Geoscientific
Model Development
Discussions

A General Lake Model (GLM 3.0) for linking with high-frequency sensor data from the Global Lake Ecological Observatory Network (GLEON)

5

Matthew R Hipsey[1,*], Louise C Bruce[1], Casper Boon[1], Brendan Busch[1], Cayelan C. Carey[2], David P Hamilton[3], Paul C. Hanson[4], Jordan S. Read[5], Eduardo de Sousa[1], Michael Weber[6], Luke A. Winslow[7]

[1] UWA School of Agriculture & Environment, The University of Western Australia, Crawley WA, 6009, Australia
10 [2] Department of Biological Sciences, Virginia Tech, Blacksburg VA, USA
[3] Australian Rivers Institute, Griffith University, Nathan QLD, 4111, Australia
[4] Center for Limnology, University of Wisconsin - Madison, Madison WI, USA
[5] Center for Integrated Data Analytics, U.S. Geological Survey, Middleton WI, USA
[6] Department of Lake Research, Helmholtz Centre for Environmental Research - UFZ, Magdeburg, Germany
15 [7] Department of Biological Sciences, Rensselaer Polytechnic Institute, Troy NY, USA

[*]*Correspondence to*: Matthew R. Hipsey (matt.hipsey@uwa.edu.au)

20

Abstract. The General Lake Model (GLM) is a one-dimensional open-source code designed to simulate the hydrodynamics of lakes, reservoirs and wetlands. GLM was developed to support the science needs of the Global Lake Ecological Observatory Network (GLEON), a network of researchers attempting to use lake sensors to understand lake functioning and address 25 questions about how lakes around the world respond to climate and land-use change. The scale and diversity of lake types, locations and sizes, as well as the expanding observational datasets, created the need for a robust community model of lake dynamics with sufficient flexibility to accommodate a range of scientific and management questions relevant to the GLEON community. This paper summarises the scientific basis and numerical implementation of the model algorithms, including details of sub-models that simulate surface heat exchange and ice-cover dynamics, vertical mixing and inflow/outflow 30 dynamics. We demonstrate the suitability of the model for different lake types, that vary substantially in their morphology, hydrology and climatic conditions. GLM supports a dynamic coupling with biogeochemical and ecological modelling libraries for integrated simulations of water quality and ecosystem health, and options for integration with other environmental models are outlined. Finally, we discuss utilities for the analysis of model outputs and uncertainty assessments, model operation within a distributed cloud-computing environment, and as a tool to support learning of network participants.

Geoscientific
Model Development
Discussions

Revision 8 Mar 2018

1 Introduction

Lakes and other standing waters support extensive ecosystem services such as water supply, flood mitigation, hydropower, aesthetic and cultural benefits, as well as fisheries and biodiversity (Mueller et al., 2016). Lakes are often considered to be "*sentinels of change*", providing a window into the sustainability of activities in their associated river basins (Williamson et al., 2009). They are also particularly susceptible to impacts from invasive species and land use development, which often lead to water quality deterioration and loss of ecosystem integrity. Recent estimates have demonstrated their significance in the earth system, contributing to heterogeneity in land surface properties and feedbacks to regional and global climate through energy, water and biogeochemical transfers (Martynov et al., 2012, Cole et al., 2007). For example, Tranvik et al. (2009) suggest carbon burial in lakes and reservoirs is substantial on a global scale, on the order of 0.6 Pg yr^{-1}, or four times the oceanic burial rate.

Given the diversity of lakes among continents, region-specific pressures and local management approaches, the Global Lake Ecological Observatory Network (GLEON: gleon.org) was initiated in 2004 as a grass-roots science community with a vision to observe, understand and predict freshwater systems at a global scale (Hanson et al., 2016). In doing so, GLEON has been a successful example of collaborative research within the hydrological and ecological science disciplines. GLEON aims to bring together environmental sensor networks, numerical models, and information technology to explore ecosystem dynamics across a vast range of scales - from individual lakes or reservoirs (Hamilton et al., 2015) to regional (Read et al., 2014; Klug et al., 2012), and even global extents (Rigosi et al., 2015; O´Reilly et al., 2015). Ultimately, it is the aim of the network to facilitate discovery and synthesis, and to provide an improved scientific basis for sustainable freshwater resource management.

Environmental modelling forms a critical component of observing systems, as a way to make sense of the "data deluge" (Porter et al., 2012), allowing users to build virtual domains to support knowledge discovery at the system scale (Ticehurst et al., 2007; Hipsey et al., 2015). In lake ecosystems, the tight coupling between physical processes and water quality and ecological dynamics has long been recognised. Models have capitalized on comprehensive understanding of physical processes (e.g., Imberger and Patterson, 1990; Imboden and Wüest, 1995) to use hydrodynamic models as an underpinning basis for coupling to ecological models. Such models have contributed to our understanding of lake dynamics, including aspects such as climate change (Winslow et al., 2017), eutrophication dynamics (Matzinger et al., 2007), harmful algal bloom dynamics (Chung et al., 2014), and fisheries (Makler-Pick et al., 2009).

In recent decades a range of 1, 2, and 3-dimensional hydrodynamic models has emerged for lake simulation. Depending on the dimensionality, the horizontal resolution of these models may vary from metres to tens of kilometres with vertical resolutions from sub-metre to several metres. As in all modelling disciplines, identifying the most parsimonious model structure and degree of complexity and resolution is challenging, and users in the lake modelling community often tend to rely on heuristic rules or practical reasons for model choice (Mooij et al., 2010). High-resolution models are suited to studying events that occur at the time scale of flow dynamics, but are not always desirable for ecological studies over longer time scales due to their computational demands and level of over-parameterisation. On the other hand, simple models may be more agile

Geoscientific
Model Development
Discussions

Revision 8 Mar 2018

for a particular application, and more suited to parameter identification and scenario testing workflows. However, it has been the case within GLEON that simple models are often less applicable across a wide variety of domains, making them less generalizable, which is a key requirement of synthesis studies. Despite the fact that there is a relatively large diversity of models and approaches for aquatic ecosystem simulation (Janssen et al., 2015), it is generally agreed that to improve scientific

5   collaboration within the limnological modelling community, there is an increasing need for flexible, open-source community models (Trolle et al., 2012). Whilst acknowledging that there is no single model suitable for all applications, a range of open-source community models and tools can enhance scientific capabilities, and foster scientific collaboration and combined efforts (Read et al., 2016). There are several examples of such initiatives being successful in the oceanography, hydrology and climate modelling communities.

10

With this in mind, the General Lake Model (GLM), a one-dimensional (1D) hydrodynamic model for enclosed aquatic ecosystems, was developed. The lake modelling community has often relied on 1D models, which originated to capture lake water balance and thermal stratification dynamics (e.g., Imberger and Patterson, 1981; Saloranta and Andersen, 2007; Perroud et al., 2009; Kirillin et al., 2011; Stepanenko et al., 2013). The use of 1D structure is justified across a diverse range of lake

15   sizes given the dominant role of seasonal changes in vertical stratification on lake dynamics, including oxygen, nutrient and metal cycling and plankton dynamics (Hamilton and Schladow, 1997; Gal et al., 2009). Despite advances in computing power and more readily available 3D hydrodynamic drivers, 1D models continue to remain attractive as they are easily linked with biogeochemical and ecological modelling libraries for complex ecosystem simulations. This allows 1D models to be used to capture the long-term trajectory and resilience of lakes and reservoirs to climate change, hydrologic change and land use

20   change. For example, such models have been used to model long-term changes to oxygen, nutrient cycles, and the changing risk of algal blooms (e.g., Peeters et al., 2007; Hu et al., 2016; Snortheim et al., 2017). Furthermore, the low computational requirements of this approach relative to 3D models is more suited to parameter identification and uncertainty analysis, making it an attractive balance between process complexity and computational intensity.

25   GLM emerged as a new open-source code in 2012, with the design goal of balancing the complexity of dimensional representation, applicability to a wide range of standing waters, and availability to a broad community (e.g., GLEON). The scope and capability of the model has developed rapidly with application to numerous lakes and lake-types within the GLEON network and beyond (e.g., Read et al., 2014; Bueche et al., 2017, Snortheim et al., 2017; Weber et al., 2017; Mencló et al., 2017; Bruce et al., 2017). It is unique in that its suitability now ranges from ephemeral wetlands and ponds to deep lakes,

30   from natural systems to heavily managed man-made reservoirs, and across climatic regions. Given that individual applications of the model rarely engage the full array of features or describe the full details of the model structure, the aim of this paper is to present a complete description of GLM, including the scientific background (Section 2), and model code organization (Section 3). The approach to coupling with biogeochemical models is also discussed (Section 4) since a main objective of the model development is to intimately link with biogeochemical models to support exploration of stratification and vertical

35   mixing on the dynamics of biogeochemical cycles and lake ecology. Finally, an overview of the use of the model within the context of GLEON specific requirements for model analysis, integration and education (Section 5-6) is described. In order to

Revision 8 Mar 2018

better define the typical level of model performance across these diverse lake types, a companion paper by Bruce et al. (2018) has undertaken a systematic assessment of the model's error structure against 31 lakes from across GLEON.

2 Model Overview

2.1 Background and layer structure

5   The 1D approach adopted by GLM resolves a vertical series of layers that capture the variation in water column properties. Users may configure any number of inflows and outflows, and more advanced options exist for simulating aspects of the water and heat balance (Figure 1). Depending on the context of the simulation, either daily or hourly meteorological time series data for surface forcing is required, and daily time series of volumetric inflow and outflow rates can also be supplied. The model is suitable for operation in a wide range of climate conditions and is able to simulate ice formation, as well as accommodating
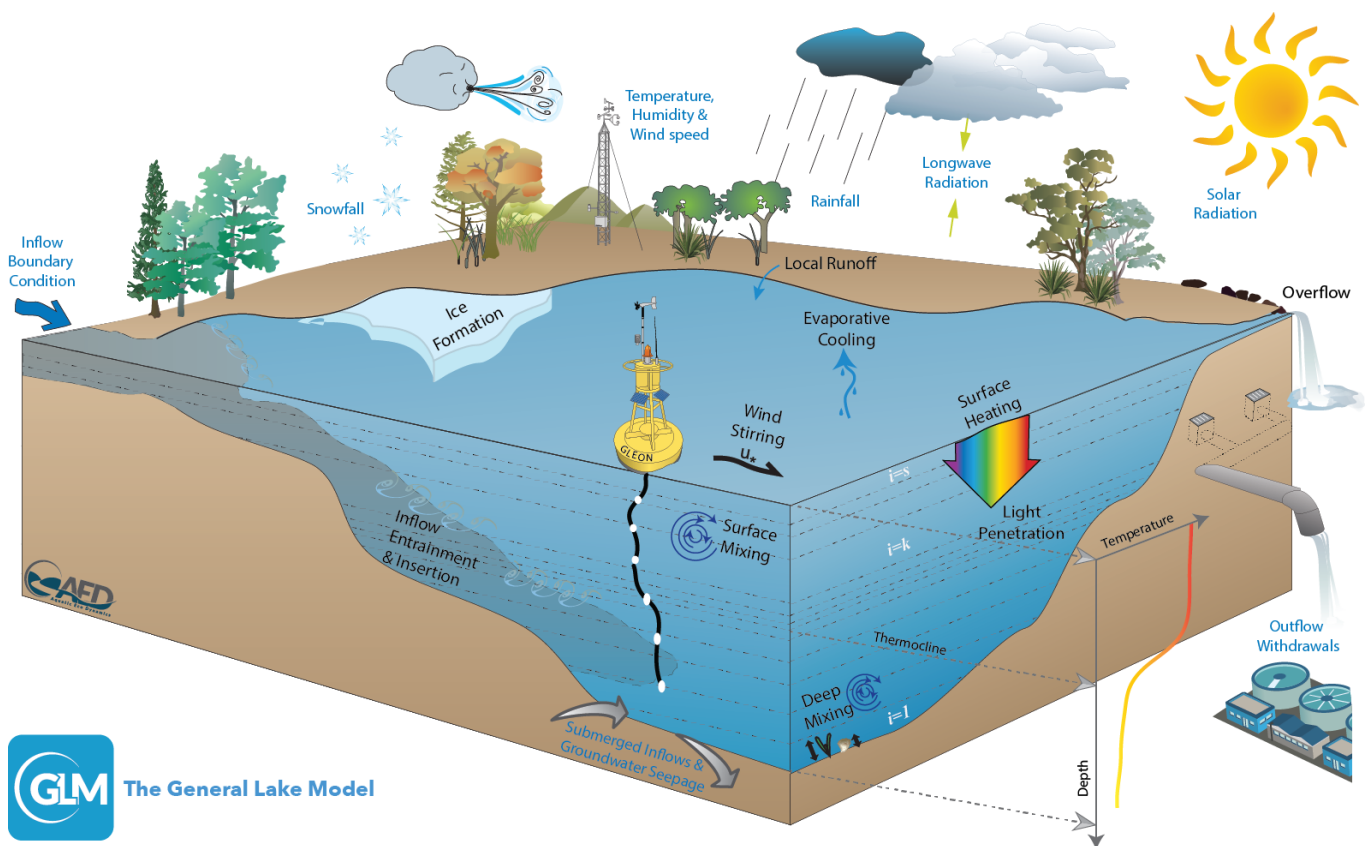
10 a range of atmospheric forcing conditions.

Figure 1: Schematic of a GLM simulation domain, input information (blue text) and key simulated processes (black text).

15 Although GLM is a new model code written in the C programming language, the core layer structure and mixing algorithms are founded on principles and experience from model platforms including the Dynamic Reservoir Simulation Model (DYRESM; Imberger and Patterson, 1981; Hamilton and Schladow, 1997) and the Dynamic Lake Model (DLM; Chung et al., 2008). Other variations have been introduced to extend this underlying approach through applications to a variety of lake and

reservoir environments (e.g., Hocking & Patterson, 1991; McCord & Schladow, 1998; Gal et al., 2003; Yeates and Imberger, 2003). The layer structure is numbered from the lake bottom to the surface, and adopts the flexible Lagrangian layer scheme first introduced by Imberger et al. (1978) and Imberger and Patterson (1981). The approach defines each layer, i, as a 'control volume' that can change thickness by contracting and expanding in response to inflows, outflows, mixing with adjacent layers,

5   and surface mass fluxes, as depicted schematically in Figure 1. As the model simulation progresses, density changes due to surface heating, vertical mixing, and inflows and outflows lead to dynamic changes in the layer structure, associated with layers amalgamating, expanding, contracting or splitting. Notation used throughout the model description is provided in Table 1.

10   As layers change, their volumes change based on the site-specific hypsographic curve, whereby the overall lake volume, V_{max}, is defined as $\int_{H_0}^{H_{max}} A[H] \, dH$, with the elevation ($H$), and area ($A$) relationship provided as a series of points based on bathymetric data. This computation requires the user to provide a number, N_{BSN}, of heights with corresponding areas. The cumulative volume at any lake elevation is first estimated as:

$$V_b = V_{b-1} + [A_{b-1} + 0.5(A_b - A_{b-1})](H_b - H_{b-1}) \tag{1}$$

where $2 \leq b \leq N_{BSN}$. Using this raw hyposgraphic data, a refined height-area-volume relationship is then internally computed

15   using finer height increments (e.g., $\Delta H_{mi} \sim 0.1$ m), giving N_{MORPH} levels that are used for subsequent calculations. The area and volume at the height of each increment, H_{mi}, are interpolated from the supplied information as:

$$V_{mi} = V_{b-1} \left(\frac{H_{mi}}{H_{b-1}} \right)^{\alpha_{b-1}} \quad \text{and} \quad A_{mi} = A_{b-1} \left(\frac{H_{mi}}{H_{b-1}} \right)^{\beta_{b-1}} \tag{2}$$

where V_{mi} and A_{mi} are the volume and area at each of the elevations of the interpolated depth vector, and V_{b-1} and A_{b-1} refer to the nearest b level below H_{mi} such that $H_{b-1} < H_{mi}$. The interpolation coefficients are computed as:

$$\alpha_b = \left[\frac{log_{10}\left(\frac{V_{b+1}}{V_b} \right)}{log_{10}\left(\frac{H_{b+1}}{H_b} \right)} \right] \quad \text{and} \quad \beta_b = \left[\frac{log_{10}\left(\frac{A_{b+1}}{A_b} \right)}{log_{10}\left(\frac{H_{b+1}}{H_b} \right)} \right]. \tag{3}$$

Within this lake domain, the model solves the water balance by including several user configurable water fluxes that change

20   the layer structure. Initially, the layers are assumed to be of equal thickness, and the initial number of layers, $N_{LEV}(t = 0)$ is computed based on the initial water depth. Water fluxes include surface mass fluxes (evaporation, rainfall and snowfall), inflows (surface inflows, submerged inflows and local runoff from the surrounding exposed lake bed area) and outflows (withdrawals, overflow and seepage). Surface mass fluxes operate on a sub-daily time step, Δt, by impacting the surface layer thickness (described in Section 2.2), whereby the dynamics of inflows and outflows modify the overall lake water balance and

25   layer structure on a daily time step, Δt_d, by adding, merging or removing layers (described in Section 2.7). Depending on whether a surface (areal) mass flux or volumetric mass flux is being applied, the layer volumes are updated by interpolating changes in layer heights, whereby $V_i = f[h_i]$, and i is the layer number, or layer heights are updated by interpolating changes in layer volumes, whereby $h_i = f[V_i]$.

30   Each layer also contains heat, salt (S) and other constituents (C) which are generically referred to as scalars. These are subject to mass conservation as layers change thickness or are merged or split. The specific number of other constituents depends on

Geoscientific
Model Development
Discussions

Revision 8 Mar 2018

the configuration of the associated water quality model, but typically includes attributes such as oxygen, nutrients and phytoplankton. Layer density is computed from the local salinity and temperature according to TEOS-10, whereby $\rho_i = \rho[T_i, S_i]$. When sufficient energy becomes available to overcome density instabilities between adjacent layers, the layers merge, thereby accounting for the process of mixing (Section 2.6). For deeper systems, a stable vertical density gradient will

5   form in response to periods of high solar radiation creating warm, buoyant water overlying cooler, denser water, separated by a metalimnion region which includes the thermocline. Layer thickness limits, Δz_{min} and Δz_{max}, are enforced to adequately resolve the vertical density gradient, generally with fine resolution occurring in the metalimnion and thicker cells where mixing is active. The number of layers, $N_{LEV}(t)$, is adjusted throughout the simulation to maintain homogenous properties within a layer. It has been reported that numerical diffusion at the thermocline can be restricted using this layer structure and mixing

10   algorithm (depending on the minimum and maximum layer thickness limits set by the user), making it particularly suited to long-term investigations, and ideally requiring limited site-specific calibration (Patterson et al., 1984; Hamilton and Schladow, 1997; Bruce et al., 2018).

Because this approach assumes layer properties are laterally averaged, the model is suitable for investigations where resolving

15   the horizontal variability is not a requirement of the study. This is often the case for ecologists and biogeochemists studying central basins of natural lakes (e.g., Gal et al., 2009), managers simulating drinking water reservoirs (e.g., Weber et al., 2017), or mining pit lakes (e.g., Salmon et al., 2017), or for analyses exploring the coupling between lakes and regional climate (e.g., Stepanenko et al., 2013). Further, whilst the model is able to resolve vertical stratification, the approach is also able to be used to simulate shallow lakes, wetlands, wastewater ponds and other small waterbodies that experience well-mixed conditions. In

20   this case, the layer resolution, with upper and lower layer bounds specified by the user, will automatically be reduced, and the mass of water and constituents, and energy will continue to be conserved. The remainder of this section outlines the model components and provides example outputs for five water bodies that experience a diverse hydrology (Figure 2).

2.2 Surface water balance

The mass balance of the surface layer is computed at each model time step (Δt; usually hourly), by modifying the surface layer

25   height according to:

$$\frac{dh_S}{dt} = R_F + S_F + \frac{Q_R}{A_s} - E - \frac{d\Delta z_{ice}}{dt} \qquad (4)$$

where h_S is the top height of the surface layer (m), t is the time (s), E is the evaporation mass flux computed from the heat flux ϕ_E, described below ($E = -\phi_E/\lambda_v\rho_s$; m s^{-1}), R_F is rainfall and S_F is snowfall (m s^{-1}). R_F and S_F both affect the water surface height depending on the presence of ice cover:

$$R_F = \begin{cases} f_R R_x/c_{secday} \, , & \text{if } \Delta z_{ice} = 0 \\ f_R R_x/c_{secday} \, , & \text{if } \Delta z_{ice} > 0 \text{ and } T_a > 0 \\ 0 \, , & \text{if } \Delta z_{ice} > 0 \text{ and } T_a \leq 0 \end{cases} \qquad (5)$$

and

$$S_F = \begin{cases} f_S f_{SWE} S_x/c_{secday} \, , & \text{if } \Delta z_{ice} = 0 \\ 0, & \text{if } \Delta z_{ice} > 0 \end{cases} \qquad (6)$$

Geoscientific
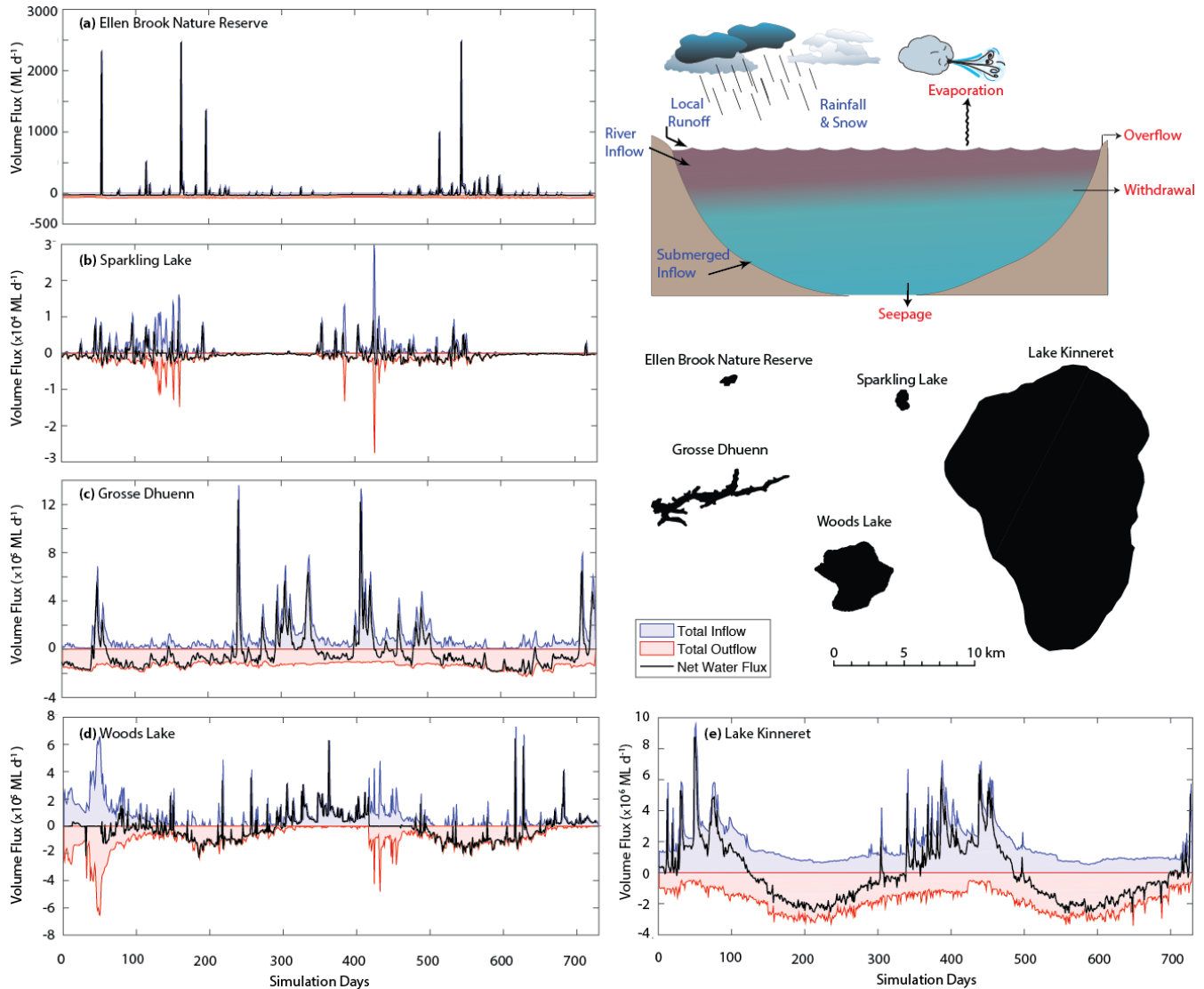Model Development
Discussions

Revision 8 Mar 2018

Figure 2: A two-year times-series of the simulated daily water balance for five example lakes, a-e, that range in size and hydrology. The water balance components summarised are depicted schematically in the inset, and partitioned into inputs and outputs. The net water flux in a time step is: $dV/dt = \Delta h_s A_s + \sum_I^{N_{INF}} Q_{inf_{0_I}} - \sum_O^{N_{OUT}} Q_{outf_O} - Q_{ovfl} - Q_{seepage}$**. For more information about each lake, the simulation configuration and input data, refer to the Data availability section.**

Here f_R and f_S are user definable scaling factors that may be applied to adjust the input data values, R_x and S_x respectively. The surface height of the water column is also impacted by ice formation or melting, according to $d\Delta z_{ice}/dt$, as described in Section 2.4.

10

Q_R is an optional term to account for runoff to the lake from the exposed riparian banks, which may be important in reservoirs with a large drawdown range, or wetlands where periodic drying of the lake may occur. The runoff volume generated is averaged across the area that the active lake surface area (A_s) is not occupying, and the amount is calculated using a simple model based on exceedance of a rainfall intensity threshold, R_L (m day^{-1}), and runoff coefficient:

Geoscientific
Model Development
Discussions

Open Access

EGU

Revision 8 Mar 2018

$$Q_R = max\big[0, f_{ro}\big(R_F - R_L/c_{secday}\big)\big](A_{max} - A_s) \tag{7}$$

where f_{ro} is the runoff coefficient, defined as the fraction of rainfall that is converted to runoff at the lake's edge, and A_{max} is the maximum possible area of inundation of the lake (the area provided by the user as the N_{BSN} value).

Note that mixing dynamics (i.e., the merging or splitting of layers to enforce the layer thickness limits), will impact the
5   thickness of the surface mixed layer, z_{sml}, but not change the overall lake height. However, in addition to the terms in Eq. 4, h_S is modified due to volume changes associated with river inflows, withdrawals, seepage or overflows, which are described in subsequent sections.

2.3 Surface energy balance

A balance of shortwave and longwave radiation fluxes, and sensible and evaporative heat fluxes (all W m^{-2}) determines the
10   net cooling and heating across the surface. The general heat budget equation for the upper most layer is described as:

$$c_w \rho_s z_s \frac{dT_s}{dt} = \phi_{SW_S} - \phi_E + \phi_H + \phi_{LWin} - \phi_{LWout} \tag{8}$$

where c_w is the specific heat capacity of water, T_s is the surface temperature, and z_s and ρ_s are the depth and density of the surface layer ($i = N_{LEV}$), respectively. The RHS heat flux terms are computed at each time step, and include several options for customizing the individual surface heat flux components, which are expanded upon below.

2.3.1 Solar heating and light penetration

15   Solar radiation is the key driver of the lake thermodynamics and may be input based on daily or hourly measurements from a nearby pyranometer. If data is not available then users may choose to either have GLM compute surface irradiance from a theoretical approximation based on the Bird Clear Sky insolation model (BCSM) (Bird, 1984), modified for cloud cover and latitude. Therefore the options for input are summarised as:

$$\phi_{SW_0} = \begin{cases} (1 - \alpha_{SW})\, f_{SW}\, \phi_{SW_x}\, f[d, t - \lfloor t \rfloor], & \text{Option 1: daily insolation data provided} \\ (1 - \alpha_{SW})\, f_{SW}\, \phi_{SW_x}, & \text{Option 2: sub-daily input data provided} \\ (1 - \alpha_{SW})\, \hat{\phi}_{SW}, & \text{Option 3: data is computed from the BCSM} \end{cases} \tag{9a-c}$$

where ϕ_{SW_0} is the solar radiation flux entering the surface layer, ϕ_{SW_x} is the incoming shortwave radiation flux supplied by
20   the user, f_{SW} is a scaling factor that may be applied and adjusted as part of the calibration process, and α_{SW} is the albedo for shortwave radiation. If daily data is supplied (Option 1), the model continues to run at a sub-daily time step, but applies the algorithm outlined in Hamilton and Schladow (1997) to distribute the daily solar energy flux over a diurnal cycle, based on the day of the year, d, and time of day, $t - \lfloor t \rfloor$. For Option 3 the BCSM is used (Bird, 1984; Luo et al., 2010):

$$\hat{\phi}_{SW} = \frac{\hat{\phi}_{DB} + \hat{\phi}_{AS}}{1 - (\alpha_{SW}\, \alpha_{SKY})}\, f[C] \tag{10}$$

Geoscientific
Model Development
Discussions

Revision 8 Mar 2018

where the total irradiance, $\hat{\phi}_{SW}$, is computed from direct beam $\hat{\phi}_{DB}$, and atmospheric scattering $\hat{\phi}_{AS}$ components (refer to Appendix A for a detailed outline of the BCSM equations and parameters). In GLM, the clear sky value is then reduced according to the cloud cover data provided by the user, C_x, according to:

$$f[C_x] = 0.66182\, C_x{}^2 - 1.5236\, C_x + 0.98475 \tag{11}$$

which is based on a polynomial regression of cloud data from Perth Airport, Australia, compared against nearby sensor data
5 ($R^2 = 0.952$; see also Luo et al., 2010).

The albedo, α_{SW}, is the reflected fraction of the incoming radiation and depends on surface conditions including the presence of ice, waves and the angle of incident radiation. For open water conditions, users may configure:

Option 1 : Daily approximation, Hamilton and Schladow (1997)

$$\alpha_{SW} = \begin{cases} 0.08 - 0.02\, sin\left[\frac{2\pi}{365} d - \frac{\pi}{2}\right] & \text{:northern hemisphere} \\ 0.08 & \text{:equator} \\ 0.08 - 0.02\, sin\left[\frac{2\pi}{365} d + \frac{\pi}{2}\right] & \text{:southern hemisphere} \end{cases} \tag{12a}$$

Option 2 : Briegleb et al. (1986)

$$\alpha_{SW} = \frac{1}{100}\left(\frac{2.6}{cos[\Phi_{zen}]^{1.7}+0.065} + 15(cos[\Phi_{zen}] - 0.1)(cos[\Phi_{zen}] - 0.5)[cos[\Phi_{zen}] - 1]\right) \tag{12b}$$

Option 3 : Yajima and Yamamoto (2015)

$$\alpha_{SW} = max\left[0.02, 0.001\,\frac{RH_x}{100}\,[1 - cos(\Phi_{zen})]^{0.33} - 0.001\, U_{10}\,[1 - cos(\Phi_{zen})]^{-0.57} - 0.001\,\varsigma\,[1 - cos(\Phi_{zen})]^{0.829}\right] \tag{12c}$$

where Φ_{zen} is the solar zenith angle (radians) as outlined in Appendix A, RH_x is the relative humidity, ς is the atmospheric
10 diffuse radiation, d is the day of year, and U_x is wind speed. The second (oceanic) and third (lacustrine) options are included to allow for diel and seasonal variation of albedo from approximately 0.01 to 0.4 depending on the sun-angle (Figure 3). Albedo is calculated separately during ice cover conditions using a customised algorithm, outlined below in Section 2.4.
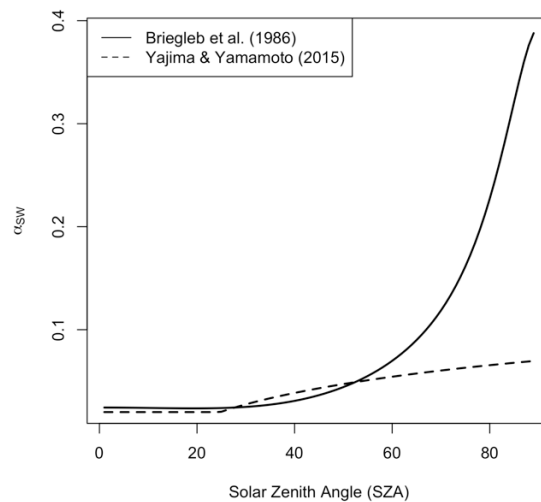
Figure 3: Variation of albedo (α_{SW}) with solar zenith angle (SZA = $\Phi_{zen}180/\pi$, degrees) for `albedo_mode` 2 and 3 (Eq. 12). For
15 option 3, settings of RH = 80 % and U = 6 m s^{-1} were assumed.

Geoscientific
Model Development
Discussions

The depth of penetration of shortwave radiation into the lake is wavelength specific, and depends on the water clarity via the light extinction coefficient, K_w (m^{-1}). Two approaches are supported in GLM. The first option assumes the Photosynthetically Active Radiation (PAR) fraction of the incoming light is the most penetrative, and follows the Beer-Lambert Law:

$$\phi_{PAR}[z] = f_{PAR}\,\phi_{SW_0}\,exp[-K_w z] \tag{13}$$

where z is the depth of any layer from the surface. K_w may be set by the user as constant or linked to the water quality model

5   (e.g., FABM or AED2, see Section 4) in which case the extinction coefficient will change as a function of depth and time according to the concentration of dissolved and particulate constituents. For this option Beer's Law is only applied for the photosynthetically active fraction, f_{PAR}, which is set as 45% of the incident light. The amount of radiation heating the surface layer, ϕ_{SW_S}, is therefore the photosynthetically active fraction that is attenuated across z_{sml}, plus the entire $(1 - f_{PAR})$ fraction, which accounts for near infra-red and ultraviolet bandwidths of the incident shortwave radiation $\phi_{SW_S} = \phi_{SW_0} - \phi_{PAR}[z_{sml}]$.

10   and implicitly assumes these have significantly higher attenuation coefficients (Kirk, 1994). The second option adopts a more complete light adsorption algorithm that integrates the attenuated light intensity across the bandwidth spectrum:

$$c_w\rho_s\Delta z_i\frac{dT_i}{dt} = \sum_{k=1}^{N_{SW}}\phi_{SW_{i_k}}[z_i] - \sum_{k=1}^{N_{SW}}\phi_{SW_{i-1_k}}[z_{i-1}] \tag{14}$$

where k is the bandwidth index $\phi_{SW_{i_k}}[z_i]$ is the radiation flux at the top of the i th layer. For this option, the model by Cengel and Ozisk (1984) is adopted to compute $\phi_{SW_{i_k}}(z_i)$, which more comprehensively resolves the light climate including incident and diffuse radiation components, the angle of incident light and transmission across the light surface (based on the Fresnel

15   equations), and reflection off the bottom. These processes are wavelength specific and the user must specify the number of simulated bandwidths, N_{SW}, and their respective absorption coefficient.

The light reaching the benthos may be used in some applications as an indicator of benthic productivity, and a proxy for the type of benthic habitat that might emerge. In addition to the light profiles, GLM also predicts the benthic area of the lake where

20   light intensity exceeds a user defined fraction of the surface irradiance, $f_{BEN_{crit}}$, (Figure 4):

$$A_{BEN} = A_s - A[h_{BEN}] \tag{15}$$

where $h_{BEN} = h_s - z_{BEN}$, and z_{BEN} is calculated from Beer's law:

$$z_{BEN} = -\frac{ln[f_{BEN_{crit}}]}{K_w} \tag{16}$$

and the daily average benthic area above the threshold is then reported as a percentage (A_{BEN}/A_s).

2.3.2 Longwave radiation

25   Longwave radiation can be provided as a net flux, an incoming flux or, if there is no radiation data from which longwave radiation can be computed, then it may be calculated by the model internally based on the cloud cover fraction and air temperature. Net longwave radiation is described as:

Geoscientific
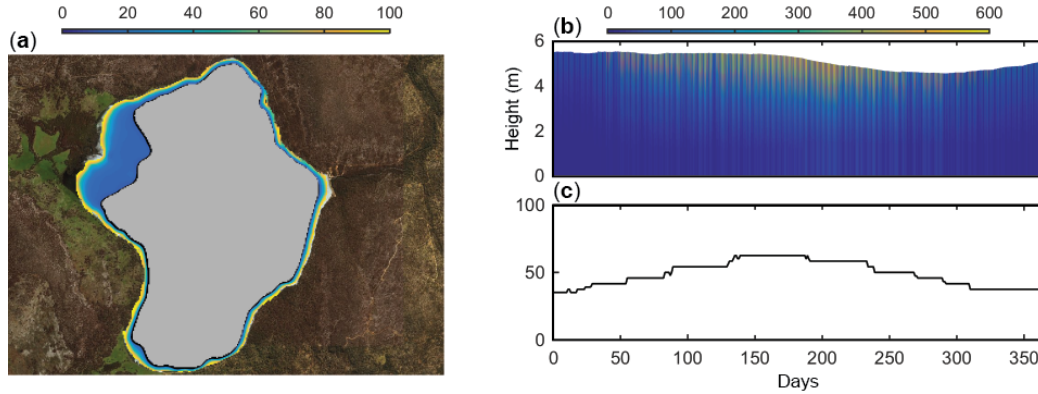Model Development
Discussions

Revision 8 Mar 2018

Figure 4: Example light data outputs from a GLM application to Woods Lake, Australia, showing a) the ratio of benthic to surface light, $\phi_{PAR_{BEN}}/\phi_{SW_0}$ (%), overlain on the lake map based on the bathymetry, b) a time series of the depth variation in light (W m^{-2}), and c) a time series of A_{BEN}/A_s (as %) for $f_{BEN_{crit}} = 0.2$.

5

$$\phi_{LW_{net}} = \phi_{LW_{in}} - \phi_{LW_{out}} \tag{17}$$

where

$$\phi_{LW_{out}} = \varepsilon_w \sigma (\theta_s)^4 \tag{18}$$

and σ is the Stefan-Boltzman constant and ε_w the emissivity of the water surface, assumed to be 0.985. If the net or incoming longwave flux is not provided, the model will compute the incoming flux from:

$$\phi_{LW_{in}} = (1 - \alpha_{LW}) \varepsilon_a^* \sigma (\theta_a)^4 \tag{19}$$

10   where α_{LW} is the longwave albedo (0.03). The emissivity of the atmosphere can be computed considering emissivity of cloud-free conditions (ε_a), based on air temperature (T_a) and vapour pressure, and extended to account for reflection from clouds, such that $\varepsilon_a^* = f[T_a, C_x, e_a]$ (see Henderson-Sellers, 1986; Flerchinger, 2009). Options available in GLM include:

$$\varepsilon_a^* = \begin{cases} (1 + 0.275\,C_x)(1 - 0.261\exp[-0.000777\,T_a{}^2]), & \text{Option 1: Idso and Jackson (1969)} \\ (1 + 0.17\,C_x^2)\,(9.365{\times}10^{-6}(\theta_a)^2), & \text{Option 2: Swinbank (1963)} \\ (1 + 0.275\,C_x)\,0.642\,(e_a/\theta_a)^{1/7}, & \text{Option 3: Brutsaert (1975)} \\ (1 - C_x^{2.796})\,1.24\,(e_a/\theta_a)^{1/7} + 0.955\,C_x^{2.796}, & \text{Option 4: Yajima and Yamamoto (2015)} \end{cases} \tag{20a-d}$$

15   where, C_x is the cloud cover fraction (0-1), e_a the air vapour pressure calculated from relative humidity, and options 1-4 are chosen via the `cloud_mode` variable. Note that cloud cover is typically reported in octals (0-8) with each value depicting a fraction of 8, thus a value of 1 would correspond to a fraction of 0.125. Some data may also include cloud type and their respective heights. If this is the case, good results have been reported by averaging the octal values for all cloud types to get an average cloud cover.

20

If longwave radiation data does not exist and cloud data is also not available, but solar irradiance is measured, then GLM `rad_mode` setting 3 will instruct the model to compare the measured and theoretical clear-sky solar irradiance (estimated by

11

Geoscientific
Model Development
Discussions

the BCSM; Eq. 10) to approximate the cloud cover fraction by assuming that $\phi_{SW_x}/\hat{\phi}_{SW} = f[C_x]$. Note that if neither shortwave or longwave radiation is provided, then the model will use the BCSM to compute incoming solar irradiance, and cloud cover will be assumed to be 0 (noting that this is likely to be an overestimate of downwelling shortwave radiation).

2.3.3 Sensible and latent heat transfer

5 The model accounts for the surface fluxes of sensible heat and latent heat using commonly adopted bulk aerodynamic formulae. For sensible heat:

$$\phi_H = -\rho_a c_a C_H U_{10}(T_s - T_a) \tag{21}$$

where c_a is the specific heat capacity of air, C_H is the bulk aerodynamic coefficient for sensible heat transfer, T_a the air temperature and T_s the temperature of the water surface layer. The air density (kg m^{-3}) is computed from $\rho_a = 0.348\,(1 + r)/(1 + 1.61r)\, p/T_a$, where p is air pressure (hPa) and r is the mixing ratio, which is used to compute

10 the gas constant.

For latent heat:

$$\phi_E = -\rho_a C_E \lambda_v U_{10} \frac{\omega}{p} (e_s[T_s] - e_a[T_a]) \tag{22}$$

where C_E is the bulk aerodynamic coefficient for latent heat transfer, e_a the air vapour pressure, e_s the saturation vapour pressure (hPa) at the surface layer temperature (°C), ω the ratio of molecular mass of water to molecular mass of dry air

15 (= 0.622) and λ_v the latent heat of vaporisation. The vapour pressure can be calculated by the following formulae:

$$e_s[T_s] = \begin{cases} exp\left[2.3026\left(7.5\frac{T_s}{T_s + 237.3}\right) + 0.7858\right], & \text{Option 1 : TVA (1972) - Magnus-Tetens} & (23a) \\[2mm] exp\left[6.1094\left(\frac{17.625\,T_s}{T_s + 243.04}\right)\right], & \text{Option 2 : August-Roche-Magnus} & (23b) \\[2mm] 10^{\left(9.28603523\,\frac{2322.37885\,T_s}{T_s+273.15}\right)}, & \text{Option 3 : Tabata (1973) - Linear} & (23c) \end{cases}$$

and

$$e_a[T_a] = f_{RH} RH_x\, e_s[T_a] \tag{24}$$

The net heat fluxes for the example lakes are shown in Figure 5.

Correction for non-neutral atmospheric stability: For long-time (e.g., seasonal) integrations, the bulk-transfer coefficients for

20 momentum, C_D, sensible heat, C_H, and latent heat, C_E, can be assumed approximately constant because of the negative feedback between surface forcing and the temperature response of the water body (e.g., Strub and Powell, 1987). At finer timescales (hours to weeks), the thermal inertia of the water body is too great and so the transfer coefficients must be specified as a function of the degree of atmospheric stratification experienced in the internal boundary layer that develops over the water (Woolway et al. 2017). Monin and Obukhov (1954) parameterised the stratification in the air column using the now well-

Geoscientific
Model Development
Discussions

known stability parameter, z/L, which is used to define corrections to the bulk aerodynamic coefficients C_H and C_E, using the numerical scheme presented in Appendix B. The corrections may be optionally applied within a simulation, and if enabled, the transfer coefficients used above are automatically updated. This option requires the measurement of wind speed, air temperature and relative humidity within the internal boundary layer over the lake surface, supplied at an hourly resolution.

5
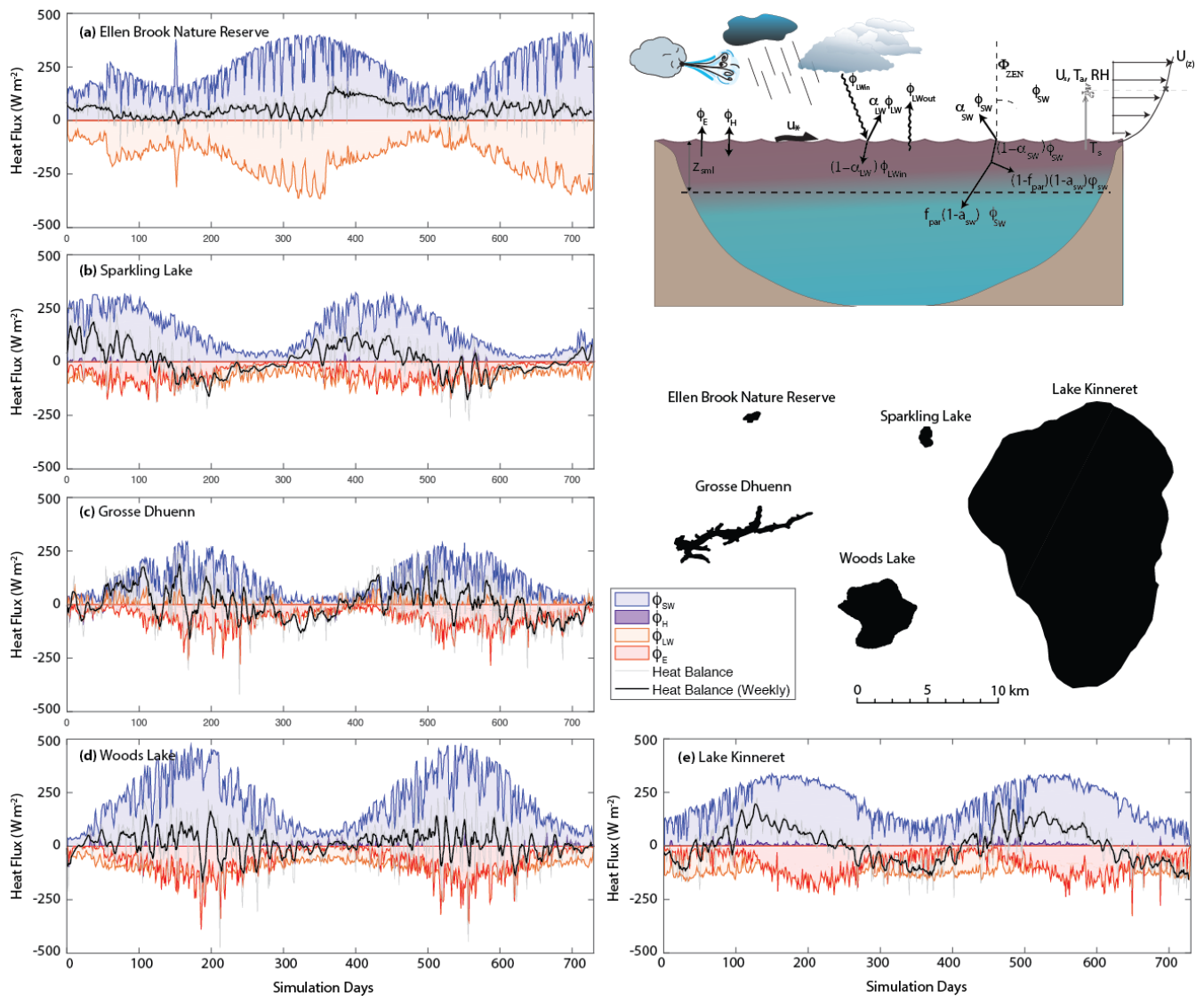
Figure 5: A two-year times-series of the simulated daily heat fluxes for the five example lakes, a-e, that were depicted in Figure 2. The heat balance components summarised are depicted schematically in the inset, as described in Section 2.3 and the "Heat Balance" line refers to the LHS of Eq. 8.

10

Wind sheltering: Wind sheltering may be important depending on the lake size and shoreline complexity, and is parameterised according to several methods based on the context of the simulation and data available. For example, Hipsey et al. (2003) presented a simple adjustment to the bulk transfer equation to account for the effect of wind sheltering in small reservoirs

Revision 8 Mar 2018

using a shelter index to account for the length scale associated with the vertical obstacle relative to the horizontal length scale associated with the water body itself. Markfort et al. (2009) estimate the effect of a similar sheltering length-scale on the overall lake area. Therefore, within GLM, users may specify the degree of sheltering or fetch limitation using either constant or direction-specific options for computing an "effective" area:

$$A_E = \begin{cases} A_S, & \text{Option 0: no sheltering (default)} \\ A_S \tanh\left(\dfrac{A_S}{A_{WS}}\right), & \text{Option 1: Yeates \& Imberger (2003)} \\ \dfrac{L_D{}^2}{2} cos^{-1}\left(\dfrac{x_{WS}{}^\Phi}{L_D}\right) - \dfrac{x_{WS}{}^\Phi}{L_D}\sqrt{L_D{}^2 - (x_{WS}{}^\Phi)^2}, & \text{Option 2: Markfort et al. (2009)} \\ f_{WS}[\Phi_{wind}] \, A_S, & \text{Option 3: user} - \text{defined} \end{cases} \quad (25\text{a-d})$$

5

where A_{WS} is a user defined critical lake area for wind sheltering to dominate, x_{WS} is a user defined sheltering distance, and L_D the lake diameter ($L_D = 0.5(L_{crest} + W_{crest})$). For option 1, the sheltering factor is held constant for the simulation based on the size of the lake, whereas the latter two options require users to additionally input wind direction data, and a direction function, $f_{WS}[\Phi_{wind}]$, to allow for a variable sheltering effect over time. In the case of option 2, this function scales the

10   sheltering distance, x_{WS}, as a function of wind direction, $x_{WS}{}^\Phi = x_{WS}(1 - min(f_{WS}[\Phi_{wind}], 1))$, whereas in the case of option 3 the function reads in an effective area scaling fraction directly.

The ratio of the effective area to the total area of the lake, A_E/A_S, is then used to scale the wind speed data input by the user, U_x, as a means of capturing the average wind speed over the entire lake surface, such that $U_{10} = f_U U_x A_E/A_S$, where f_U is a

15   wind speed adjustment factor that can be used to assist calibration, or to correct the raw wind speed data to the reference height of 10 m.

Still-air limit: The above formulations only apply when sufficient wind exists to create a defined boundary layer over the surface of the water. As the wind tends to zero (the 'still-air limit'), Eqs. 21-22 become less appropriate as they do not account

20   for free convection directly from the water surface. This is a relatively important phenomenon for small lakes, cooling ponds and wetlands since they tend to have small fetches that limit the energy input from wind. These water bodies may also have large areas sheltered from the wind and will develop surface temperatures warmer than the atmosphere for considerable periods. Therefore, users can optionally augment Eqs. 21-22 with calculations for low wind speed conditions by calculating the evaporative and sensible heat flux values for both the given U_{10} and for an assumed $U_{10} = 0$. The chosen value for the

25   surface energy balance (as applied in Eq. 8) is found by taking the maximum value of the two calculations:

$$\phi_X^* = \begin{cases} \max\left[\phi_X, \phi_{X_0}\right], & \text{Option 1: no} - \text{sheltering area} \\ \max\left[\phi_X, \phi_{X_0}\right] A_E/A_S + \phi_{X_0}(A_S - A_E)/A_S, & \text{Option 2: still} - \text{air sheltered area} \end{cases} \quad (26)$$

where ϕ_{X_0} is the zero-wind flux for either the evaporative or sensible heat flux (and ϕ_X is calculated from Eqs. 21-22). The two zero-wind speed heat flux equations are from TVA (1972), but modified to return energy flux in SI units (W m^{-2}):

Revision 8 Mar 2018

$$\phi_{E_0} = \rho_s \, \lambda_v \, \alpha_e (\vartheta_s - \vartheta_a) \tag{27a-b}$$

$$\phi_{H_0} = \alpha_h (T_s - T_a)$$

$$\alpha_e = 0.137 \; f_0 \; \frac{K_{air}}{c_a \rho_s} \left(g \, \frac{|\rho_a - \rho_o|}{\rho_a \, \nu_a \, D_a} \right)^{1/3} \tag{28a-b}$$

$$\alpha_h = 0.137 \, f_0 \, K_{air} \left(g \, \frac{|\rho_a - \rho_o|}{\rho_a \, \nu_a \, D_a} \right)^{1/3}$$

where $\vartheta = \kappa \, e/p$, with the appropriate vapour pressure values, e, for both surface and ambient atmospheric values. Here, K_{air} is the molecular heat conductivity of air (J m^{-1} s^{-1} C^{-1}), ν_a is the kinematic viscosity of the air (m^2 s^{-1}), ρ_o is the density of the saturated air at the water surface temperature, ρ_s is the density of the surface water, f_0 is a dimensionless roughness correction coefficient for the lake surface and D_a is the molecular heat diffusivity of air (m^2 s^{-1}). Note that the impact of low wind speeds

5 on the drag coefficient is captured by the modified Charnock relation (Eq. A24), which includes an additional term for the smooth flow transition (see also Figure A1).

2.4 Snow and ice dynamics

The algorithms for GLM ice and snow dynamics are based on previous ice modelling studies (Patterson and Hamblin, 1988; Gu and Stefan, 1993; Rogers et al., 1995; Vavrus et al., 1996; Launiainen and Cheng, 1998; Magee et al., 2016). To solve the

10 heat transfer equation, the ice model uses a quasi-steady assumption that the time scale for heat conduction through the ice is short relative to the time scale of changes in meteorological forcing (Patterson and Hamblin, 1988; Rogers et al., 1995). The steady-state conduction equations are used with a three-layer ice model that includes blue ice (or black ice), white ice (or snow ice) and snow (see Eq. 1 and Fig. 5 of Rogers et al., 1995), and forced at the surface based on shortwave radiation which is partitioned into two components, a visible (f_{VIS}) and an infra-red ($1 - f_{VIS}$) spectral band. Blue ice is formed through direct

15 freezing of lake water into ice whereas white ice is generated in response to flooding, when the mass of snow that can be supported by the buoyancy of the ice cover is exceeded (Rogers et al., 1995). By assigning appropriate boundary conditions to the interfaces and solving the quasi-steady state equation for heat transfer numerically, the model computes the upward conductive heat flux through the ice and snow cover to the atmosphere, termed ϕ_0. The estimation of ϕ_0 applies an empirical equation to estimate snow conductivity, K_{snow}, from its density (Ashton, 1986; Figure 6).

20

At the solid surface (ice or snow), a heat flux balance is employed to provide the condition for surface melting:

$$\phi_0[T_0] + \phi_{net}[T_0] = 0 \qquad\qquad T_0 < T_m \tag{29}$$

$$\phi_{net}[T_0] = -\rho_{ice,snow} \, \lambda_f \frac{d\Delta z_{ice,snow}}{dt} \qquad\qquad T_0 = T_m \tag{30}$$

where λ_f is the latent heat of fusion, $\Delta z_{ice,snow}$ is the height of the upper snow or ice layer, $\rho_{ice,snow}$ is the density of either the snow or ice, determined from the surface medium properties, T_0 is the temperature at the solid surface, T_m is the melt-water temperature (0 ^{o}C) and $\phi_{net}[T_0]$ is the net incoming heat flux for non-pentrative radiation at the solid surface:

Geoscientific
Model Development
Discussions

Revision 8 Mar 2018

$$\phi_{net}[T_0] = \phi_{LWin} - \phi_{LWout}[T_0] + \phi_H[T_0] + \phi_E[T_0] + \phi_R[T_0] \tag{31}$$

where the heat fluxes between the solid boundary and the atmosphere are calculated as outlined previously, but with modification for the determination of vapor pressure over ice or snow (Gill, 1982), and the addition of the rainfall heat flux, ϕ_R, (Rogers et al., 1995). T_0 is determined using a bilinear iteration until surface heat fluxes are balanced (i.e., $\phi_0[T_0] = -\phi_{net}[T_0]$) and T_0 is stable (± 0.001 °C). In the presence of ice (or snow) cover, a surface temperature $T_0 > T_m$ indicates that

5 energy is available for melting. The amount of energy for melting is calculated by setting $T_0 = T_m$ to determine the reduced thickness of snow or ice (as shown in Eq. 30).

Accretion or ablation of ice is determined through the heat flux at the ice-water interface, ϕ_f. Shortwave radiation is absorbed and attenuates with different extinction depths for snow, white ice, and blue ice, and these also depend on wavelength of the

10 light. Assuming two light bandwidths, we solve for the heat conduction through ice to yield:

$$\phi_f = \phi_0 \; - f_{VIS}\, \phi_{SW_0}\, (1 - \exp[-K_{s1}\Delta z_{snow} - K_{w1}\Delta z_{white} - K_{b1}\Delta z_{blue}])$$
$$- (1 - f_{VIS})\, \phi_{SW_S}\, (1 - \exp[-K_{s2}\Delta z_{snow} - K_{w2}\Delta z_{white} - K_{b2}\Delta z_{blue}])$$
$$- \phi_{white}^*\Delta z_{snow} \tag{32}$$

where ϕ_{SW_0} is the shortwave radiation penetrating the ice/snow surface, K refers to the light attenuation coefficient of the ice and snow components designated with subscripts *s, w* and *b* for snow, white ice and blue ice respectively, and Δz refers to the thickness of snow, white ice and blue ice. ϕ_{white}^* is a volumetric heat flux for the formation of snow ice, which is given in Eq.

15 14 of Rogers et al. (1995). Ice and snow light attenuation coefficients in GLM are fixed to the same values as those given by Rogers et al. (1995). Shortwave albedo for the ice or snow surface is a function of surface medium (snow or ice), surface temperature and ice or snow thickness (see Table 1 of Vavrus et al., 1996). Values of albedo derived from these functions vary from 0.08 to 0.6 for ice and from 0.08 to 0.7 for snow, depending on the surface temperature and their layer thickness.

20 The imbalance between ϕ_f moving through the blue ice layer and the heat flux from the water into the ice, ϕ_w, gives the rate of change of ice thickness at the interface with water:

$$\frac{d\Delta z_{blue}}{dt} = \frac{\phi_f - \phi_w}{\rho_{blue}\, \lambda_f} \tag{33}$$

where ρ_{blue} is the density of blue ice and ϕ_w is given by a finite difference approximation of the conductive heat flux from water to ice:

$$\phi_w = -K_{water}\, \frac{\Delta T}{\delta_{wi}}, \tag{34}$$

where K_{water} is molecular conductivity of water (assuming the water is stagnant), and ΔT is the temperature difference

25 between the surface water of the lake and the bottom of the blue ice layer, $T_m - T_s$. This occurs across an assigned length-scale δ_{wi}, for which a value of 0.1-0.5 m is usual, based on the reasoning given in Rogers *et al.* (1995) and the typical vertical water layer resolution of a model simulation (0.125 − 1.5 m). Note that a wide variation in techniques and values is used to

determine the basal heat flux immediately beneath the ice pack (e.g., Harvey, 1990) which suggests that this may need careful consideration during calibration.

5   Figure 6 summarizes the algorithm to update ice cover, snow cover and water depth. The ice cover equations are applied when water temperature first drops below 0 °C. The ice thickness is set to its minimum value of 0.05 m, which is suggested by Patterson and Hamblin (1988) and Vavrus et al. (1996). The need for a minimum ice thickness relates primarily to horizontal variability of ice cover during the formation and closure periods. The ice cover equations are discontinued and open water conditions are restored in the model when the thermodynamic balance first produces ice thickness < 0.05 m.
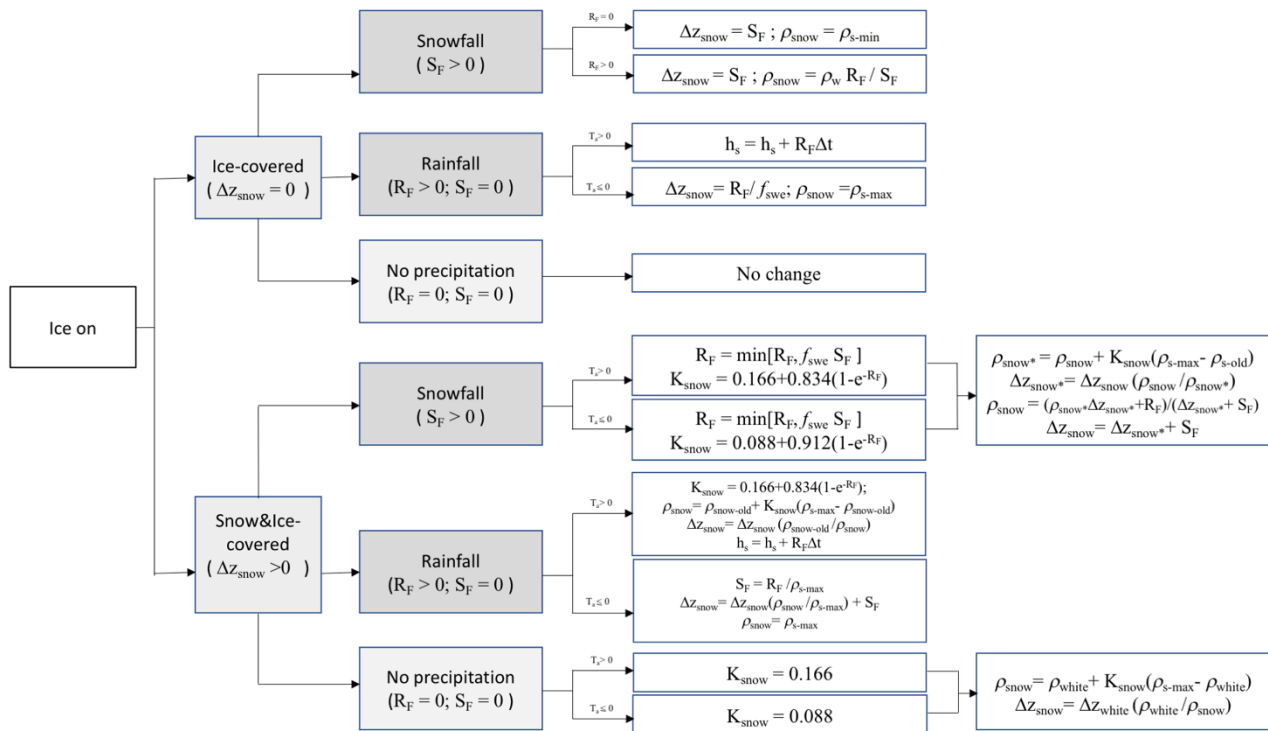
10

Figure 6: Decision tree to update snow cover and water depth according to snow compaction, rainfall (R_F) and snowfall (S_F) each time step. Refer to text and Table 1 for definitions of other variables.

15   After the change in ice thickness due to heat exchange is calculated, the effects of snowfall, rainfall, and compaction of snow are calculated through appropriate choice of one of several options, depending on the air temperature and whether ice or snow is the upper solid boundary (Figure 6). Density of fresh snowfall is determined as the ratio of measured snowfall height to water-equivalent height, with any values exceeding the assigned maximum or minimum snow density (defaults: $\rho_{s,max}$ = 300 kg m^{-3}, $\rho_{s,min}$ = 50 kg m^{-3}) truncated to the appropriate limit. The snow compaction model is based on the exponential decay

20   formula of McKay (1968), with selection of snow compaction parameters based on air temperature (Rogers et al., 1995) as well as on rainfall or snowfall. The approach of snow compaction used by Rogers et al. (1995) is to set the residual snow

Revision 8 Mar 2018

density to its maximum value when there is fresh snowfall. This method is found to produce increases in snow density that are too rapid when there is only light snowfall. As a result, GLM uses a gradual approach where the new snowfall and the existing snow is used to form a layer with a combined mass and average density. Example outputs are shown in Figure 7, and see also Yao et al. (2014) for a previous application.

5
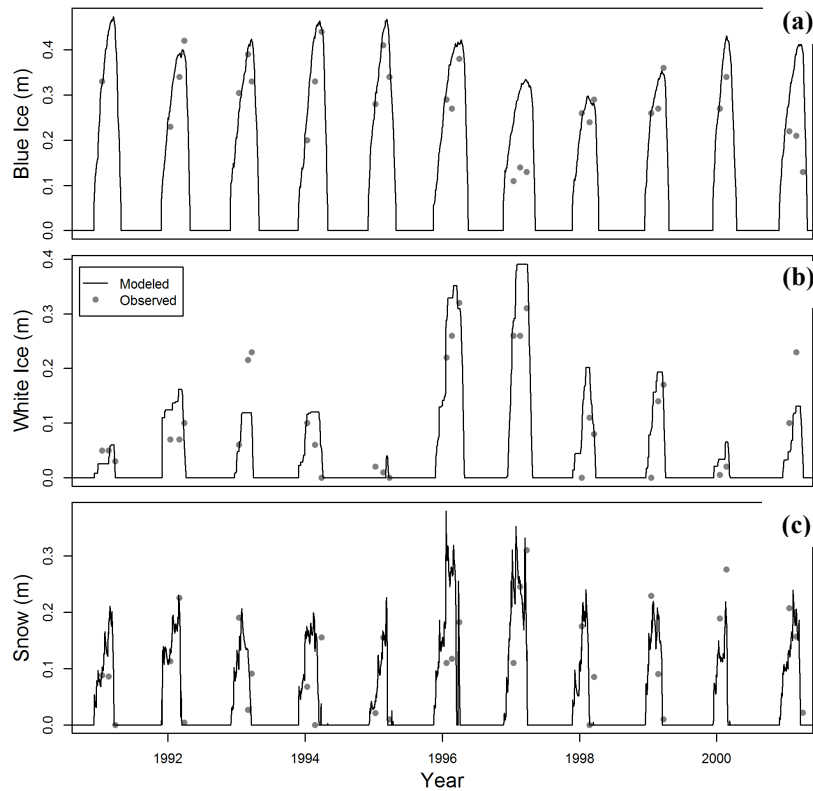
Figure 7: Example of modelled and observed thickness of (a) blue ice, Δz_{blue}, (b) white ice, Δz_{white}, and (c) snow, Δz_{snow}, for Sparkling Lake, Wisconsin. Lines are modelled thickness and points are average observed thicknesses.

10 **2.5 Sediment heating**

The water column thermal budget may also be affected by heating or cooling from the soil/sediment below. For each layer, the rate of temperature change depends on the temperature gradient and the relative area of the layer volume in contact with bottom sediment:

$$c_w \rho_i \, \Delta V_i \frac{dT_i}{dt} = K_{soil} \frac{(T_{z_i} - T_i)}{\delta z_{soil}} \, (A_i - A_{i-1}) \tag{35}$$

where K_{soil} is the soil/sediment thermal conductivity and δz_{soil} is the length scale associated with the heat flux. The

15 temperature of the bottom sediment varies seasonally, and also depending on its depth below the water surface, such that:

18

Geoscientific
Model Development
Discussions

Revision 8 Mar 2018

$$T_{z_i} = T_{z_{mean}} + \delta T_z \cos\left[\frac{2\pi}{365}\left(d - d_{T_z}\right)\right] \tag{36}$$

where z is the soil/sediment zone that the i [th] layer overlays (see Section 4 for details), T_{z_i}, is the temperature of this zone, $T_{z_{mean}}$ is the annual mean sediment zone temperature, δT_z is the seasonal amplitude of the soil temperature variation, and d_{T_z} is the day of the year when the soil temperature peaks. By defining different sediment zones, the model can therefore allow for a different mean and amplitude of littoral waters compared to deeper waters. A dynamic sediment temperature diffusion

5   model is also under development, which will be available when empirical data for the above parameters in Eq 36 is not possible.

2.6 Stratification and vertical mixing

2.6.1 Surface mixed layer

To compute mixing of layers, GLM works on the premise that the balance between the available energy, E_{TKE}, and the energy required for mixing to occur, E_{PE}, provides for the surface mixed layer (sml) deepening rate dz_{sml}/dt, where z_{sml} is the

10   thickness of the surface mixed layer. For an overview of the dynamics, readers are referred to early works on bulk mixed layer depth models by Kraus and Turner (1967) and Kim (1976), which were subsequently extended by Imberger and Patterson (1981) as a basis for hydrodynamic model design. Using this approach, the available kinetic energy is calculated due to contributions from wind stirring, convective overturn, shear production between layers, and Kelvin-Helmholtz (K-H) billowing. They may be combined and summarised for E_{TKE} as (Hamilton and Schladow, 1997):

$$E_{TKE} = \underbrace{0.5 C_K (w_*^3)\,\Delta t}_{convective\ overturn} + \underbrace{0.5 C_K (C_W\, u_*^3)\,\Delta t}_{wind\ stirring} + \underbrace{0.5\, C_S \left[u_b^2 + \frac{u_b^2}{6}\frac{d\delta_{KH}}{dz_{sml}} + \frac{u_b \delta_{KH}}{3}\frac{du_b}{dz_{sml}}\right]}_{\substack{shear\ production \\ K-H\ production}} \Delta z_{k-1} \tag{37}$$

15   where δ_{KH} is the K-H billow length scale (described below), u_b is the shear velocity at the interface of the mixed layer, and C_K, C_W, and C_S are mixing efficiency constants. For mixing to occur, the energy must be sufficient to lift up water in the layer below the bottom of the mixed layer, denoted here as the layer $k - 1$, with thickness Δz_{k-1}, and accelerate it to the mixed layer velocity, u_*. This also accounts for energy consumption associated with K-H production and expressed as, E_{PE}:

$$E_{PE} = \left[\underbrace{0.5 C_T (w_*^3 + C_W\, u_*^3)^{2/3}}_{acceleration} + \underbrace{\frac{\Delta\rho}{\rho_o} g\, z_{SML}}_{lifting} + \underbrace{\frac{g\delta_{KH}^2}{24\rho_o}\frac{d(\Delta\rho)}{dz_{sml}} + \frac{g\delta_{KH}\Delta\rho}{12\rho_o}\frac{d\delta_{KH}}{dz_{sml}}}_{K-H\ consumption}\right]\Delta z_{k-1} \tag{38}$$

20   To numerically resolve Eq 37 and 38 the model sequentially computes the different components of the above expressions with respect to the layer structure, checking the available energy relative to the required amount. GLM follows the sequence of the algorithm presented in detail in Imberger and Patterson (1981), whereby layers are combined due to convection and wind stirring first, and then the resultant mixed layer properties are used when subsequently computing the extent of shear mixing and the effect of K-H instabilities. Plots indicating the role of mixing in shaping the thermal structure of the exmaple lakes are

25   shown in Figure 8.

To compute the mixing energy available due to convection, in the first step, the value for w_* is calculated, which is the turbulent velocity scale associated with convection brought about by cooling at the air-water interface. The model adopts the algorithm

Geoscientific
Model Development
Discussions

Revision 8 Mar 2018

used in Imberger and Patterson (1981), whereby the potential energy that would be released by mixed layer deepening is computed as the difference in the moments of the layers in the epilimnion (surface mixed layer) about the lake bottom, which is numerically computed by summing from the bottom-most layer of the epilimnion, k, up to N_{LEV}:

$$w_*^3 = \frac{g}{\rho_{sml} \, \Delta t} \left(\sum_{i=k}^{N_{LEV}} [\rho_i \, \Delta z_i \, \widetilde{h_i}] - \widetilde{h_{sml}} \sum_{i=k}^{N_{LEV}} [\rho_i \, \Delta z_i \,] \right) \tag{39}$$

where ρ_{sml} is the mean density of the mixed layer including the combined layer, ρ_k is the density of the kth layer, Δz_i is the height difference between two consecutive layers within the loop ($\Delta z_i = h_i - h_{i-1}$), $\widetilde{h_i}$ is the mean height of layers to be mixed ($\widetilde{h_i} = 0.5[\,h_i + h_{i-1}\,]$), and $\widetilde{h_{sml}}$ is the epilimnion mid height, calculated as: $\widetilde{h_{sml}} = 0.5(h_s + h_{k-1})$.

The velocity scale u_* is associated with wind stress and calculated according to the wind strength:

$$u_*^2 = C_D U_{10}^2 \tag{40}$$

where C_D is the drag coefficient for momentum. The model first checks to see if the energy available from Eqs. (39) and (40) can overcome the energy required to mix the $k-1$ layer into the surface mixed layer; i.e., mixing of $k-1$ occurs if:

$$C_K(w_*^3 + C_W \, u_*^3) \, \Delta t \geq \left(g_k' \, z_{SML} + C_T (w_*^3 + C_W \, u_*^3)^{2/3} \right) \Delta z_{k-1} \tag{41}$$

where $g_k' = \frac{\Delta \rho}{\rho_o}$ is the reduced gravity between the mixed layer and the $k-1$ layer, calculated as $(\rho_{sml} - \rho_{k-1})/(0.5(\rho_{sml} + \rho_{k-1}))$. If the mixing condition is met the layers are combined, the energy required to combine the layer is removed from the available energy, k is adjusted, and the loop continues to the next layer. Where the mixing energy is substantial and the mixing reaches the bottom layer, then the mixing routine ends. If the condition in Eq. 41 is not met, then the energy is stored for the next time step, and the mixing algorithm continues as outlined below.

Once stirring is completed, mixing due to velocity shear is applied. Parameterising the shear velocity in a one-dimensional model is difficult but the approximation used in Imberger and Patterson (1981) is applied as:

$$u_b = \begin{cases} \dfrac{u_*^2 t}{z_{sml}} + u_{b_{old}}, & t \leq t_b + \delta t_{shear} \\ 0, & t > t_b + \delta t_{shear} \end{cases} \tag{42}$$

such that there is a simple linear increase in the shear velocity over time for a constant wind stress, considered relative to t_{shear}, which is the cut-off time; beyond this time it is assumed no further shear-induced mixing occurs for that event. The velocity $u_{b_{old}}$, is from the previous time step, and zeroed between shear events. This cut-off time assumes use of only the energy produced by shear at the interface during a period equivalent to half the basin-scale seiche duration, δt_{iw}, which can be modified to account for damping (Spigel, 1978):

$$\delta t_{shear} = \begin{cases} 1.59 \, \delta t_{iw} & \dfrac{\delta t_{damp}}{\delta t_{iw}} \geq 10 \\ \left(1 + 0.59 \left[1 - cosh \left(\dfrac{\delta t_{damp}}{\delta t_{iw}} - 1 \right)^{-1} \right] \right) \delta t_{iw} & \dfrac{\delta t_{damp}}{\delta t_{iw}} < 10 \end{cases} \tag{43}$$
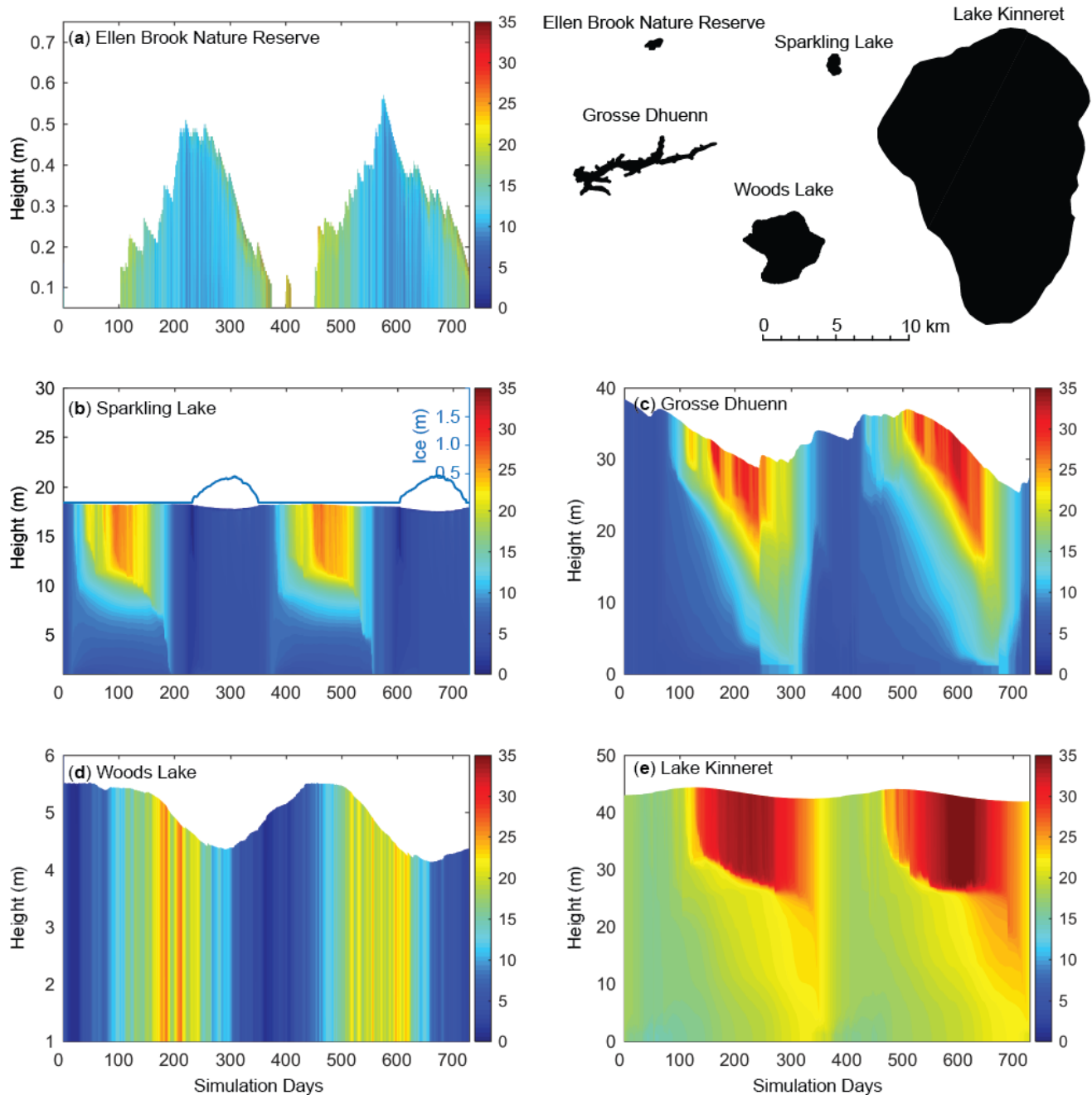
Figure 8: A two-year time-series of the simulated temperature profiles for five example lakes, a-e, that range in size and hydrology. For more information about each lake and the simulation configuration refer to the Data availability section (refer also to Fig. 2 and 5). Sparkling Lake (d) also indicates the simulated depth of ice on the RHS scale.

Revision 8 Mar 2018

where δt_{damp} is the time scale of damping. The wave period is approximated based on the stratification as $\delta t_{iw} = L_{META}/2c$, where L_{META} is the length of the basin at the thermocline, calculated from $\sqrt{A_{k-1}(4/\pi)(L_{crest}/W_{crest})}$, and c is the internal wave speed:

$$c = \sqrt{|g'_{EH}| \frac{\delta_{epi}\delta_{hyp}}{(\delta_{epi} + \delta_{hyp})}} \qquad (44)$$

where δ_{epi} and δ_{hyp} are characteristic vertical length scales associated with the epilimnion and hypolimnion:

$$\delta_{epi} = \frac{\Delta V_{epi}}{0.5(A_s + A_{k-1})} \; ; \; \delta_{hyp} = \frac{V_{k-1}}{0.5 A_{k-1}} \qquad (45)$$

5

The time for damping of internal waves in a two-layer system can be parameterised by estimating the length scale of the oscillating boundary layer, through which the wave energy dissipates, and the period of the internal standing wave (see Spigel and Imberger, 1980):

$$\delta t_{damp} = \frac{\sqrt{\nu_w}}{c_{damp}\,\delta_{ss}} \frac{2(\delta_{epi} + \delta_{hyp})}{u_*^2} \sqrt{\frac{c}{2\,L_{META}}} \frac{\delta_{hyp}}{\delta_{epi}} (\delta_{epi} + \delta_{hyp}) \qquad (46)$$

10 Once the velocity is computed from Eq. 42, the energy for mixing from velocity shear is compared to that required for lifting and accelerating the next layer down, and layers are combined if there is sufficient energy, *i.e.* when:

$$0.5\,C_S \left[\frac{u_b^2(\widetilde{z_{sml}} + \Delta\delta_{KH})}{6} + \frac{u_b \delta_{KH}\Delta u_b}{3} \right] + \left[g'_k \delta_{KH} \left(\frac{\delta_{KH}\Delta z_{k-1}}{24 z_{SML}} - \frac{\Delta\delta_{KH}}{12} \right) \right] \qquad (47)$$

$$\geq \left(g'_k\, z_{sml} + C_T(w_*^3 + C_W\, u_*^3)^{2/3} \right)\Delta z_{k-1}$$

where the billow length scale is $\delta_{KH} = C_{KH}u_b^2/g'_{EH}$ and $\Delta\delta_{KH} = 2\,C_{KH}\,u_b\,\Delta u_b/g'_{EH}$; in this case the reduced gravity is computed from the difference between the epilimnion and hypolimnion, and C_{KH} is a measure of the billow mixing efficiency.

15

Once shear mixing is done, the model checks the resultant density interface to see if it is unstable to shear, such that K-H billows would be expected to form, i.e., if the metalimnion thickness is less than the K-H length scale, δ_{KH}. If K-H mixing is required, layers are further split and a linear density profile is set over the metalimnion.

20 **2.6.2 Deep mixing**

Mixing below the epilimnion in lakes, in the deeper stratified regions of the water column, is modelled using a characteristic vertical diffusivity, $D_Z = D_\varepsilon + D_m$, where D_m is a constant molecular diffusivity for scalars and D_ε is the turbulent diffusivity. Three hypolimnetic mixing options are possible in GLM including: (1) no diffusivity, $D_Z = 0$, (2) a constant vertical diffusivity D_Z over the water depth below the thermocline or (3) a derivation by Weinstock (1981) used in DYRESM, which is described

Revision 8 Mar 2018

as being suitable for regions displaying weak or strong stratification, whereby diffusivity increases with dissipation and decreases with heightened stratification.

For the constant vertical diffusivity option, the coefficient α_{TKE} is interpreted as the vertical diffusivity (m² s⁻¹), i.e., $D_z =$
5   C_{HYP}. For the Weinstock (1981) model, the diffusivity is computed according to:

$$D_z = \frac{C_{HYP}\,\varepsilon_{TKE}}{N^2 + 0.6\,k_{TKE}^2\,u_*^2} \tag{48}$$

where C_{HYP} in this case is the mixing efficiency of hypolimnetic TKE (~0.8 in Weinstock, 1981) and u_* is defined as above. N^2 is the Brunt–Väisälä (buoyancy) frequency defined for a given layer as:

$$N^2{}_i = \frac{g\Delta\rho}{\rho\Delta z} \approx \frac{g(\rho_{i+2} - \rho_{i-2})}{\rho_{ref}(h_{i+2} - h_{i-2})} \tag{49}$$

where ρ_{ref} is the average of the layer densities. This is computed from layer 3 upwards, averaging over the span of 5 layers, until the vertical density gradient exceeds a set tolerance. k_{TKE} is the turbulence wavenumber:

$$k_{TKE}^2 = \frac{c_{wn}\,A_s}{\tilde{V}_{N^2}\,\Delta z_{sml}} \tag{50}$$

10   where $\tilde{V}_{N^2}$ is a fractional volume of the lake that contains 85% of N^2. The turbulent dissipation rate can be complex in stratified lakes, however, GLM adopts a simple approach as described in Fischer et al. (1979) where a "net dissipation" is approximated by assuming dissipation is in equilibrium with energy inputs from external drivers:

$$\varepsilon_{TKE} \approx \overline{\varepsilon_{TKE}} = \varepsilon_{WIND} + \varepsilon_{INFLOW} \tag{51}$$

which is expanded and calculated per unit mass as:

$$\overline{\varepsilon_{TKE}} = \underbrace{\frac{1}{\tilde{V}_{N^2}\,\bar{\rho}}\,m\,C_D\,\rho_a\,U_{10}^3\,A_s}_{\text{rate of working by wind}} + \underbrace{\frac{1}{(\tilde{V}_{N^2} - \Delta V_s)\,\bar{\rho}}\sum_I^{N_{INF}} g\left(\rho_{ins_I} - \rho_{i_{ins_I}}\right) Q_{inf_{ins_I}}\left(\left(h_s - z_{inf_{ins_I}}\right) - h_{i_{ins_I}-1}\right)}_{\text{rate of work done by inflows}} \tag{52}$$

where $\bar{\rho} = 0.5(\rho_1 + \rho_{N_{LEV}})$ is the mean density of the water column. The work done by inflows is computed based on the
15   flow rate, the depth the inflow plunges to, and the density difference, summed over all configured inflows.

Since the dissipation is assumed to concentrate close to the level of strongest stratification, the "mean" diffusivity from Eq. 48 is modified to decay exponentially within the layers as they increase their distance from the thermocline:

$$D_{Z_i} = \begin{cases} 0 & h_i \geq (h_s - z_{sml}) \\ D_z\,exp\left[\dfrac{-(h_s - z_{sml} - h_i)^2}{\sigma}\right] & h_i < (h_s - z_{sml}) \end{cases} \tag{53}$$

where σ is the variance of the N^2 distribution below the bottom of the mixed layer, $h_s - z_{sml}$, and this scales the depth over
20   which the mixing is assumed to decay.

Once the diffusivity is approximated (for either model 1 or 2), the diffusion of any scalar, C (including salinity), between two layers is numerically accounted for by the following mass transfer expressions:

Revision 8 Mar 2018

$$C_{i+1} = \bar{C} + e^{-f} \frac{\Delta z_i \Delta C}{(\Delta z_{i+1} + \Delta z_i)}$$

(54a,b)

$$C_i = \bar{C} - e^{-f} \frac{\Delta z_{i+1} \Delta C}{(\Delta z_{i+1} + \Delta z_i)}$$

where $\bar{C}$ is the weighted mean concentration of C for the two layers, and ΔC is the concentration difference between them. The smoothing function, f_{dif}, is related to the diffusivity according to:

$$f_{dif} = \frac{D_{z_{i+1}} + D_{z_i}}{(\Delta z_{i+1} + \Delta z_i)^2} \Delta t$$

(55)

and the above diffusion algorithm is run once up the water column and once down the water column as a simple explicit method for capturing diffusion of mass to both the upper and lower layers. An example of the effect of hypolimnetic mixing

5   on a hypothetical scalar concentration released into the hypolimnion is shown in Figure 9.
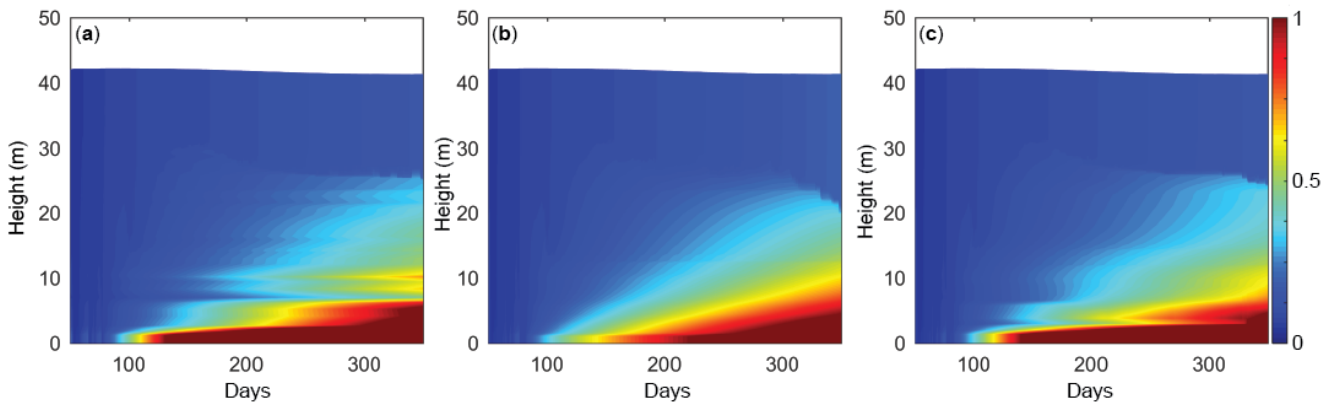

Figure 9: Example simulations for Lake Kinneret showing the hypolimnetic concentration of a passive tracer (normalised units) released from the sediment into the bottom layer at a constant rate for the case: a) without deep mixing, b) constant vertical diffusivity, $D_z = 2 \times 10^{-6}$ m² s⁻¹, and c) calculated vertical diffusivity (Eq. 48). The thermal structure for this case is in Figure 8c.

10

2.7 Inflows and outflows

Aside from the surface fluxes of water described above, the water balance of a lake is controlled by the specifics of the inflows and outflows. Inflows can be specified as local runoff from the surrounding (dry) lake domain (Q_R described separately above, Eq. 7), rivers entering at the surface of the lake that will be buoyant or plunge depending on their momentum and density

15   (Section 2.7.1), or submerged inflows (including groundwater) that enter at depth (Section 2.7.2). Four options for outflows are included in GLM. These include withdrawals from a specified depth (Section 2.7.3), adaptive offtake (Section 2.7.4), vertical groundwater seepage (Section 2.7.5), and river outflow/overflow from the surface of the lake (Section 2.7.6). Any number of lake inflows and outflows can be specified and, except for the local runoff term, all applied at a daily time step. Depending on the specific settings of each, these water fluxes can impact the volume of the individual layers, ΔV_i, as well as

20   the overall lake volume.

2.7.1 River inflows

As water from an inflowing river connects with a lake or reservoir environment, it will form a positively or negatively buoyant intrusion depending on the density of the incoming river water in the context of the water column stratification. As the inflow progresses towards insertion, it will entrain water at a rate depending on the turbulence created by the inflowing water mass

5 (Fischer et al., 1979). For each configured inflow the characteristic rate of entrainment of the intrusion, E_{inf}, is computed using the approximation given in Fischer et al. (1979):

$$E_{inf} = 1.6 \frac{C_{D_{inf}}^{3/2}}{Ri_{inf}} \tag{56}$$

where $C_{D_{inf}}$ is the user-specified drag coefficient for the inflow. The inflow Richardson number, Ri_{inf}, characterises the stability of the water in the context of the inflow channel geometry (Fischer et al., 1979), computed as:

$$Ri_{inf} = \frac{C_{D_{inf}} \left(1 + 0.21 \sqrt{C_{D_{inf}}} \sin \alpha_{inf}\right)}{\sin \alpha_{inf} \tan \Phi_{inf}} \tag{57}$$

where α_{inf} is the stream half angle and ϕ_{inf} is the tangent of the slope of the inflow, at the point where it meets the water

10 body (Figure 10).
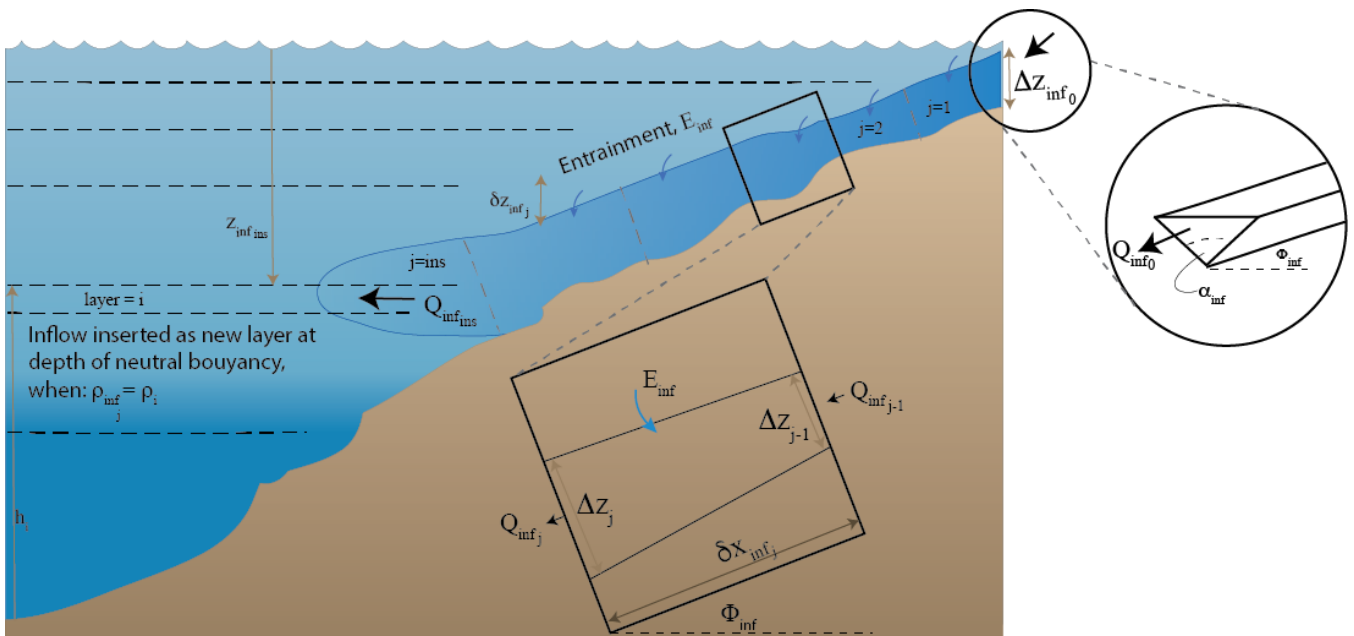
Figure 10: Schematic showing inflow insertion depth, entrainment, E_{inf}, slope, Φ_{inf} and half angle, α_{inf} of an inflowing river
15 **entering with a prescribed flow of Q_{inf_0}, and estimated starting thickness of Δz_{inf_0}.**

The inflow algorithm captures two phases: first, the inflowing water crosses the layers of the lake until it reaches a level of neutral buoyancy, and second, it then undergoes insertion. In the first part of the algorithm, the daily inflow parcel is tracked

Revision 8 Mar 2018

down the lake-bed and its mixing with layers is updated until it is deemed ready for insertion. The initial estimate of the intrusion thickness, Δz_{inf_0}, is computed from Antenucci et al. (2005):

$$\Delta z_{inf_0} = \left(2\ \frac{Ri_{inf}}{g'_{inf}} \left(\frac{Q_{inf_0}}{tan\ \Phi_{inf}} \right)^2\ \right)^{1/5} \tag{58}$$

where $Q_{inf_0} = f_{inf}\ Q_{inf_x}/c_{secday}$ is the inflow discharge entering the domain, based on the data provided as a boundary condition, Q_{inf_x}, and g' is the reduced gravity of the inflow as it enters:

$$g'_{inf} = g\ \frac{(\rho_{inf} - \rho_s)}{\rho_s} \tag{59}$$

5   where ρ_{inf} is the density of the inflow, computed from the supplied inflow properties of temperature and salinity (T_{inf_x}, S_{inf_x}), and ρ_s is the density of the surface layer. If the inflowing water is deemed to be positively buoyant $(\rho_{inf} < \rho_s)$, or the model only has one layer ($N_{LEV} = 1$), then the inflow water over the daily time step is added to the surface layer volume ($\Delta V_{N_{LEV}} = Q_{inf_0}\ \Delta t_d$), and h_s is updated accordingly. Otherwise, this inflow volume is treated as a parcel which travels down through the lake layers, and its properties are subsequently incremented over each daily time step, j, until it inserts. The

10   thickness of an inflow parcel increases over each increment due to entrainment, assuming:

$$\Delta z_{inf_j} = 1.2\ E_{inf}\ \Delta x_{inf_j} + \Delta z_{inf_{j-1}} \tag{60}$$

where Δz_{inf_j} is the inflow thickness and Δx_{inf_j} is the distance travelled by the inflowing water parcel in the time step. The distance travelled is estimated based on the change in the vertical elevation of the inflow, δz, and the slope of the inflow river, ϕ_{inf}, as given by:

$$\Delta x_{inf_j} = \frac{\delta z_{inf_{j-1}}}{\sin \Phi_{inf}} \tag{61}$$

where, $\delta z_{inf_j} = \left(h_s - z_{inf_j} \right) - h_{i_j-1}$, and the depth of the inflow from the surface is $z_{inf_j} = z_{inf_{j-1}} + \Delta x_{inf_j} \sin \Phi_{inf}$. The

15   average velocity of the inflow parcel for that increment is calculated from:

$$u_{inf_j} = Q_{inf_j} \frac{\tan \alpha_{inf}}{\left(\Delta z_{inf_j} \right)^2} \tag{62}$$

where the numerator links the relationship between inflow height and channel width in order to define the cross-sectional area of the flow. This velocity is used to estimate the time scale of transport of the parcel ($\delta t_d = \Delta x_{inf_j}/u_{inf_j}$). Following conservation of mass, the flow is estimated to increase according to Fischer et al. (1979) (see also Antenucci et al. 2005):

$$\Delta Q_{inf_j} = Q_{inf_{j-1}} \left[\left(\frac{\Delta z_{inf_j}}{\Delta z_{inf_{j-1}}} \right)^{5/3} - 1 \right] \tag{63}$$

20

whereby ΔQ_{inf_j} is removed from the volume of the corresponding layer, i_j, and added to the previous time-step inflow $Q_{inf_{j-1}}$ to capture the entrainment effect on the inflow. The inflow travel algorithm (Eq. 63) increments through j until the density of

Revision 8 Mar 2018

the inflow reaches its depth of neutral buoyancy: $\rho_{inf_j} \leq \rho_{i_j}$. Once this condition is met, the second part of the algorithm creates a new layer of thickness dependent on the inflow volume at that time (including the successive additions from entrainment; Eq. 60).

5 Note that a new inflow parcel is created each day, and the user may configure multiple inflows, N_{INF}, creating a complex set of parcels being tracked via Eqs 56-63, and a queue of new layers to be inserted. Following creation of a new layer for the inflow parcel, N_{LEV} is incremented and all layer heights are updated. The new inflow layer is then subject to the thickness limits criteria within the layer limit checking routine and may amalgamate with adjacent layers for combining or splitting layers.

10

Aside from importing mass into the lake, river inflows also contribute turbulent kinetic energy to the hypolimnion, as discussed in Sect 2.6.2 (e.g., see Eq. 49), and contribute to the scalar transport in the water column by adding mass and contributing to mixing (Figure 11a).

2.7.2 Submerged inflows

15 Submerged inflows are inserted at the user-specified depth with zero entrainment by utilising the second part of the algorithm described in Section 2.7.1. The submerged inflow volume is added as a new layer which may then be mixed with adjacent layers (above or below) depending on the density difference and layer thickness criteria (Figure 11b). This option can be used across one or more inflow elevations to account for groundwater input to a lake, or for capturing a piped inflow, for example.
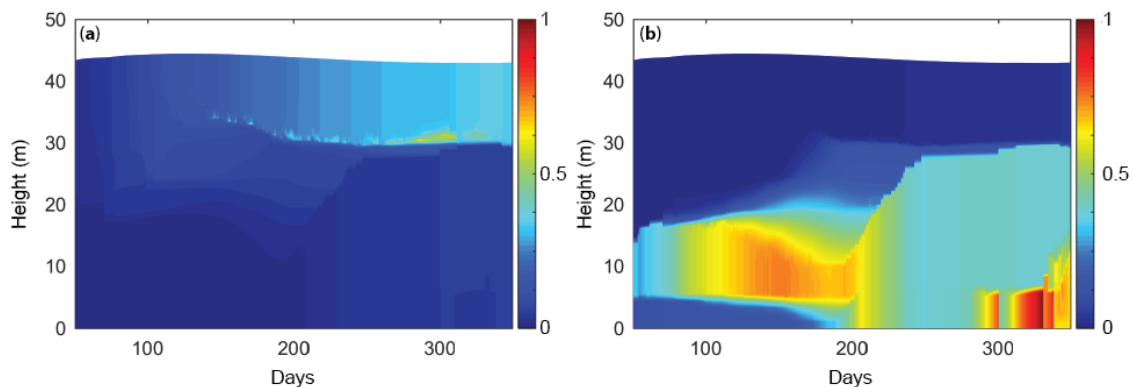
Figure 11: Example simulations demonstrating inflow insertion example for the case where a) the inflow was set as a surface river inflow and subject to the insertion algorithm (Eqs 56-63) prior to insertion, and b) the inflow was set as a submerged inflow at a specified height (h_{inf} = 5m). Once entering the water column, the tracer, C, is subject to mixing during inflow entrainment in case (a), and by surface and/or deep mixing once inserted, for both cases (a) and (b). The colour scale represents an arbitrary inflow concentration which entered with a value of 1.

Geoscientific
Model Development
Discussions

Revision 8 Mar 2018

2.7.3 Withdrawals

Outflows from a specific depth can include outlets from a dam wall offtake or other piped withdrawal, or removal of water that may be lost due to groundwater recharge or seepage to an outflow. For a stratified water column, the water will be removed from the layer corresponding to the specified withdrawal height, h_{outf}, as well as layers above or below, depending on the

5   strength of discharge and stability of the water column. Accordingly, the model assumes an algorithm where the thickness of the withdrawal layer is dependent on the internal Froude (Fr) and Grashof (Gr) numbers, and the parameter, R (see Fischer et al., 1979; Imberger and Patterson, 1981):

$$Fr = \frac{f_{outf} \; Q_{outf_x}/c_{secday}}{N_{outf} \; W_{outf} \; L_{outf}^2} \tag{64}$$

$$Gr = \frac{N_{outf}^2 A_{outf}^2}{D_{outf}^2} \tag{65}$$

$$R = Fr Gr^{1/3} \tag{66}$$

where W_{outf}, L_{outf} and A_{outf} are the width, length and area of the lake at the outlet elevation, and D_{outf}^2 is the vertical diffusivity averaged over the layers corresponding to the withdrawal thickness, δ_{outf} (described below). To calculate the width

10   and length of the lake at the height of the outflow, it is assumed, firstly, that the lake shape can be approximated as an ellipse, and secondly, that the ratio of length to width at the height of the outflow is the same as that at the lake crest. The length of the lake at the outflow height, L_{outf} and the lake width, W_{outf} are given by:

$$L_{outf} = \sqrt{A_{outf} \frac{4}{\pi} \frac{L_{crest}}{W_{crest}}} \tag{67}$$

$$W_{outf} = L_{outf} \frac{W_{crest}}{L_{crest}} \tag{68}$$

where A_{outf} is the area of the lake at the outflow height, L_{crest} is the length and W_{crest} the width of the lake at the crest height.

15   The thickness of the withdrawal layer is calculated depending on the value of R (Fischer et al. 1978), such that:

$$\delta_{outf} = \begin{cases} 2L_{outf} \; Gr^{-1/6} & R \leq 1 \\ 2L_{outf} \; Fr^{1/2} & R > 1 \end{cases} \tag{69}$$

If stratification is apparent near h_{outf}, either above or below this elevation, then the thickness computed in Eq 69 may not be symmetric about the offtake level (Imberger and Patterson, 1981); therefore the algorithm separately computes the thickness of the withdrawal layer above and below, denoted $\delta_{outf_{top}}$ and $\delta_{outf_{bot}}$, respectively. The Brunt-Väisälä frequency is averaged over the relevant thickness, N_{outf}^2, and calculated as:

$$N_{outf}^2 = \frac{g}{\delta_{outf}} \frac{\rho_{outf} - \rho_i}{\rho_{outf}} \tag{70}$$

20   where ρ_{outf} is the density of the layer corresponding to the height of the withdrawal, i_{outf}, and ρ_i is the density of the water column at the edge of the withdrawal layer, as determined below. The proportion of water withdrawn from each layer, Q_{outf_i}, either above or below the layer of the outlet elevation, requires identification of the upper and lower-most layer indices

influenced by the outflow, denoted i_{top} and i_{bot}. Once the layer range is defined, Q_{outf_i} is computed for the layers between i_{outf} and i_{top}, and i_{outf} and i_{bot}, by partitioning the total outflow using a function to calculate the proportion of water withdrawn from any layer that fits the region of water drawn in a given time ($Q_{outf_i} = f \left[f_{outf} \, Q_{outf_x} / c_{secday} \, , h_i, h_{i-1}, h_{outf}, \delta_{outf_{bot}}, \delta_{outf_{top}} \right]$; see Imberger and Patterson, 1981, Eq 65). Given that

5   users configure any height for a withdrawal outlet and flow rates of variable strength, the upper ($h_{outf} + \delta_{outf_{top}}$) and lower ($h_{outf} - \delta_{outf_{bot}}$) elevation limits computed by the algorithm are limited to the lake surface layer or bottom layer. Once computed, the volumes are removed from the identified layer set, and their height and volumes updated accordingly. Q_{outf_i} is constrained within the model to ensure no more than 90% of a layer can be removed in a single time step. Depending on the fractional contribution from each of the layers the water is withdrawn from, the water taken will have the associated weighted

10 average of the relevant scalar concentrations (heat, salinity and water quality) which are reported in the outlet file for the particular withdrawal. This routine is repeated for each withdrawal considered, denoted O, and the model optionally produces a summary file of all the outflow water and its properties.

2.7.4 Adaptive offtake dynamics

For reservoir applications, a special outflow option has been implemented that extends the dynamics in Section 2.7.3 to

15 simulate an adaptive offtake or selective withdrawal. This approach is used for accommodating flexible reservoir withdrawal regimes and their effects on the thermal structure within a reservoir. For this option, a target temperature is specified by the user and GLM identifies the corresponding withdrawal height within a predefined (facility) range to meet this target temperature during the runtime of the simulation, i.e., the withdrawal height adaptively follows the thermal stratification in the reservoir. The target temperature can be defined as a constant temperature (e.g., 14 °C) or a time series (via a *.csv file),

20 such as a measured water temperature from an upstream river that could be used to plan environmental releases from the reservoir to the downstream river. The selected height of the adaptive offtake is printed out in a *.txt file for assisting reservoir operation. In addition to the basic adaptive offtake function, GLM can also simulate withdrawal mixing, i.e., water from the adaptive offtake is mixed with water from another predefined height (e.g., the bottom outlet). For this option, the discharges at both locations need to be predefined by the user (via the standard outflow *.csv files) and GLM chooses the adaptive

25 withdrawal from a height, where the water temperature is such that the resulting mixing temperature meets the target temperature. This withdrawal mixing is a common strategy in reservoir operation where deep water withdrawal and temperature control are required simultaneously to prevent deleterious downstream impacts.

An example of the adaptive offtake function with and without withdrawal mixing, assuming a constant water temperature of

30 14 °C for the outflow water, shows that GLM is able to deliver a constant outflow temperature of 14 °C during the stratified period (Figure 12). In winter, when the water column is cooler than 14 °C, the model withdraws surface water. The adaptive offtake functionality can be used in a stand-alone mode or also linked to the dissolved oxygen concentration (when operated with the coupled water quality model AED2, see Section 4). In the latter case, the effect of the withdrawal regime on the oxygen dynamics in the hypolimnion can be simulated (see Weber et al., 2017). In this setting, the simulated hypolimnetic

Geoscientific
Model Development
Discussions

Revision 8 Mar 2018

dissolved oxygen concentration at a specified height is checked against a user-defined critical threshold. If the hypolimnetic oxygen falls below the critical threshold, the height of the adaptive offtake will be automatically switched to a defined height (usually deep outlets in order to remove the oxygen-depleted water) to withdraw water from this layer, until the oxygen concentrations have recovered.

5
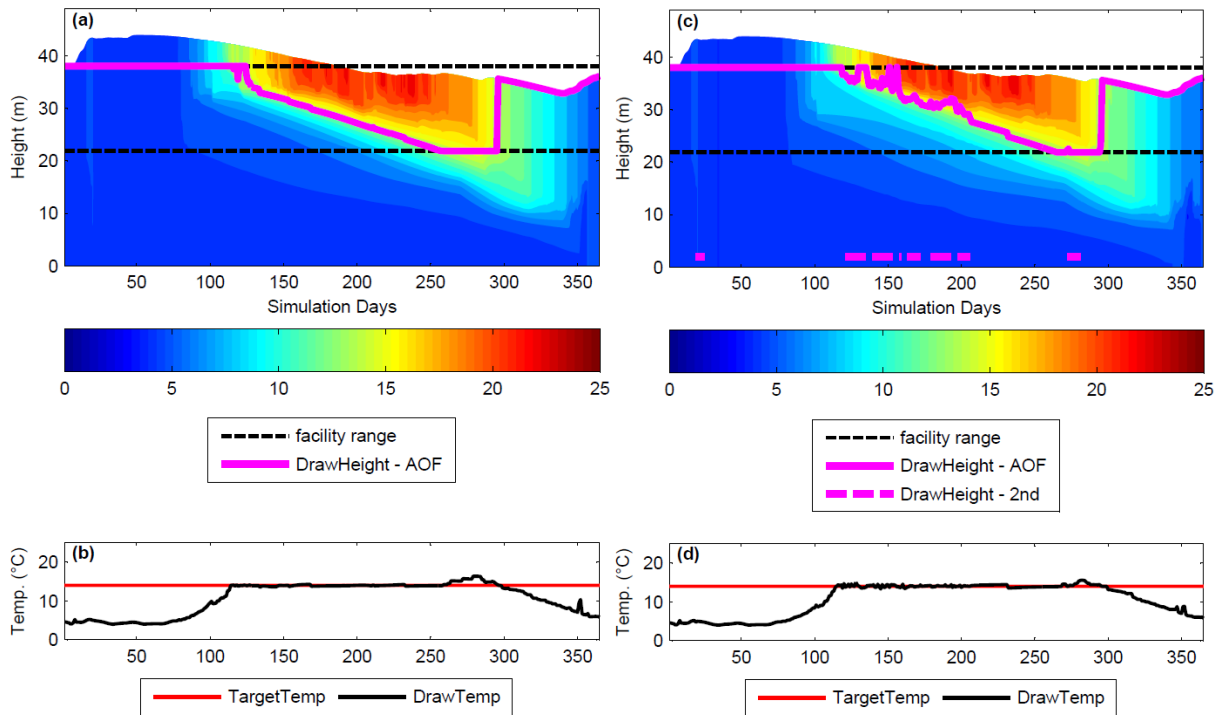
Figure 12: Adaptive offtake reservoir simulation; water temperatures of the adaptive offtake model assuming a constant target temperature of 14 °C (a,b) without and (c,d) with mixing with the bottom outlet withdrawal. The black dashed line (a,c) represents
10 **the height range of the variable withdrawal facility (AOF) and the magenta lines the adaptive offtake and second withdrawal height. Panels (b) and (d) indicate where the actual withdrawal temp (DrawTemp) was able to meet the target (TargetTemp).**

2.7.5 Seepage

Seepage of water from the lake can also be configured within the model, for example, as might be required in a wetland
15 simulation or for small reservoirs perched above the water table that experience leakage to the soil below. The seepage rate, $Q_{seepage}$, can be assumed constant or dependent on the overlying lake head:

$$Q_{seepage} = \begin{cases} -GA_s/c_{secday}, & \text{Option 1: constant rate} \\ -\left(\dfrac{K_{seep}}{\Delta z_{soil}}\right)A_s\,h_s/(c_{secday}), & \text{Option 2: Darcy flux based on water height} \end{cases} \tag{71}$$

where G is the seepage rate (m day^{-1}) and K_{seep} is the soil hydraulic conductivity (m day^{-1}) and Δz_{soil} is an assumed soil thickness over which the seepage is assumed to occur. The water leaving the lake is treated as a "vertical withdrawal" whereby the water exits via the bottom-most layer(s), and the amount $\Delta V_G = Q_{seepage}\Delta t_d$, is generally all taken from the bottom-most

Revision 8 Mar 2018

layer ($i = 1$), however, it is constrained within the model to ensure no more than 90% of the layer can be reduced in any one time step; where $\Delta V_G > 0.9 V_{i=1}$ then the routine sequentially loops up through the above layers until enough lake volume has been identified to cover the seepage demand. Once the individual layer volumes are incremented due to the seepage flux, ΔV_{G_i}, the heights of all layers ($h_1 : h_s$) are re-computed based on the hypsographic curve using $h_i = f[V_i]$. Where seepage reduces the lake below 0.05 m, the lake becomes dry until new inputs from rain or inflows (e.g., Figure 8a).

2.7.6 Overflows

Once the lake volume exceeds the maximum volume, the excess water is assumed to leave the domain as an overflow. The flow rate, Q_{ovfl}, is computed based on the interim volume, V_S^*, prior to the end of the daily time-step, where $V_S^* = V_S^t + \Delta h_s A_s + \Delta t \left(\sum_I^{NINF} Q_{inf_{0_I}} - \sum_O^{NOUT} Q_{outf_O} - Q_{seepage} \right)$. Users can optionally also specify a crest elevation which sits below the elevation of maximum lake volume, and support a rating curve linking the height of water above the crest level with the overflow volume:

$$Q_{weir} = \begin{cases} 0, & V_S^* \leq V_{crest} \\ \frac{2}{3} C_{D_{weir}} \sqrt{2g} \; b \; (h_S^* - h_{crest})^{3/2}, & V_S^* > V_{crest} \end{cases} \tag{72}$$

where h_S^* is the interim update to the water surface height, $C_{D_{weir}}$ is a coefficient related to the drag of the weir, b is the width of the crest and h_{crest} is the height of the crest level. The overflow rate is then computed as the sum of the flow over the weir crest and the volume of water exceeding the volume of the domain:

$$Q_{ovfl} = \begin{cases} Q_{weir}, & V_S^* \leq V_{max} \\ Q_{weir} + (V_S^* - V_{max})/\Delta t_d, & V_S^* > V_{max} \end{cases} \tag{73}$$

2.8 Wave height and bottom stress

Wind induced resuspension of sediment from the bed of shallow lakes is sporadic and occurs as the waves at the water surface create oscillatory currents that propagate down to the lake-bed. GLM does not predict resuspension and sediment concentration directly, but computes the bottom shear stress for later use by sediment and water quality modules. Nonetheless, even without this explicit formulation, the model can identify the areal extent and potential for bed-sediment resuspension by computing the area of the lake over which the bed shear stress exceeds some critical value required for resuspension to occur.

To compute the stress at the lake bottom the model estimates the surface wave conditions using a simple, fetch-based, steady state wave model (Laenen and LeTourneau, 1996; Ji 2008). The wave geometry (wave period, significant wave height and wave length), is predicted based on the wind speed and fetch over which the waves develop (Figure 13). The fetch is approximated from:

$$F = 2\sqrt{A_s/\pi} \tag{74}$$

Revision 8 Mar 2018

and the wave period, δt_{wave}, is calculated from fetch as:

$$\delta t_{wave} = 7.54 \left(\frac{U_{10}}{g} \right) tanh(\xi) \; tanh \left(\frac{0.0379 \left[\frac{gF}{U_{10}^2} \right]^{0.333}}{tanh(\xi)} \right) \tag{75}$$

where:

$$\xi = 0.833 \left[\frac{g z_{avg}}{U_{10}^2} \right]^{0.375} \tag{76}$$

and z_{avg} is the average lake depth. The typical wave length is then estimated from:

$$\delta x_{wave} = \left[\frac{g (\delta t_{wave})^2}{2\pi} \right] tanh \left(\frac{2\pi \, z_{avg}}{\left[\frac{g (\delta t_{wave})^2}{2\pi} \right]} \right) \tag{77}$$

and the significant wave height from:

$$\delta z_{wave} = 0.283 \left(\frac{U_{10}^2}{g} \right) tanh(\zeta) tanh \left(\frac{0.00565 \left[\frac{gF}{U_{10}^2} \right]^{0.5}}{tanh(\zeta)} \right) \tag{78}$$

5   where

$$\zeta = 0.53 \left[\frac{g z_{avg}}{U_{10}^2} \right]^{0.75} \tag{79}$$

Based on these properties the orbital wave velocity at depth (in the $i^{\,th}$ layer) is calculated as:
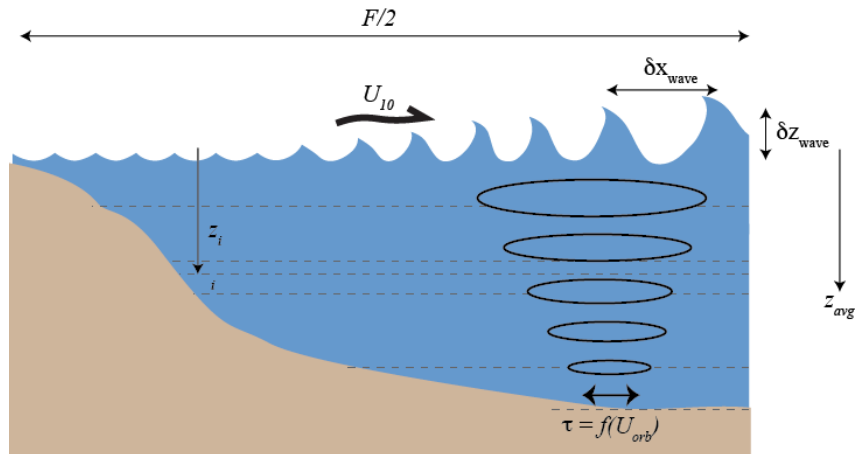
$$U_{orb_i} = \frac{\pi \, \delta z_{wave}}{\delta t_{wave} \; sinh \left[\frac{2\pi \, z_{i-1}}{\delta x_{wave}} \right]} \tag{80}$$

Figure 13: Schematic of the wave estimation approach depicting the lake fetch, surface wind speed, wave height, wavelength and
10   **bottom stress created by the orbital velocity.**

Geoscientific
Model Development
Discussions

Revision 8 Mar 2018

For each layer, the total shear stress experienced at the lake bed portion of that layer (equivalent in area to $A_i - A_{i-1}$) is calculated from:

$$\tau_i = \frac{1}{2} \rho_i \left[f_w U_{orb_i}^2 + f_c U_{m_i}^2 \right] \tag{81}$$

where U_m is the mean layer velocity, which for simplicity is assumed based on the velocity estimate made during the mixing calculations (Eq. 40) in the surface mixed layer, such that:

$$U_{m_i} = \begin{cases} u_*, & i \geq k \\ 0, & i < k \end{cases} \tag{82}$$

5

The friction factors depend upon the characteristic particle diameter of the lake bottom sediments, δ_{ss} and the fluid velocity. For the current induced stress, we compute $f_c = 0.24/\log\left(12 z_{avg}/2.5\delta_{ss_{z_i}}\right)$, and for waves (Kleinhans and Grasmeijer, 2006):

$$f_w = \exp\left[-5.977 + 5.213\left(\frac{U_{orb_i}\,\delta t_{wave}}{5\pi\,\delta_{ss_{z_i}}}\right)^{-0.194}\right] \tag{83}$$

where $\delta_{ss_{z_i}}$ is specific for each layer i, depending on which sediment zone it overlays (see Section 4). The current and wave

10   induced stresses at the lake bottom manifest differently within the lake, as demonstrated in Figure 14 for a shallow lake.
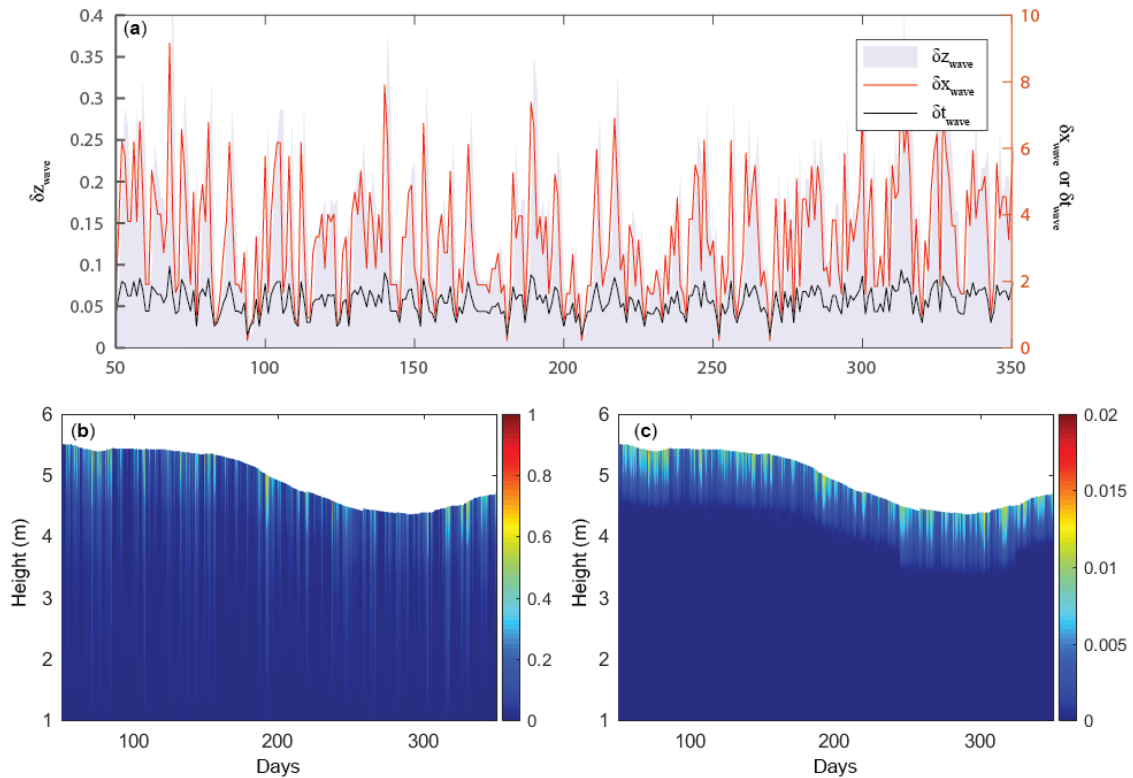
Figure 14: Simulation from Woods Lake, Australia, showing a) time series of surface wave properties (Hs = δz_{wave}, L= δx_{wave} and T= δt_{wave}), b) orbital velocity, U_{orb} (m s^{-1}), and c) comparison with the layer mean velocities, U_m (m s^{-1}).

Geoscientific
Model Development
Discussions

Revision 8 Mar 2018

3 Code organization and model operation

Aside from the core water balance and mixing functionality, the model features numerous options and extensions in order to make it a fast and easy-to-use package suitable for a wide range of contemporary applications. Accommodating these requirements has led to the modular code structure outlined in Figure 15. The model is written in C, with a Fortran-based interface module to link with Fortran-based water quality modelling libraries described in Section 4. The model compiles with gcc, and gfortran, and commercial compilers, with support for Windows, OS X and Linux.
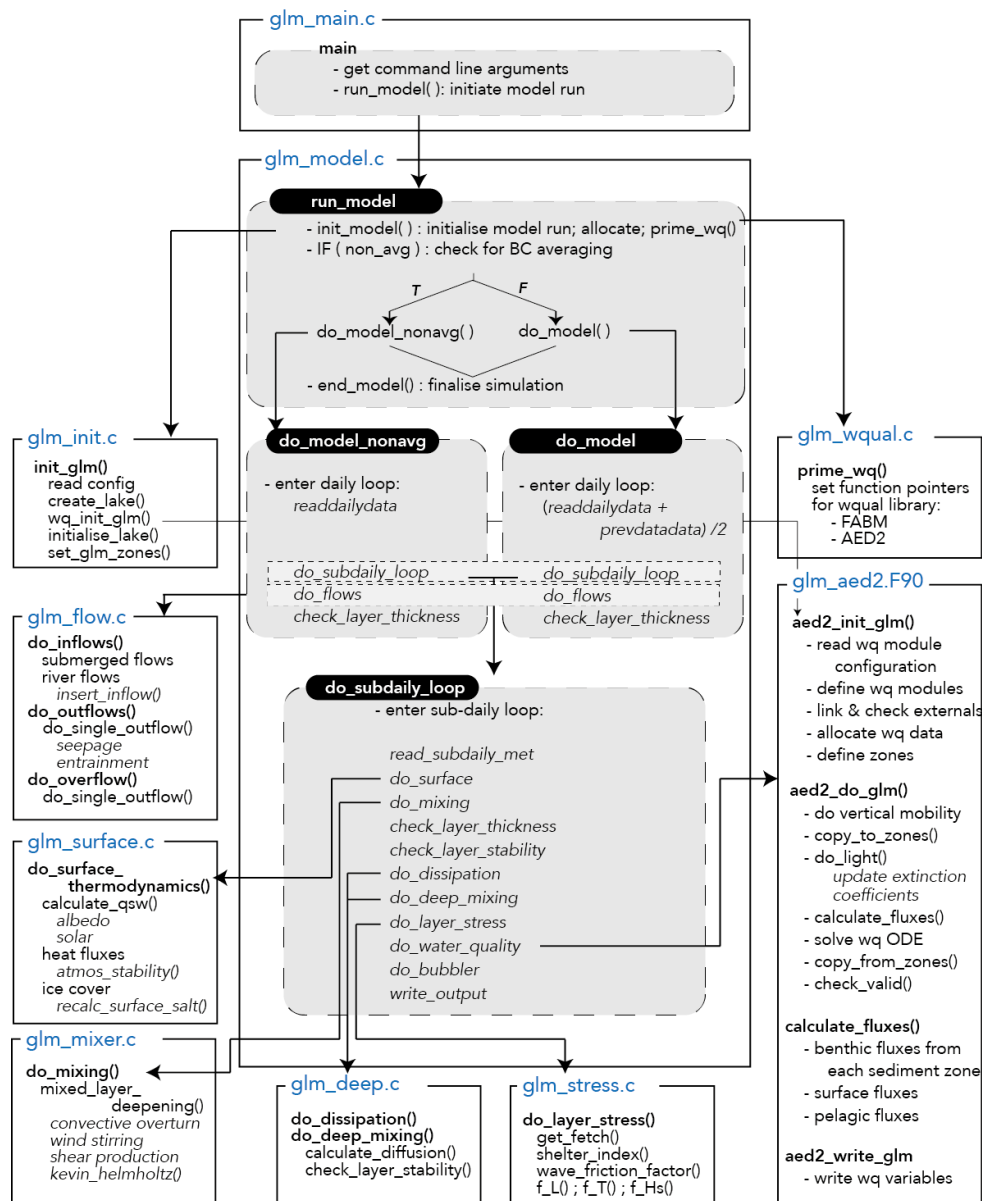
Figure 15: GLM code structure and logic flow. Each module is depicted as a box with the main routines and functions summarised.

Geoscientific
Model Development
Discussions

Open Access

EGU

The model may also be compiled as a library, termed libGLM, that can be called as a plugin into other models (e.g., see Section 5.4). Whilst the model is not object-oriented, users may easily customise specific modules described in Section 2 by adding or extending options for alternate schemes or functions.

5 To facilitate the use of the model in teaching environments and for users with limited technical support, iti may be operated without any third party software, as the input files consist of "namelist" (`nml`) text files for configuration and csv files for meteorological and flow time series data (Figure 16). The outputs from predictions are stored into a structured netCDF file, which can be visualised in real-time through the simple inbuilt plotting library (libplot) or may be opened for post-processing in MATLAB, R, or any other tool supporting the open netCDF format (see Section 5.1). Parameters and configuration details

10 are input through the main `glm.nml` text file (Figure 16) and default parameters and their associated descriptions are outlined in Table 1.
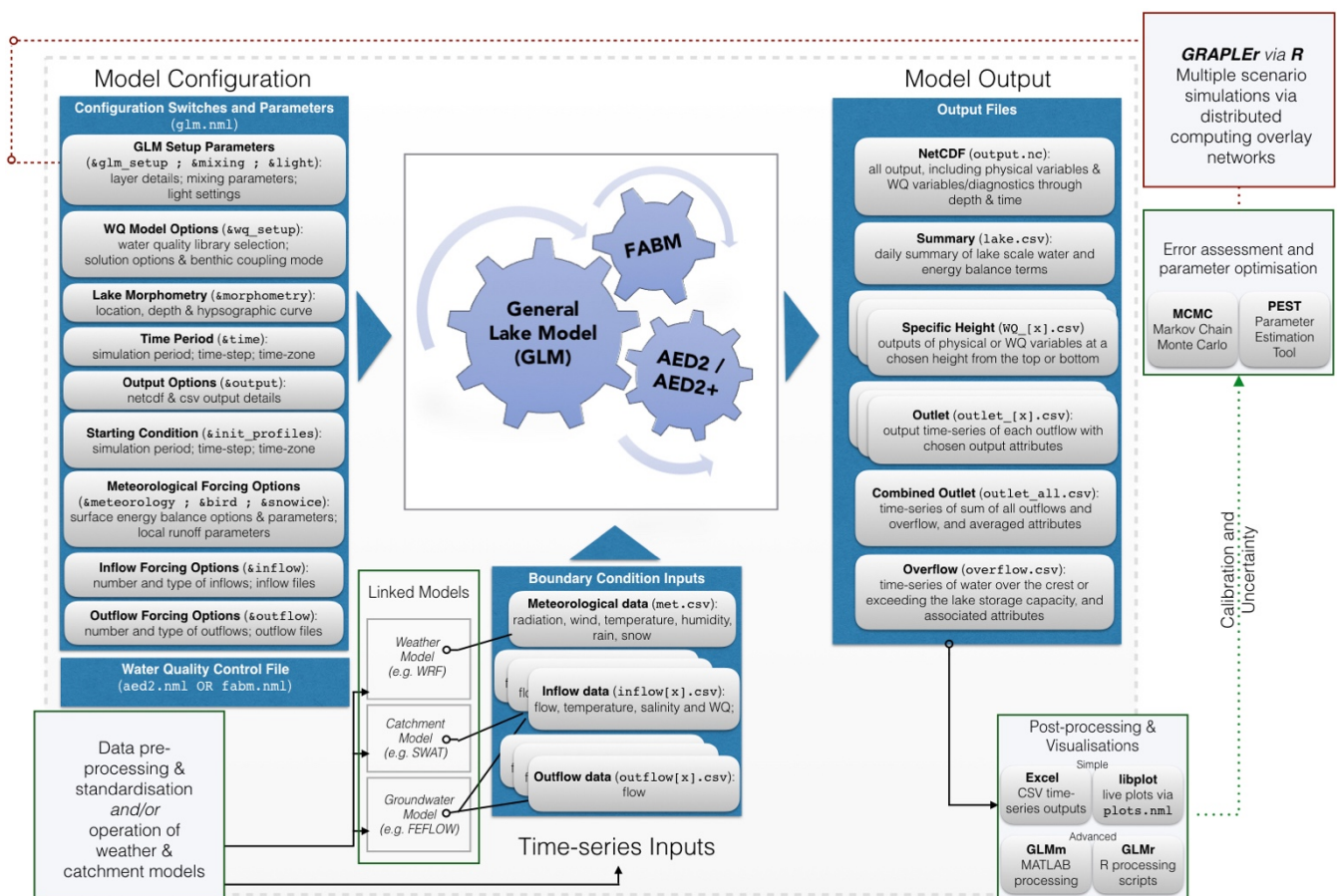
Figure 16: Flow diagram showing the input information required for operation of the model, the outputs, and analysis pathways.

15

Revision 8 Mar 2018

4 Dynamic coupling with biogeochemical and ecological model libraries

Beyond modelling the vertical temperature distribution, the water, ice and heat balance, as well as the transport and mixing in a lake, the model has been designed to couple with biogeochemical and ecological model libraries. Currently the model is distributed pre-linked with the AED2 simulation library (Hipsey et al., 2013) and the Framework for Aquatic Biogeochemical

5 Models (FABM; Bruggeman and Bolding, 2014). Through connection with these libraries, GLM can simulate the seasonal changes in vertical profiles of turbidity, oxygen, nutrients, phytoplankton, zooplankton, pathogens and other water quality variables of interest. Documentation of these models is beyond the scope of the present paper, however, two features are highlighted here as being relevant to managing physical-ecological interactions.

10 Firstly, the model is designed to allow a user defined number of sediment zones that span the depth of the lake. Using this approach, the current setup allows for depth-dependent sediment properties, both for physical properties such as roughness or sediment heat flux (as outlined in previous sections), and also biogeochemical properties such as sediment nutrient fluxes and benthic ecological interactions. Since the GLM layer structure is flexible over time (i.e., layer depths are not fixed), any interactions between the water and sediment/benthos must be managed at each time step. The model therefore supports

15 disaggregation and/or aggregation of layer properties, for mapping individual water layers to one or more sediment zones (Figure 17). The weightings provided by each layer to the sediment are based on the relative depth overlap of a layer with the depth range of the sediment zone. This approach makes the model suitable for long-term assessments of wetland, lake and reservoir biogeochemical budgets, including for C, N and other attribute balances as required (Stepanenko et al., 2016).
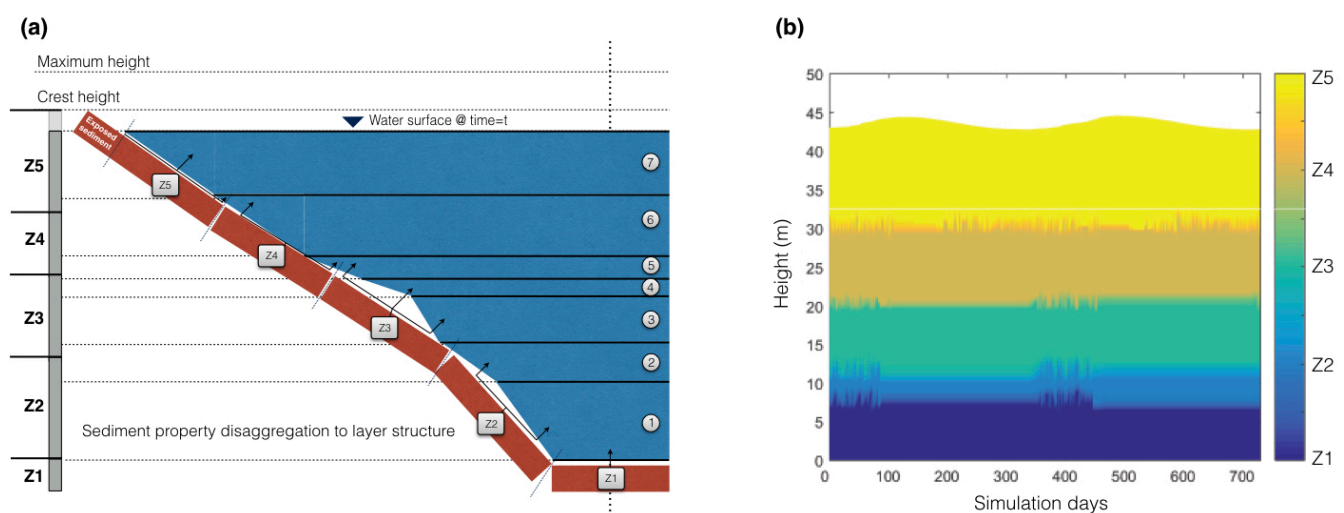
20

Figure 17: a) Schematic of a lake model layer structure (indicated by layers 1-7), in conjunction with five sediment "zones" (Z1-Z5) activated when `benthic_mode` = 2. The dynamically varying layer structure is re-mapped to the fixed sediment zone locations at each time step in order for the sediment zone to receive the average overlying water properties, and for the water to receive the appropriate information from benthic/sediment variables. b) example of GLM output showing the sediment zone each water layer

25 **is mapped to.**

Revision 8 Mar 2018

Secondly, the water quality modules feed back to GLM properties related to the water and/or heat balance. Feedback options include water density additions, bottom friction, f_w, the light attenuation coefficient, K_w, solar shading f_{SR}, and rainfall interception, f_R.

5 Workflow tools for integrating GLM with sensor data and supporting models

5 The GLM model has been designed to support integration of large volumes of data coming from instrumented lakes, including many GLEON sites. These data consist of high-frequency and discrete time series observations of hydrologic fluxes, meteorology, temperature, and water quality (e.g., Hamilton et al. 2014). To facilitate research that requires running the model using these data sources, we have created GLM interfaces in the R and MATLAB analysis environments. These tools support user-friendly access to the model and include routines that streamline the process of calibrating models or running various
10 scenarios. In addition, for assessment of lake dynamics in response to catchment or climatic forcing, it is desirable to be able to connect GLM with other model platforms associated with surface and groundwater simulation, and weather prediction (Read et al., 2016).

5.1 R and MATLAB libraries for model setup and post-processing

The R and MATLAB scientific languages are commonly used in aquatic research, often as part of automated modelling and
15 analysis workflows. GLM has a client library for both, and these tools are shared freely online. The R package is called "`glmtools`" (https://github.com/USGS-R/glmtools) and the MATLAB library is called "`GLMm`" (https://github.com/AquaticEcoDynamics/GLMm). Both tools have utilities for model output pre- and post-processing. The pre-processing components can be used to format and modify data inputs and configuration files, and define options for how GLM executes. Post-processing tools include visualizations of simulation results (as shown in the results figures above),
20 comparisons to field observations, and various evaluations of model performance.

5.2 Utilities for assessing model performance, parameter identification and uncertainty analysis

In order to compare the performance of the model for various types of lakes, numerous metrics of model performance are relevant. These include simple measures like surface or bottom temperature, or ice thickness. It is also possible to assess the model's performance in capturing higher-order metrics relevant to lake dynamics, including Schmidt Stability, thermocline
25 depth, ice on/off dates (see also Bruce et al., 2018, for a detailed assessment of the model's accuracy across a wide diversity of lakes across the globe). With particular interest in the model's ability to interface with high frequency sensor data for calculation of key lake stability metrics (Read et al., 2011), continuous wavelet transform comparisons are also possible (Kara et al., 2012), allowing assessment of the time scales over which the model is able to capture the observed variability within the data.

30

As part of the modelling process, it is common to adjust parameters to get the best fit with available field data and, as such, the use of a Bayesian Hierarchical Framework in the aquatic ecosystem modelling community has become increasingly useful (e.g., Zhang and Arhonditsis, 2009; Romarheim et al., 2015). Many parameters described throughout Section 2 are attempts

at physically based descriptions where there is relatively little variation (Bruce et al., 2018), thereby reducing the number of parameters that remain uncertain. For others, however, their variation reflects imperfect formulation of some processes that are not completely described numerically. Therefore, within MATLAB, support scripts for GLM to work with the Markov Chain Monte Carlo (MCMC) code outlined in Haario et al. (2006) can be used to provide improved parameter estimates and

5   uncertainty assessment (Figure 18). Example setups for use of GLM within the PEST (Parameter Estimation Tool) have also been developed, giving users access to a wide range of assessment methodologies. The PEST framework allows for calibration of complex models using highly-parameterised regularisation with pilot-points (Doherty, 2015). Sensitivity matrices derived from the calibration process can also be utilised in linear and non-linear uncertainty analysis.
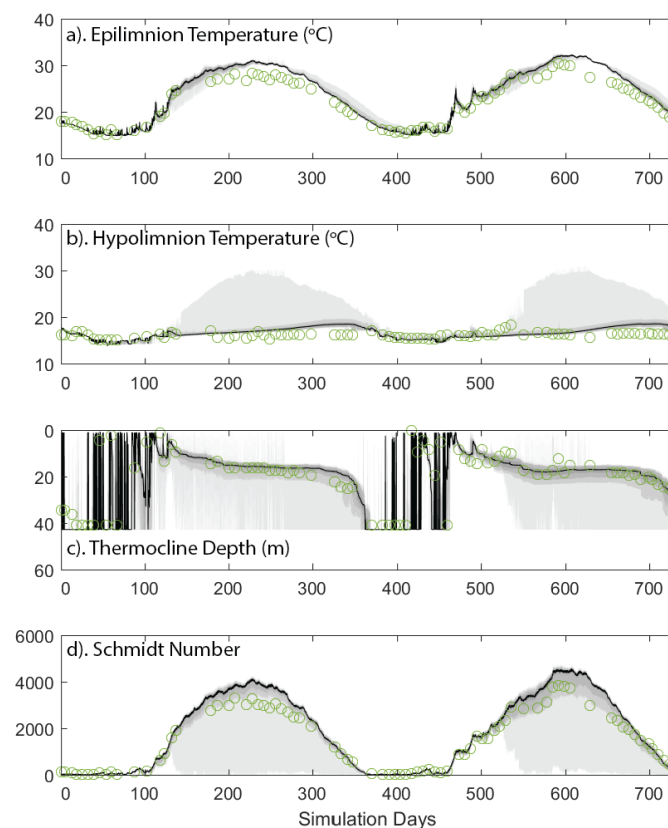
10   **Figure 18: Depiction of parameter uncertainty for a GLM simulation of Lake Kinneret, Israel, following calibration against observations (green circles) via MCMC for a) epilimnion temperature, b) hypolimnion temperature, c) thermocline depth, and d) Schmidt number. The black line indicates the 50th-percentile likelihood of the prediction, and the grey bands depict the 40th, 60th and 80th percentile.**

15   **5.3 Operation in the cloud: GRAPLEr**

Questions relevant to land use and climate change are driving scientists to develop numerous scenarios for how lake ecosystems might respond to changing exogenous drivers. An important approach to addressing these questions is to simulate lake or

Geoscientific
Model Development
Discussions

reservoir physical-biological interactions in response to changing hydrology, nutrient loads or meteorology, and then infer consequences from the emergent properties of the simulation, such as changes in water clarity, extent of anoxia, mixing regime, or habitability to fishes (Hipsey et al., 2015). Often, it takes years or even decades for lakes to respond fully to changes in exogenous drivers, requiring simulations to recreate lake behavior over extended periods. While most desktop computers can

5 run a decade-long, low-resolution simulation in less than one minute, high-resolution simulations of the same extent may require minutes to hours of processor time. When questions demand hundreds, thousands or even millions of simulations, the desktop approach is no longer suitable.

Through access to distributed computing resources, modellers can run thousands of GLM simulations in the time it takes to

10 run a few simulations on a desktop computer. Collaborations between computer scientists in the Pacific Rim Applications and Grid Middleware Assembly (PRAGMA) and GLEON have led to the development of GRAPLEr (GLEON Research and PRAGMA Lake Expedition in R), software, written in R, that enables modellers to distribute batches of GLM simulations to pools of computers (Subratie et al., 2017). Modellers use GRAPLEr in two ways: by submitting a single simulation to the GRAPLEr Web service, along with instructions for running that simulation under different climate scenarios, or by configuring

15 many simulations on the user's desktop computer, and then submitting them as a batch to the Web service. The first approach provides a high degree of automation that is well suited to training and instruction, and the second approach has the full flexibility often needed for research projects. In all approaches, GRAPLEr converts the submitted job to a script that is used by the scheduling program HTCondor (Thain et al., 2005) to distribute and manage jobs among the computer pool and ensure that all simulations run and return results. An iPOP overlay network (Ganguly et al., 2006) allows the compute services to

20 include resources from multiple institutions, as well as cloud computing services.

GRAPLEr's Web service front-end shields the modeller from the compute environment, greatly reducing the need for modellers to understand distributed computing; they therefore only need to install the R package, know the URL of the GRAPLEr Web service, and decide how the simulations should be setup.

25

5.4 Integration with catchment and climate models

GLM simulations may be coupled with catchment models, such as the Soil Water Assessment Tool (SWAT) or similar catchment models, simply by converting the catchment model output into the inflow file format via conversion scripts. Similarly, scripts exist for coupling GLM with the Weather Research Forecasting (WRF) model, or similar climate models,

30 for specification of the meteorological input file from weather prediction simulations.

The above coupling approaches require the models to be run in sequence. For the simulation of lake-wetland-groundwater systems, however, two-way coupling is required to account for the flow of water into and out of the lake throughout the simulation. For these applications, the interaction can be simulated using GLM coupled with the 3D groundwater flow model,

35 FEFLOW (https://www.mikepoweredbydhi.com/products/feflow). For this case, the GLM code is compiled as a Dynamic

Revision 8 Mar 2018

Link Library (DLL) termed libGLM and loaded into FEFLOW as a plug-in module. The coupling between GLM and FEFLOW is implemented using a one-step lag between the respective solutions of the groundwater and lake models. This approach, in most simulations, does not introduce a significant error, however, error can be assessed and reduced using smaller time step lengths. The GLM module was designed to accommodate situations of variable lake geometry, by using a dry-lake/wet-lake approach. In this approach, dry-lake areas are defined as those above the current lake level and wet-lake areas as below the current lake level. Different boundary types in FEFLOW are assigned to dry-lake and wet-lake areas (Figure 19). The calibration of such coupled models is often complex, given the large number of parameters and sensitivities when different sources of information are utilised (for example flow and water level measurements). The FEFLOW-GLM coupling structure allows for a relatively straightforward integration with PEST (Doherty, 2015), based on existing FEFLOW workflows.
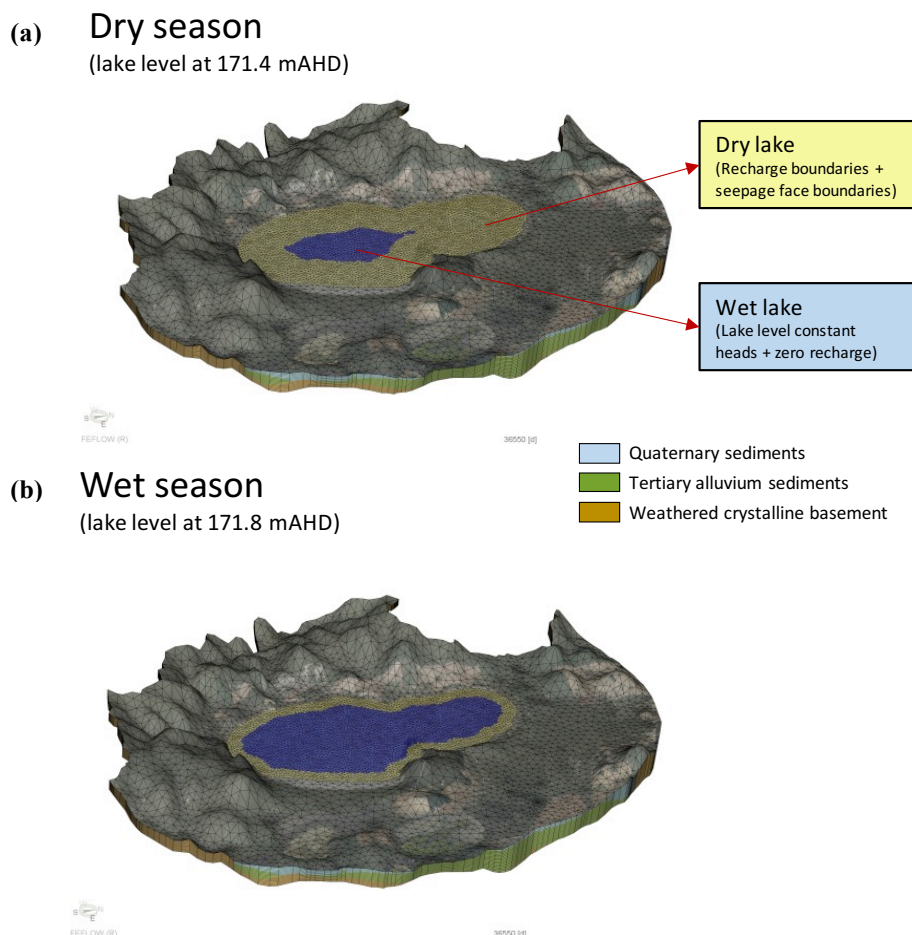
Figure 19: Example of lake boundary changes during wet and dry cycles from Lake Muir, Australia. GLM water level is communicated to FEFLOW to each time step and used as a constant head boundary condition for all wet cells.

6 GLM as a tool for teaching environmental science and ecology

Environmental modelling is integral for understanding complex ecosystem responses to anthropogenic and natural drivers, and also provides a valuable tool for engaging students learning environmental science (Carey and Gougis, 2017). Previous pedagogical studies have demonstrated that engaging students in modelling provides cognitive benefits, enabling them to build

new scientific knowledge and conceptual understanding (Stewart et al., 2005; Zohar and Dori 2011). For example, modelling forces students to analyze patterns in data, create evidence-based hypotheses for those patterns and make their hypotheses explicit, and develop predictions of future conditions (Stewart et al., 2005). As a result, the U.S. National Research Council has recently integrated modelling into the *Next Generation Science Standards*, which provide recommendations for primary

5   and secondary school science pedagogy in the United States (NRC, 2013). However, it remains rare for undergraduate and graduate science courses to include the computer-based modelling that environmental scientists need to manage natural ecosystems.

A teaching module for the use of GLM within undergraduate and graduate classrooms has been developed to explore lake

10   responses to climate change (Carey and Gougis, 2017). The GLM module, called the "Climate Change Effects on Lake Temperatures", teaches students how to set up a simulation for a model lake within R. After they are able to successfully run their lake simulations, they force the simulation with climate scenarios of their own design to examine how lakes may change in the future. To improve computational efficiency, students also learn how to submit, retrieve, and analyze hundreds of model simulations through distributed computing overlay networks embedded via the GRAPLEr interface (Section 5.3). Hence,

15   students participating in the module learn computing and quantitative skills in addition to improving their understanding of how climate change affects lake ecosystems.

Initial experiences teaching GLM as well as pre- and post-assessments indicate that participation in the module improves students' understanding of lake responses to climate change (Carey and Gougis, 2017). By modifying GLM boundary

20   condition data and exploring model output, students are able to better understand the processes that control lake responses to altered climate, and improve their predictions of future lake change. Moreover, the module exposes students to computing and modelling tools not commonly experienced in most university classrooms, building competence with manipulating data files, scripting, creating figures and other visualizations, and statistical and time series analysis; all skills that are transferrable for many other applications.

25

7 Conclusions

As part of GLEON activities, the emergence of complex questions about how different lake types across the world are responding to climate change and land-use change has created the need for a robust, accessible community code suitable for a diverse range of lake types and simulation contexts. Here, GLM is presented as a tool that meets many of the needs of network

30   participants for their individual lake simulation requirements, in addition to being suitable for application in a distributed way across tens to thousands of lakes for regional and global scale assessments. Recent examples include an application of the model for assessing how the diversity of >2000 lakes in the lake-rich landscape in Wisconsin respond to climate including projected warming (Read et al., 2014; Winslow et al., 2017). Given its computationally efficient nature, it is envisioned that GLM can be made available as a library for use within in land-surface models (e.g., the Community Land Model, CLM),

35   allowing improved representation of lake dynamics in regional hydrological or climate assessments. With further advances in

Geoscientific
Model Development
Discussions

Revision 8 Mar 2018

the degree of resolution and scope of earth system models, we further envisage GLM as an option suitable to be embedded within these models to better allow the simulation of lake stratification, air-water interaction of momentum and heat, and also biogeochemically relevant variables associated with contemporary questions about greenhouse gases emissions such as CO_2, CH_4, and N_2O.

5

Since the model is one-dimensional, it assumes no horizontal variability in the simulated water layers and users must therefore ensure their application of the model is suited to this simplifying assumption. For stratified systems, the parameterization of mixing due to internal wave and inflow intrusion dynamics is relatively simple, making the model ideally suited to longer-term investigations ranging from weeks to decades (depending on the domain size), and for coupling with biogeochemical

10 models to explore the role that stratification and vertical mixing play on lake ecosystem dynamics. However, the model can also be used for shallow lakes, ponds and wetland environments where the water column is relatively well mixed. In cases where the assumption of one-dimensionality is not met for a particular lake application, a two or three dimensional model may be preferred.

15 This paper has focused on description of the hydrodynamic model, but we highlight that the model is a platform for coupling with advanced biogeochemical and ecological simulation libraries for water quality prediction and integrated ecosystem assessments. As with most coupled hydrodynamic-ecological modelling platforms, GLM handles the boundary conditions and transport of variables simulated within these libraries, including the effects of inflows, vertical mixing, and evapo-concentration. Whilst the interface to these libraries is straightforward, the Lagrangian approach adopted within GLM for

20 simulation of the water column necessitates the adoption of sediment zones on a static grid that is independent from the water column numerical grid.

More advanced workflows for operation of the model within distributed computing environments and with data assimilation algorithms is an important application when used within GLEON capabilities related to high frequency data and its

25 interpretation. The 1D nature of the model makes the run-times modest and therefore the model suitable for application within more intensive parameter identification and uncertainty assessment procedures. This is particularly relevant as the needs for network participants to expand model configurations to further include biogeochemical and ecological state variables. It is envisioned that continued application of the model will allow us to improve parameter estimates and ranges, and this will ultimately support other users of the model in identifying parameter values, and assigning parameter prior distributions. Since

30 many of the users the model is intended for may not have access to the necessary cyberinfrastructure, the use of GLM with the open-source GRAPLEr software in the R environment provides access to otherwise unavailable distributed computing resources. This has the potential to allow non-expert modellers within the science community to apply good modelling practices by automating boundary condition and parameter sensitivity assessments, with technical aspects of simulation management abstracted from the user.

35

Geoscientific
Model Development
Discussions

Open Access

EGU

Revision 8 Mar 2018

Finally, the role of models in informing and educating members of the network and the next generation of hydrologic and ecosystem modellers has been identified as a critical element of synthesis activities and supporting cross-disciplinary collaboration (Weathers et al., 2017). Initial use of GLM within the classroom has found that teaching modules integrating GLM into classes improves students' understanding of lake ecosystems.

5 **Code availability**

The GLM code is provided as open-source under the GNU GPL3 license, and version controlled via the GitHub repository: https://github.com/AquaticEcoDynamics/GLM. *[Code DOI to be inserted here on final acceptance]*

Data availability

The five example lakes used to demonstrate the model operation are described along with model input files (and associated
10   hydrologic and meteorological forcing data) within the GitHub repository:
https://github.com/AquaticEcoDynamics/GLM/tree/master/Examples/2.4.0
[Examples DOI to be inserted here on final acceptance]

References

Ashton, G.D. (ed.), 1986. <u>River and lake ice engineering</u>. Water Resources Publications, Littleton, Colorado, U.S.A.

Antenucci, J.P., Brookes, J.D. and Hipsey, M.R., 2005. A simple model for quantifying" Cryptosporidium" transport, dilution, and potential risk in reservoirs. *Journal of the American Water Works Association*, 97(1): 86-93.

5   Babanin, A.V. and Makin, V.K., 2008. Effects of wind trend and gustiness on the sea drag: Lake George study. *Journal of Geophysical Research: Oceans,* 113(C2).

Bird, R.E., 1984. A simple, solar spectral model for direct-normal and diffuse horizontal irradiance. *Solar Energy*, 32: 461-471.

Briegleb, B.P., Minnis, P., Ramanathan, V. and Harrison, E., 1986. Comparison of regional clear-sky albedos inferred from
10   satellite observations and model computations. *Journal of Climate and Applied Meteorology*, 25(2): 214-226.

Bruce, L.C., Frassl, M.A., Arhonditsis, G.B., Gal, G., Hamilton, D.P., Hanson, P.C., et al., 2018. A multi-lake comparative analysis of the General Lake Model (GLM): Stress-testing across a global observatory network. *Environmental Modelling and Software*, 102: 274-291.

Bruggeman, J. and Bolding, K., 2014. A general framework for aquatic biogeochemical models. *Environmental Modelling*
15   *and Software*, 61: 249-265.

Brutsaert, W., 1975. On a derivable formula for long-wave radiation from clear skies, *Water Resources Research*, 11(5): 742–744.

Bueche, T., Hamilton, D.P. and Vetter, M., 2017. Using the General Lake Model (GLM) to simulate water temperatures and ice cover of a medium-sized lake: a case study of Lake Ammersee, Germany. *Environmental Earth Sciences*, *76*(13): 461.

20   Businger, J.A., Wyngaard, J.C., Izumi, Y. and Bradley, E.F., 1971. Flux profile relationships in the atmospheric surface layer. *Journal of Atmospheric Sciences*, 28: 181-189.

Carey, C.C. and Gougis, R.D., 2017. Simulation modeling of lakes in undergraduate and graduate classrooms increases comprehension of climate change concepts and experience with computational tools. *Journal of Science Education and Technology*, 26: 1-11.

25   Cengel, Y.A. and Ozisk, M.N., 1984. Solar radiation absorption in solar ponds. *Solar Energy,* 33(6): 581-591.

Chung, E. G., Schladow, S. G., Perez-Losada, J., and Robertson, D. M., 2008. A linked hydrodynamic and water quality model for the Salton Sea. *Hydrobiologia,* 604:57–75.

Chung, S.W., Imberger, J., Hipsey, M.R. and Lee, H.S., 2014. The influence of physical and physiological processes on the spatial heterogeneity of a Microcystis bloom in a stratified reservoir. *Ecological Modelling*, *289*, pp.133-149.

Revision 8 Mar 2018

Cole, J.J., Prairie, Y.T., Caraco, N.F., McDowell, W.H., Tranvik, L.J., Striegl, R.G., Duarte, C.M., Kortelainen, P., Downing, J.A., Middelburg, J.J. and Melack, J., 2007. Plumbing the Global Carbon Cycle: Integrating Inland Waters into the Terrestrial Carbon Budget. *Ecosystems*, 10: 172–185.

Doherty, J., 2015. Calibration and Uncertainty Analysis for Complex Environmental Models. Watermark Numerical
5   Computing, Brisbane, Australia. ISBN: 978-0-9943786-0-6

Dyer, A.J., 1974. A review of flux-profile relationships. *Boundary Layer Meteorology*, 7: 363-372.

Fischer, H.B., List, E.G., Koh, R.C.Y., Imberger, J. and Brooks, N.H., 1979. Mixing in Inland and Coastal Waters. Academic Press. New York, NY, 483 pp.

Flerchinger, G.N., Xaio, W., Marks, D., Sauer, T.J. and Yu, Q., 2009. Comparison of algorithms for incoming atmospheric
10   long-wave radiation, *Water Resources Research*, 45: W03423.

Francey, R.J. and Garratt, J.R., 1978. Eddy flux measurements over the ocean and related transfer coefficients. *BoundaryLayer Meteorology*, 14: 153-166.

Gal, G., Imberger, J., Zohary, T., Antenucci, J., Anis, A. and Rosenberg, T., 2003. Simulating the thermal dynamics of Lake Kinneret. *Ecological Modelling*, 162: 69-86.

15   Gal, G., Hipsey, M.R., Parparov, A., Wagner, U., Makler, V. and Zohary, T., 2009. Implementation of ecological modeling as an effective management and investigation tool: Lake Kinneret as a case study. *Ecological Modelling*, 220(13): 1697-1718.

Ganguly, A., Agrawal, A., Boykin, P. O. and Figueiredo, R., 2006. IP over P2P: Enabling self-configuring virtual IP networks for grid computing. In International Parallel and Distributed Processing Symposium.

Gill, A.E., 1982. Atmosphere-ocean dynamics (Vol. 30). Academic Press.

20   Gu, R. and Stefan, H.G., 1993. Validation of cold climate lake temperature simulation. *Cold Regions Science and Technology*, 22: 99-104.

Haario, H., Laine, M., Mira, A. and Saksman, E., 2006. DRAM: Efficient adaptive MCMC, *Statistics and Computing,* 16: 339-354.

Hamilton, D.P. and Schladow, S.G. 1997. Water quality in lakes and reservoirs. Part I Model description. *Ecological*
25   *Modelling*, 96: 91–110.

Hamilton, D.P., Carey, C.C., Arvola, L., Arzberger, P., Brewer, C., Cole, J.J., Gaiser, E., Hanson, P.C., Ibelings, B.W., Jennings, E. and Kratz, T.K., 2015. A Global Lake Ecological Observatory Network (GLEON) for synthesising high-frequency sensor data for validation of deterministic ecological models. *Inland Waters*, 5(1): 49-56.

Hanson, P.C., Weathers, K.C. and Kratz, T.K., 2016. Networked lake science: how the Global Lake Ecological Observatory
30   Network (GLEON) works to understand, predict, and communicate lake ecosystem response to global change. *Inland Waters*, 6(4): 543-554.

Harvey, L.D.D., 1990. Testing alternative parameterizations of lateral melting and upward basal heat flux in a thermodynamic sea ice model. *Journal of Geophysical Research,* 95: 7359-7365.

Henderson-Sellers, B., 1986. Calculating the surface energy balance for lake and reservoir modeling: A review. *Reviews of Geophysics*, 24(3): 625-649.

Hicks, B.B., 1975. A procedure for the formulation of bulk transfer coefficients over water. *Boundary Layer Meteorology*, 8: 515-524.

Hicks, B.B., 1972. Some evaluations of drag and bulk transfer coefficients over water. *Boundary Layer Meteorology*, 3: 201:213.

Hipsey, M.R. and Sivapalan, M., 2003. Parameterizing the effect of a wind-shelter on evaporation from small waterbodies. *Water Resources Research*, 39(12): 1339.

Hipsey, M.R., Bruce, L.C. and Hamilton, D.P., 2013. Aquatic EcoDynamics (AED) Model Library Science Manual. The University of Western Australia Technical Manual, Perth, Australia, 34pp.

Hipsey, M.R., Hamilton, D.P., Hanson, P.C., Carey, C.C., Coletti, J.Z., Read, J.S., Ibelings, B.W., Valesini, F.J. and Brookes, J.D., 2015. Predicting the resilience and recovery of aquatic systems: A framework for model evolution within environmental observatories. *Water Resources Research*, 51(9): 7023-7043.

Hocking, G.C. and Patterson, J.C., 1991. Quasi-two-dimensional reservoir simulation model. *Journal of Environmental Engineering*, 117: 595-613.

Hu, F., Bolding, K., Bruggeman, J., Jeppesen, E., Flindt, M., van Gerven, L.P.A., Janse, J.H., Janssen, A.B.G., Kuiper, J.J., Mooij, W.M. and Trolle, D. 2016. FABM-PCLake - Linking aquatic ecology with hydrodynamics. *Geoscientific Model Development*, 9: 2271-2278

Idso, S.B. and Jackson, R.D., 1969. Thermal radiation from the atmosphere. *Journal of Geophysical Research*, 74: 5397-5403.

Imberger, J., Patterson, J., Hebbert, B. and Loh, I., 1978. Dynamics of reservoir of medium size. *Journal of the Hydraulics Division - ASCE*, 104 No HY5: 725-743.

Imberger, J. and Patterson, J.C., 1981. *A dynamic reservoir simulation model-DYRESM:5*. In: H.B. Fischer (ed.), Transport Models for Inland and Coastal Waters. Academic Press, New York*:* 310-361.

Imberger, J. and Patterson, J.C., 1990. *Physical Limnology*. In: T. Wu (ed.), Advances in applied mechanics 27. Academic Press. Boston. U.S.A.

Imboden, D.M. and Wüest, A., 1995. *Mixing Mechanisms in Lakes*, p. 83-138. In: A. Lerman, D.M. Imboden and J.R. Gat (eds.), Physics and Chemistry of Lakes. Springer-Verlag.

Janssen, A.B.G., Arhonditsis, G.B., Beusen, A., Bolding, K., Bruce, L., Bruggeman, J., Couture, R.M., Downing, A.S., Elliott, J.A., Frassl, M.A., Gal, G., Gerla, D.J., Hipsey, M.R., Hu, F., Ives, S.C., Janse, J., Jeppesen, E., Jöhnk, K.D., Kneis, D., Kong, X., Kuiper, J.K., Lehmann, M., Lemmen, C., Ozkundakci, D., Petzoldt, T., Rinke, K., Robson, B.J., Sachse, R., Schep,

Revision 8 Mar 2018

S., Schmid, M., Scholten, H., Teurlincx, S., Trolle, D., Troost, T.A., Van Dam, A., Van Gerven, L.A., Weijerman, M., Wells S.A. and Mooij, W.M., 2015. Exploring, exploiting and evolving diversity of aquatic ecosystem models: a community perspective. *Aquatic Ecology*, 49(4): 513-548.

Jellison, R. and Melack, J.M., 1993. Meromixis and vertical diffusivities in hypersaline Mono Lake, California. *Limnology and Oceanography*, 38: 1008–1019.

Ji, Z.G., 2008. Hydrodynamics and water quality: modeling rivers, lakes, and estuaries. John Wiley & Sons.

Kara, E.L., Hanson, P., Hamilton, D., Hipsey, M.R., McMahon, K.D., Read, J.S., Winslow, L., Dedrick, J., Rose, K., Carey, C.C. and Bertilsson, S., 2012. Time-scale dependence in numerical simulations: assessment of physical, chemical, and biological predictions in a stratified lake at temporal scales of hours to months. *Environmental Modelling and Software*, *35*: 104-121.

Kim, J-W., 1976. A generalized bulk model of the oceanic mixed layer. *Journal of Physical Oceanography*, 6: 686-695.

Kirk, J.T.O., 1994. Light and photosynthesis in aquatic ecosystems. Cambridge University Press.

Kirillin, G., Hochschild, J., Mironov, D., Terzhevik, A., Golosov, S. and Nützmann, G., 2011. FLake-Global: Online lake model with worldwide coverage. *Environmental Modelling and Software*, 26(5): 683-684.

Kleinhans, M.G. and Grasmeijer, B.T., 2006. Bed load transport on the shoreface by currents and waves. *Coastal Engineering*, 53: 983-996.

Klug, J.L., Richardson, D.C., Ewing, H.A., Hargreaves, B.R., Samal, N.R., Vachon, D., Pierson, D.C., Lindsey, A.M., O'Donnell, D.M., Effler, S.W. and Weathers, K.C., 2012. Ecosystem Effects of a Tropical Cyclone on a Network of Lakes in Northeastern North America. *Environmental Science and Technology*, 46 (21): 11693-11701.

Kraus, E.B. and Turner, J.S., 1967. A one-dimensional model of the seasonal thermocline: II The general theory and its consequences. *Tellus*, 19: 98-106.

Laenen A. and LeTourneau A.P., 1996. Upper Klamath Lake nutrient loading study – Estimate of wind-induced resuspension of bed sediment during periods of low lake elevation. *US Geological Survey Open-File Report, 95-414*, 11 pp

Launiainen, J., 1995. Derivation of the relationship between the Obukhov stability parameter and the bulk Richardson number for flux-profile studies. *Boundary Layer Meteorology*, 76: 165-179.

Launiainen, J. and Cheng, B., 1998. Modelling of ice thermodynamics in natural water bodies. *Cold Region Science and Technology*, 27: 153-178.

Launiainen, J. and Vihma, T., 1990. Derivation of turbulent surface fluxes—An iterative flux-profile method allowing arbitrary observing heights. *Environmental Software*, 5: 113-124.

Luo, L., Hamilton, D.P. and Han, B., 2010. Estimation of total cloud cover from solar radiation observations at Lake Rotorua, New Zealand. *Solar Energy*, 84: 501-506.

Revision 8 Mar 2018

Magee, M.R., Wu, C.H., Robertson, D.M., Lathrop, R.C. and Hamilton, D.P., 2016. Trends and abrupt changes in 104 years of ice cover and water temperature in a dimictic lake in response to air temperature, wind speed, and water clarity drivers. *Hydrology and Earth System Sciences*, 20(5): 1681.

Makler-Pick, V., Gal, G., Shapiro, J. and Hipsey, M.R., 2011. Exploring the role of fish in a lake ecosystem (Lake Kinneret, Israel) by coupling an individual-based fish population model to a dynamic ecosystem model. *Canadian Journal of Fisheries and Aquatic Sciences*, *68*(7): 1265-1284.

Markfort, C.D., Perez, A.L.S., Thill, J. W., Jaster, D.A., Porté-Agel, F. and Stefan, H.G. 2010. Wind sheltering of a lake by a tree canopy or bluff topography. *Water Resources Research*, 46: 1–13.

Martynov, A., Sushama, L., Laprise, R., Winger, K. and Dugas, B., 2012. Interactive lakes in the Canadian Regional Climate Model, version 5: The role of lakes in the regional climate of North America. *Tellus, Series A Dynamic Meteorology And Oceanography*, 64: 1-22.

Matzinger, A., Schmid, M., Veljanoska-Sarafiloska, E., Patceva, S., Guseska, D., Wagner, B., Müller, B., Sturm, M. and Wüest, A., 2007. Eutrophication of ancient Lake Ohrid: global warming amplifies detrimental effects of increased nutrient inputs, *Limnology and Oceanography*, 52(1): 338-353.

McKay, G.A., 1968. Problems of measuring and evaluating snow cover. In: *Proceedings Workshop Seminar of Snow Hydrology.(Secretariat Canadian National Committee for the IHD*, Ottawa: p.49-62.

McCord, S.A. and Schladow, S.G., 1998. Numerical simulations of degassing scenarios for CO2-rich Lake Nyos, Cameroon. *Journal of Geophysical Research: Solid Earth*, 103(B6): 12355-12364.

Menció, A., Casamitjana, X., Mas-Pla, J., Coll, N., Compte, J., Martinoy, M., Pascual, J. and Quintana, X.D., 2017. Groundwater dependence of coastal lagoons: The case of La Pletera salt marshes (NE Catalonia). *Journal of Hydrology*, 552: 793-806.

Mueller H, Hamilton DP and Doole GJ. 2016. Evaluating services and damage costs of degradation of a major lake ecosystem. *Ecosystem Services,* 22: 370-380.

Mooij, W.M., Trolle, D., Jeppesen, E., Arhonditsis, G., Belolipetsky, P.V., Chitamwebwa, D.B.R., Degermendzhy, A.G., DeAngelis, D.L., De Senerpont Domis, L.N., Downing, A.S., Elliott, A.E., Fragoso Jr, C.R., Gaedke, U., Genova, S.N., Gulati, R.D., Håkanson, L., Hamilton, D.P., Hipsey, M.R., Hoen, J., Hülsmann, S., Los, F.J., Makler-Pick, V., Petzoldt, T., Prokopkin, I.G., Rinke, K., Schep, S.A., Tominaga, K., Van Dam, A.A., Van Nes, E.H., Wells, S.A. and Janse, J.H., 2010. Challenges and opportunities for integrating lake ecosystem modelling approaches. *Aquatic Ecology*, 44: 633–667.

Monin, A.S. and Obukhov, A.M., 1954. Basic laws of turbulent mixing in the atmosphere near the ground. *Jr. Akad. Nauk SSSR Geofiz. Inst.,* 24: 163-187.

National Research Council (NRC), 2013. Next generation science standards: For states, by states. Washington, DC: The National Academies Press.

O'Reilly, C. M., Sharma, S., Gray, D. K., Hampton, S. E., Read, J. S., Rowley, R. J., Schneider, P., Lenters, J. D., McIntyre, P. B., Kraemer, B. M., et al., 2015. Rapid and highly variable warming of lake surface waters around the globe. *Geophysical Research Letters*, 42(24): 10773–10781.

Patterson, J.C., Hamblin, P.F. and Imberger, J., 1984. Classification and dynamics simulation of the vertical density structure of lakes. *Limnology and Oceanography*, 29: 845-861.

Patterson, J.C. and Hamblin, P.F., 1988. Thermal simulation of a lake with winter ice cover. *Limnology and Oceanography*, 33: 323-338.

Paulson, C. A., 1970. The mathematical representation of wind speed and temperature profiles in the unstable atmospheric surface layer. *Journal of Applied Meteorology*, 9: 857-861.

Peeters, F., Straile, D. Loke, A. and Livingstone, D. M., 2007. Earlier onset of the spring phytoplankton bloom in lakes of the temperate zone in a warmer climate. *Global Change Biology*. 13: 1898–1909.

Perroud, M., Goyette, S., Martynov, A., Beniston, M. and Anneville, O., 2009. Simulation of multiannual thermal profiles in deep Lake Geneva: A comparison of one-dimensional lake models. *Limnology and Oceanography*, *54*(5): 1574-1594.

Porter, J.H., Hanson, P.C. and Lin, C.C., 2012. Staying afloat in the sensor data deluge. *Trends in Ecology and Evolution*, 27(2): 121-129.

Read, J.S., Hamilton, D.P., Jones, I.D., Muraoka, K., Winslow, L.A., Kroiss, R., Wu, C.H. and Gaiser, E., 2011. Derivation of lake mixing and stratification indices from high-resolution lake buoy data. *Environmental Modelling and Software,* 26: 1325–1336.

Read, J.S., Hansen, G., Van Den Hoek, J., Hanson, P.C., Bruce, L.C. and Markfort, C.D., 2014. Simulating 2368 temperate lakes reveals weak coherence in stratification phenology. *Ecological Modelling*, 291: 142-150.

Read, J.S., Gries, C., Read, E.K., Klug, J., Hanson, P.C., Hipsey, M.R., Jennings, E., O'Reilly, C., Winslow, L., Pierson, D., McBride, C. and Hamilton, D.P., 2016. Generating community-built tools for data sharing and analysis in environmental networks. *Inland Waters*, 6(4): 637-644.

Rigosi, A., Hanson, P.C., Hamilton, D.P., Hipsey, M., Rusak, J. A., Bois, J., Sparber, K., Chorus, I., Watkinson, A.J., Qin, B., Kim, B. and Brookes, J.D., 2015. Determining the probability of cyanobacterial blooms: the application of Bayesian networks in multiple lake systems. *Ecological Applications*, 25: 186–199.

Rogers, C.K., Lawrence, G.A. and Hamblin, P.F., 1995. Observations and numerical simulation of a shallow ice-covered mid-latitude lake. *Limnology and Oceanography,* 40: 374-385.

Romarheim, A.T., Tominaga, K., Riise, G. and Andersen, T., 2015. The importance of year-to-year variation in meteorological and runoff forcing for water quality of a temperate, dimictic lake. *Hydrology and Earth System Sciences*, 19(6): 2649-2662.

Revision 8 Mar 2018

Salmon, S.U., Hipsey, M.R., Wake, G.W., Ivey, G.N. and Oldham, C.E., 2017. Quantifying Lake Water Quality Evolution: Coupled Geochemistry, Hydrodynamics, and Aquatic Ecology in an Acidic Pit Lake. *Environmental Science and Technology*, 51(17): 9864-9875.

Saloranta, T.M. and Andersen, T., 2007. MyLake—A multi-year lake simulation model code suitable for uncertainty and
5   sensitivity analysis simulations. *Ecological Modelling*, 207(1): 45-60.

Schwarz, C.V. and White, B.Y., 2005. Metamodeling knowledge: Developing students' understanding of scientific modeling. *Cognition and Instruction*, 23(2): 165-205.

Schwarz, C.V., Reiser, B.J., Davis, E.A., Kenyon, L., Achér, A., Fortus, D., Shwartz, Y., Hug, B. and Krajcik, J., 2009. Developing a learning progression for scientific modeling: Making scientific modeling accessible and meaningful for
10   learners. *Journal of Research in Science Teaching*, 46(6): 632-654.

Sherman, F.S., Imberger, J. and Corcos, G.M., 1978. Turbulence and mixing in stably stratified waters. *Annual Review of Fluid Mechanics,* 10: 267-288.

Snortheim, C.A., P.C. Hanson, K.D. McMahon, J.S. Read, C.C. Carey, and H.A. Dugan. Meteorological drivers of hypolimnetic anoxia in a eutrophic, north temperate lake. *Ecological Modelling*. 343: 39-53.

15   Spigel, B., 1978. Wind mixing in lakes. PhD thesis, University of California, Berkeley.

Spigel, R.H., Imberger, J. and Rayner, K.N., 1986. Modeling the diurnal mixed layer. *Limnology and Oceanography*, 31: 533-556.

Stepanenko, V., Mammarella, I., Ojala, A., Miettinen, H., Lykosov, V. and Vesala, T., 2016. LAKE 2.0: a model for temperature, methane, carbon dioxide and oxygen dynamics in lakes. *Geoscientific Model Development*, *9*(5): 1977-2006.

20   Stepanenko, V.M., Martynov, A., Jöhnk, K.D., Subin, Z.M., Perroud, M., Fang, X., Beyrich, F., Mironov, D. and Goyette, S., 2013. A one-dimensional model intercomparison study of thermal regime of a shallow, turbid midlatitude lake. *Geoscientific Model Development*, *6*(4): 1337-1352.

Stewart, J., Cartier, J.L. and Passmore, C.M., 2005. Developing understanding through model-based inquiry. In M.S. Donovan & J.D. Bransford (Eds.), How students learn. Washington, DC: National Research Council. pp. 515–565.

25   Strub, P.T. and Powell, T.M., 1987. Surface temperature and transport in Lake Tahoe: inferences from satellite (AVHRR) imagery. *Continental Shelf Research,* 7: 1001-1013.

Subratie, K., Aditya, S., Figueiredo, R., Carey, C.C. and Hanson, P.C., 2017. GRAPLEr: A distributed collaborative environment for lake ecosystem modeling that integrates overlay networks, high-throughput computing, and web services. *Concurrency and Computation: Practice and Experience*, 29(13): e4139.

30   Swinbank, W.C., 1963. Longwave radiation from clear skies. *Quarterly Journal of the Royal Meteorological Society*, 89: 339-348.

Geoscientific
Model Development
Discussions

Open Access

EGU

Revision 8 Mar 2018

Tennessee Valley Authority (TVA), 1972. Heat and mass transfer between a water surface and the atmosphere. Water Resources Research Laboratory Report 14, Report No. 0-6803.

Tabata, S., 1973. A simple but accurate formula for the saturation vapour pressure over liquid water. *Journal of Applied Meteorology*, 12: 1410-1411.

5 Thain, D., Tannenbaum, T. and Livny, M. (2005). Distributed Computing in Practice: the Condor Experience. *Concurrency and Computation: Practice and Experience*, 17 (2–4): 323–356.

Ticehurst J.L., Newham, L.T.H., Rissik, D., Letcher, R.A. and Jakeman, A.J., 2007. A Bayesian network approach for assessing the sustainability of coastal lakes in New South Wales, Australia. *Environmental Modelling and Software,* 22(8):1129-1139.

10 Tranvik, L.J., Downing, J.A., Cotner, J.B., Loiselle, S.A., Striegl, R.G., Ballatore, T.J., Dillon, P., Finlay, K., Fortino, K., Knoll, L.B. and Kortelainen, P.L., 2009. Lakes and reservoirs as regulators of carbon cycling and climate. *Limnology and Oceanography*, 54: 2298-2314.

Trolle, D., Hamilton, D.P., Hipsey, M.R., Bolding, K., Bruggeman, J., Mooij, W. M., Janse, J. H., Nielsen, A., Jeppesen, E., Elliott, J.E., Makler-Pick, V., Petzoldt, T., Rinke, K., Flindt, M. R., Arhonditsis, G.B., Gal, G., Bjerring, R., Tominaga, K.,
15 Hoen, J., Downing, A.S., Marques, D. M., Fragoso Jr, C.R., Søndergaard, M. and Hanson, P.C., 2012. A community-based framework for aquatic ecosystem models. *Hydrobiologia*, 683: 25-34.

Vavrus, S.J., Wynne, R.H. and Foley, J.A., 1996. Measuring the sensitivity of southern Wisconsin lake ice to climate variations and lake depth using a numerical model. *Limnology and Oceanography*, 41: 822-831.

Vickers, D., Mahrt, L. and Andreas, E.L., 2013. Estimates of the 10-m neutral sea surface drag coefficient from aircraft eddy-
20 covariance measurements. *Journal of Physical Oceanography*, 43: 301-310.

Weathers, K.C., Groffman, P.M., Van Dolah, E., Bernhardt, E.S., Grimm, N.B., McMahon, K.D., Schimel, J., Paolisso, M., Maranger, R.J., Baer, S., Brauman, K.A. and Hinckley, E., 2016. Frontiers in Ecosystem Ecology from a Community Perspective: The Future is Boundless and Bright. *Ecosystems*, 19(5): 753-770.

Weber, M., Rinke, K., Hipsey, M.R. and Boehrer, B., 2017. Optimizing withdrawal from drinking water reservoirs to reduce
25 downstream temperature pollution and reservoir hypoxia. *Journal of Environmental Management*, 197: 96-105.

Weinstock, J., 1981. Vertical turbulence diffusivity for weak or strong stable stratification. *Journal of Geophysical Research*, 86(C10): 9925-9928.

Williamson, C.E., Saros, J.E., Vincent, W.F. and Smol, J.P., 2009. Lakes and reservoirs as sentinels, integrators, and regulators of climate change. *Limnology and Oceanography*, 54, 2273-2282.

30 Woolway, R.I., Verburg, P., Merchant, C.J., Lenters, J.D., Hamilton, D.P., Brookes, J., Kelly, S., Hook, S., Laas, A., Pierson, D. and Rimmer, A., 2017. Latitude and lake size are important predictors of over-lake atmospheric stability. *Geophysical Research Letters*, 44 (17), 8875–8883.

Revision 8 Mar 2018

Winslow, L. A., Hansen, G. J. A., Read, J. S. and Notaro, M., 2017 Data Descriptor: Large-scale modeled contemporary and future water temperature estimates for 10774 Midwestern U.S. Lakes. *Scientific Data*, 4:170053.

Wu J., 1973. Wind induced entrainment across a stable density interface. *Journal of Fluid Mechanics*, 61: 275-278.

Xenopoulos, M.A. and Schindler, D.W., 2001. The environmental control of near-surface thermoclines in boreal lakes. *Ecosystems*, 4: 699-707.

Yajima, H. and Yamamoto, S., 2015. Improvements of radiation estimations for a simulation of water temperature in a reservoir. *Journal of Japan Society of Civil Engineers, Ser. B1 (Hydraulic Engineering*, 71(4): 775-780.

Yao, H., Samal, N.R., Joehnk, K.D., Fang, X., Bruce, L.C., Pierson, D.C., Rusak, J.A. and James, A., 2014. Comparing ice and temperature simulations by four dynamic lake models in Harp Lake: past performance and future predictions. *Hydrological Processes*, 28: 4587-4601.

Yeates, P.S. and Imberger, J., 2003. Pseudo two-dimensional simulations of internal and boundary fluxes In stratified lakes and reservoirs. *International Journal of River Basin Research,* 1: 1-23.

Zhang, W. and Arhonditsis G.B., 2009. A Bayesian hierarchical framework for calibrating aquatic biogeochemical models, *Ecological Modelling*, 220(18): 2142-2161.

Zohar, A. and Dori, Y.J., 2012. *Introduction*. In: Metacognition in science education. Springer, Netherlands. pp. 1-19.

Geoscientific
Model Development
Discussions

Revision 8 Mar 2018

Table 1. Summary of GLM parameters with recommended values and references.

Symbol	Description	Units	Value	Reference	Comments
		Physical constants			
σ	Stefan-Boltzmann constant	W m^{-2} K^{-4}	5.67x10^{-8}		
g	acceleration due to gravity	m s^{-2}	9.81		
c_a	specific heat capacity of air	J kg^{-1} °C^{-1}	1005		
c_i	specific heat capacity of air	J kg^{-1} °C^{-1}	2050	Constant	Not adjustable in glm.nml
c_w	specific heat capacity of liquid water	J kg^{-1} °C^{-1}	4185.5		
λ_v	Latent heat of evaporation	J kg^{-1}	2.453x10^6		
λ_f	Latent heat of fusion	J kg^{-1}	3.340 x10^5		
ω	ratio of molecular weight of water to molecular weight of air	-	0.622		
		Time variables			
c_{secday}	number of seconds per day	s day^{-1}	86400		
t	time	s	-		
t_b	time when a shear event begins	s	-		
$\lfloor t \rfloor$	floor of time	s	-		used to compute the time within a day, iclock
Δt	time step used by the model	s	3600		numerical time increment the model uses
d	day of the year	-	variable		
$N_{\Delta t}$	number of time-steps to simulate	-	configurable		
δt_d	time-scale of inflow parcel transport	s	computed		
δt_{wave}	period of surface waves	s	computed		Eq. 70
δt_{iw}	period for internal waves	s	computed	Spigel and Imberger (1980)	$\delta t_{iw} = L_{META}/2c$
δt_{shear}	cut-off time for internal wave induced velocity shear	s	computed		Eq. 40
δt_{damp}	time-scale of internal wave damping	s	computed	Spigel and Imberger (1980)	Eq. 43
		Lake domain (volumes, areas, heights and depths)			
N_{OUT}	number of outlets configured	-	configurable		set in &outflows
N_{INF}	number of inflows configured	-	configurable		set in &inflows
N_{LEV}	number of layers, which varies over time	-	variable		
N_{BSN}	user provided number of basin height points	-	configurable		set in &morphometry
N_{MORPH}	internally computed number of vertical height increments for the hypsographic curve	-	computed		$H_{b=N_{BSN}} \, \Delta H_{mi} + 10$
V_{max}	maximum volume of the lake	m^3	computed		once exceeded, excess water is passed to overflow
V_b	lake volume at the hyposgraphic data point b	m^3	configurable		Eq 1

Geoscientific
Model Development
Discussions

Revision 8 Mar 2018

Symbol	Description	Units	Value	Reference	Comments
V_{mi}	interpolated volume at internal morphometry table increment mi	m^3	computed		Eq. 2
V_i	volume of the lake at the top of the ith layer	m^3	variable		$\sum_{j=1}^{i} \Delta V_j$
V_s	volume of the lake at the top of the surface layer ($i = N_{LEV}$)	m^3	variable		$V[h_{i=N_{LEV}}]$
V_S^*	interim calculation of the volume of the lake at the top of the surface layer	m^3	variable		used to estimate lake volume prior to overflow calculation
ΔV_i	volume of the ith layer	m^3	variable		$V[h_i] - V[h_{i-1}]$
$\tilde{V}_{N^2}$	a fractional volume of the lake that contains 85% of N^2 variance	m^3	variable		
ΔV_{epi}	volume of the epilimnion	m^3	variable		$\Delta V_{epi} = V_s - V_{k-1}$
ΔV_{k-1}	volume of the layer below the surface mixed layer/epilimnion	m^3	variable		$V[h_{i=k-1}]$
A_{max}	maximum possible area of the lake	m^2	configurable		$A_{max} = A_{b=N_{BSN}}$
A_b	lake area above datum at the hyposgraphic data point b	m^2	configurable		set in &morphometry
A_{mi}	lake area at internal morphometry table increment mi	m^2	computed		
A_i	lake area of the ith layer	m^2	variable		
$A[H]$	lake area at a given height / elevation	m^2	configurable		area-height relationship
A_s	area of the lake surface	m^2	variable		
A_{BEN}	lake bottom (benthic) area exceeding the critical light threshold $\phi_{BEN_{crit}}$	m^2	variable		
A_E	effective area of the lake surface exposed to wind stress	m^2	computed		
A_C	critical area below which wind sheltering may occur	m^2	10^7	Xenopoulos and Schindler (2001)	
A_{outf}	area of the lake at the height of the relevant outflow	m^2	computed		
A_{k-1}	lake area at the top of the metalimnion	m^2	variable		
H	variable referring to height above datum	m above datum	-		
H_{max}	maximum height of the lake, at the lake crest	m above datum	-		set in &morphometry
H_b	height above datum at the hyposgraphic data point b	m above datum	configurable		set in &morphometry
H_{mi}	height above datum at internal morphometry table increment mi	m above datum	computed		
ΔH_{mi}	height increment used for the model's internal hyspograhic curve interpolation function	m	0.01		
h	height above a datum	m above lake bottom	-		
h_i	height above a datum at the top of layer i	m above lake bottom	variable		
h_S	height of the upper surface of the top-most (surface) layer above the datum	m above lake bottom	variable		Eq 4
h_B	height of the upper surface of the bottom-most layer above the datum	m above lake bottom	variable		Eq. 68
h_{BEN}	height at which the $\phi_{BEN_{crit}}$ is reached	m above lake bottom	variable		
$\tilde{h}_i$	height of the middle of the ith layer	m above lake bottom	variable		

Geoscientific
Model Development
Discussions

Symbol	Description	Units	Value	Reference	Comments
$\widetilde{h_{sml}}$	height of the middle of the epilimnion	m above lake bottom	variable		
h_{outf}	height of a configured outflow	m above lake bottom	configurable		
$h_{i_{ins_I}-1}$	height of the bottom of the layer where an inflow parcel associated with the Ith inflow inserted	m above lake bottom	variable		
z	depth from the lake surface, or height above the lake surface	m from water surface	-		
z_{avg}	average depth of the lake	m	variable		
z_{BEN}	depth to the lake where critical light threshold is exceeded	m from water surface	variable		Eq. 15
z_{sml}	depth to the thermocline from the surface	m from water surface	variable		Also, vertical thickness of the surface mixed layer (sml).
z/L	Monin-Obukhov stability parameter	-	computed		Eq. A26
z_o	water surface roughness length	m	computed		Eq. A24
z_θ	water surface heat roughness length	m	computed		
z_e	water surface moisture roughness length	m	computed		
$z_{inf_{ins_I}}$	depth that an inflow parcel associated with inflow I inserts	m from water surface	variable		Depth from the surface where an inflow reaches its level of neutral buoyancy
Δz_i	thickness of the ith layer	m	variable		
Δz_{k-1}	thickness of the layer below the epilimnion	m	variable		
Δz_{min}	minimum layer thickness	m	0.5	Bruce et al. (2017) Bueche et al. (2017)	Should be estimated relative to lake depth; set in &glm_setup
Δz_{max}	maximum layer thickness	m	1.5		
Δz_{ice}	combined thickness of the white ice and blue ice	m	computed		$\Delta z_{white} + \Delta z_{blue}$
$\Delta z_{ice,snow}$	thickness of top layer of ice cover, depending on ice or snow presence	m	computed		Eq. 29
Δz_{snow}	thickness of snow	m	variable		Eq. 29; Fig. 6
Δz_{white}	thickness of white ice	m	variable		Eq. 29
Δz_{blue}	thickness of blue ice	m	variable		Eq. 32
Δz_{inf_0}	thickness of an inflow parcel before transport into the lake	m	computed		Eq. 55
Δz_{inf_j}	thickness of inflow parcel j	m	variable		Eq. 57
δz_{inf_j}	vertical transport length of inflow parcel j	m	variable		$\delta z_{inf_j} = \left(h_s - z_{inf_j}\right) - h_{i_{j-1}}$
δz_{wave}	significant wave height of surface waves	m	computed		Eq. 73
δz_{soil}	thickness of soil layer	m	0.5		Relevant layer thickness for computing sediment heat diffusion or water seepage
Simulation variables and parameters					
a	Charnock constant	-	0.012		
c	internal wave speed	m s^{-1}	computed		Eq. 41

Geoscientific
Model Development
Open Access
Discussions
EGU

Revision 8 Mar 2018

Symbol	Description	Units	Value	Reference	Comments
c_{damp}	coefficient related to damping rate of internal waves	-	104.1	Spigel (1978)	
C_i	concentration of relevant scaler, including, salinity or water quality variable, in the ith layer	various	variable		Eq. 51
$\bar{C}$	mean concentration of two or more layers	various	variable		
ΔC	difference in concentration of two layers	various	variable		
C_{KH}	Mixing efficiency - Kelvin-Helmholtz turbulent billows	-	0.3	Sherman et al. (1978)	"a good rule of thumb..."
C_{HYP}	mixing efficiency of hypolimnetic turbulence	-	0.5	Weinstock (1981)	General diffusivities in Jellison and Melack (1993)
C_T	Mixing efficiency - unsteady turbulence (acceleration)	-	0.51	Sherman et al. (1978) Spigel et al. (1986) Yeates & Imberger (2003)	
C_S	Mixing efficiency - shear production	-	0.3		Best fit of experiments reviewed
C_W	Mixing efficiency - wind stirring	-	0.23		From Wu (1973)
C_K	Mixing efficiency - convective overturn	-	0.2		Selected from a range given in Spigel et al. (1986)
$C_{D_{inf}}$	stream-bed drag of inflowing rivers	-	0.016		set based on inflow bed roughness
$C_{D_{weir}}$	drag associated with weir crest	-	0.62		
C_D	bulk aerodynamic coefficient for momentum	-	0.0013	Fischer et al. (1979) Bruce et al. (2017) Bueche et al. (2017)	see also Appendix B; Eq A23
C_E	bulk aerodynamic coefficient for latent heat transfer	-	0.0013		From Hicks' (1972) collation of ocean and lake data; many studies since use similar values.
C_H	bulk aerodynamic coefficient for sensible heat transfer	-	0.0013		Internally calculated if atmos stability correction is on.
C_{XN}	generic notation for neutral value of bulk transfer coefficient	-	-		X = H or E
C_{DN-10}	value of bulk transfer coefficient for momentum under neutral atmospheric conditions, referenced to 10m height.	-	computed		
C_{HWN-10}	value of bulk transfer coefficient for heat/moisture under neutral atmospheric conditions, referenced to 10m height.	-	0.0013		see also Appendix B
C_x	cloud cover fraction	-	time-series input		
D_Z	effective vertical diffusivity of scalars in water	$m^2 s^{-1}$	computed		
D_ε	diffusivity of scalars in water due to turbulent mixing	$m^2 s^{-1}$	computed		
D_m	molecular diffusivity for scalars in water	$m^2 s^{-1}$	1.25×10^{-9}		
D_a	molecular heat diffusivity of air	$m^2 s^{-1}$	2.14×10^{-5}	TVA (1972)	Reported as 0.077 $m^2 hr^{-1}$
D_{outf}	average vertical diffusivity of scalars in layers spanning the withdrawal thickness	$m^2 s^{-1}$	computed	Imberger and Patterson (1981)	
e_s	saturation vapour pressure	hPa	computed	various	Eq. 22
e_a	atmospheric vapour pressure	hPa	computed		Eq. 23
e_*			-		
E_{TKE}	turbulent kinetic energy available for mixing, per mass per wavenumber	$m^3 s^{-2}$	-	Imberger and Patterson (1981)	Eq. 34

Geoscientific
Model Development
Discussions

Revision 8 Mar 2018

Symbol	Description	Units	Value	Reference	Comments
E_{PE}	potential energy within the stratified water column	m^2 s^{-2}	-	Hamilton and Schladow (1997)	Eq. 35
E	evaporation mass flux	m s^{-1}	variable		
E_{inf}	inflow entrainment	-	computed		Eq. 53
F	fetch	m	computed		estimated as the square root of the lake area, Eq. 69
Fr	internal Froude number of the lake subject to a water withdrawal	-	computed		Eq. 61
f_R, f_S	rainfall scaling factor	-	1		used to adjust/calibrate model to meteorological data
f_{SW}	solar radiation scaling factor	-	1		
f_U	wind-speed scaling factor	-	1		
f_{AT}	air temperature scaling factor	-	1		
f_{RH}	relative humidity scaling factor	-	1		
f_{inf}	inflow rate scaling factor	-	1		
f_{outf}	outflow rate scaling factor	-	1		
f_{SWE}	snow water equivalent fraction	m rain/m snow	0.1		
f_{WS}	wind-sheltering scaling factor	-	1		function used to scale the wind-sheltering length scale or lake surface area, based on the direction of the wind
f_{ro}	runoff coefficient	m runoff/m rain	0.2		depends on land slope and soil type
f_{PAR}	fraction of global incoming radiation flux which is photosynthetically active	-	0.45	Jellison and Melack (1993)	
f_{VIS}	visible bandwidth fraction	-	0.3	Rogers et al. (1995)	
$f_{BEN_{crit}}$	fraction of surface irradiance at the benthos, which is considered critical for productivity	-	0.2		set in &glm_setup
f_w	friction factor used for current stress calculation	-	computed	Kleinhans and Grasmeijer (2006)	Eq. 78
f_c	friction factor used for wave stress calculation	-	computed		
f_0	roughness correction coefficient for the lake surface	-	0.5	TVA (1972)	
f_{dif}	smoothing factor used for diffusion	-	computed		Eq. 52
g'_k	reduced gravity between the mixed layer and the $k-1$ layer	m s^{-2}	computed		
g'_{EH}	reduced gravity between the epilimnion and the hypolimnion	m s^{-2}	computed		
g'_{inf}	reduced gravity between the inflowing water and adjacent lake water	m s^{-2}	computed		
G	seepage rate	m day^{-1}	0		
Gr	Grashof number related to an outflow extraction	-	computed	Imberger and Patterson (1981)	Eq. 62
k_{TKE}	turbulence wavenumber	m^{-1}	computed		Eq. 46
K_w	light extinction coefficient	m^{-1}	0.5		set in &glm_setup, or form the linked water quality model. Can be estimated from Secchi depth.

Geoscientific
Model Development
Discussions

Revision 8 Mar 2018

Symbol	Description	Units	Value	Reference	Comments
K_{w1}	Waveband 1, snow ice light extinction	m^{-1}	48.0	Rogers et al., (1995), Patterson and Hamblin (1988) Ashton (1986) Yao et al., (2014)	
K_{w2}	Waveband 2, snow ice light extinction	m^{-1}	20.0		
K_{b1}	Waveband 1, blue ice light extinction	m^{-1}	1.5		
K_{b2}	Waveband 2, blue ice light extinction	m^{-1}	20.0		
K_{s1}	Waveband 1, snow light extinction	m^{-1}	6		
K_{s2}	Waveband 2, snow light extinction	m^{-1}	20		
K_{snow}	molecular heat conductivity of snow	J m^{-1} s^{-1} °C^{-1}	computed		Fig. 6
$K_{ice_{white}}$	molecular heat conductivity of white ice	J m^{-1} s^{-1} °C^{-1}	2.3		
$K_{ice_{blue}}$	molecular heat conductivity of blue ice	J m^{-1} s^{-1} °C^{-1}	2.0		
K_{water}	molecular heat conductivity of water	J m^{-1} s^{-1} °C^{-1}	0.57		
K_{air}	molecular heat conductivity of air	J m^{-1} s^{-1} °C^{-1}	2.8x10^{-3}	TVA (1972)	Reported as 0.1 kJ m^{-1} hr^{-1} K^{-1}
L_D	equivalent circular diameter of the lake	m	computed		
L_{META}	length of the lake at the depth of the thermocline region (metalimnion)	m	computed		
L_{outf}	length of the lake at the height of the relevant outflow	m	computed		
L_{crest}	length of the lake at the upper most height of the domain	m	configurable		
m	constant used to compute the rate at which work from the wind is converted	-	4.6x10^{-7}		
N^2	the buoyancy frequency, a measure of water column stratification	s^{-2}	computed		
N^2_{outf}	the buoyancy frequency, a measure of water column stratification, about the layers impacted by the water outflow	s^{-2}	computed		
p	air pressure	hPa	1013	-	assumed constant
Q_{inf_x}	rate of water inflow provided by the user as input to the model	m^3 day^{-1}	time-series input		
Q_{inf_0}	rate of water inflow prior to the inflow entering the lake	m^3 s^{-1}	computed		$Q_{inf_0} = f_{inf}\, Q_{inf_x}/c_{secday}$
Q_{inf_j}	flow rate of inflow water parcel during transit, at the jth increment	m^3 s^{-1}	variable		Eq. 60 used to increment between j steps
$Q_{inf_{ins_I}}$	flow rate of inflowing water at the point of insertion, for inflow, I	m^3 s^{-1}	variable		
Q_{outf_x}	rate of water outflow provided by the user as input to the model	m^3 day^{-1}	time-series input		
Q_{outf_i}	flow rate of water being extracted from the ith layer	m^3 s^{-1}	computed		
Q_{ovfl}	rate of over flowing water leaving the lake	m^3 s^{-1}	computed		Eq. 73
Q_{weir}	flow rate of water discharging over the crest, before flooding	m^3 s^{-1}	computed		Eq. 72
Q_R	boundary run-off into the lake surface layer	m^3 s^{-1}	computed		
R	dimensionless parameter describing a water withdrawal flow regime	-	computed		
R_L	rainfall intensity threshold before run-in occurs	m day^{-1}	0.04		depends on land slope and soil type
RH_x	relative humidity	-	time-series input		user supplied relative humidity between 0 and 1

Geoscientific
Model Development
Discussions

Revision 8 Mar 2018

Symbol	Description	Units	Value	Reference	Comments
R_F	rainfall rate	m s^{-1}	computed		Eq 5
R_x	rainfall rate supplied in the input file	m day^{-1}	time-series input		user supplied rainfall rate
r	mixing ratio	-	computed		ratio of water mass to total air mass
Ri_{inf}	Richardson number of the inflow water	-	computed		Eq. 54
Ri_B	bulk Richardson number of the atmosphere over the lake	-	computed		A34
S_x	snowfall rate supplied in the input file	m day^{-1}	time-series input		user supplied snowfall rate
S_F	snowfall rate	m s^{-1}	computed		Eq 6.
S_i	salinity of the ith layer	ppt	variable		
S_{inf_x}	salinity of water entering in an inflow	g m^{-3}	time-series input		
T_s	temperature of the surface layer	°C	variable		Eq. 8
T_x	air temperature supplied by the user	°C	time-series input		user supplied air temperature
T_a	air temperature	°C	computed		$T_a = f_{AT} T_x$
T_i	temperature of the ith layer	°C	variable		
T_m	melt-water temperature	°C	0		
T_0	temperature at the solid surface	°C	variable		
T_{inf_x}	temperature of water entering in an inflow	°C	time-series input		
θ_V	virtual temperature of the atmospheric boundary layer above the lake	°K	computed		
θ_a	temperature of the atmospheric boundary layer above the lake	°K	computed		$\theta_a = f_{AT} T_x + 273.15$
θ_s	temperature of the atmospheric at the lake surface	°K	variable		$\theta_a = T_s + 273.15$
θ_*					
U_{10}	wind speed above the lake referenced to 10m height	m s^{-1}	-		wind speed corrected to reference height
U_x	wind speed above the lake surface provided by the user	m s^{-1}	time-series input		user supplied snowfall rate
U_{orb_i}	orbital wave velocity experienced at the bottom of the ith layer	m s^{-1}	variable		Eq. 75
U_{m_i}	mean layer velocity of the ith layer	m s^{-1}	variable		Eq. 77
u_{inf_j}	average velocity of an inflow parcel being tracked, prior to insertion	m s^{-1}	variable		Eq. 59
u_*	friction velocity	m^3 s^{-3}	computed		Eq. 37
u_b	velocity shear at the base of the thermocline	m s^{-1}	variable		Eq. 39
$u_{b_{old}}$	velocity shear at the thermocline at the previous time-step	m s^{-1}	variable		reset between shear events
W_{crest}	width of the lake at the upper most point	m	configured		
W_{outf}	width of the lake at the height of an outflow	m	computed		Eq. 65
w_*^3	turbulent velocity scale within the surfaced mixed layer, due to convective cooling	m s^{-1}	computed	Imberger and Patterson (1981)	Eq 36

Geoscientific
Model Development
Discussions

Revision 8 Mar 2018

Symbol	Description	Units	Value	Reference	Comments
x_{WS}	default sheltering distance defined as the distance from the shoreline at which wind stress is no longer affected by sheltering	m	configurable	Marrkfort et al (2009)	Approximated as 50x the vertical height of the sheltering obstacle/landform
$x_{WS}{}^{\Phi}$	sheltering distance adjusted for changes in wind direction	m	computed		$x_{WS}{}^{\Phi} = x_{WS}\,(1 - min(f_{WS}[\Phi_{wind}], 1))$
δx_{wave}	wave length of surface waves	m	computed		Eq. 72
Δx_{inf_j}	lateral distance travelled by an inflow parcel per j increment, prior to insertion	m	computed		Eq. 58
α_{inf}	half-angle of inflow river channel	deg	configurable		user supplied based on width and depth of the relevant river
α_h	coefficient for sensible heat flux into still air	J m^{-2} s^{-1} °C^{-1}	computed	TVA (1972)	Eq. 27b
α_e	coefficient for evaporative flux into still air	m s^{-1}	computed	TVA (1972)	Eq. 27a
α_{LW}	longwave albedo	-	0.03		
α_{SW}	albedo of shortwave radiation at the water surface	-	0.08		Eq. 12
α_{SKY}	scattered radiation within the sky	-	computed	Bird (1984)	$\alpha_{SKY} = 0.0685 + (1 - 0.84)(1 - T_{as})$
α_b	interpolation coefficient for volume	-	computed		Eq. 3
β_b	interpolation coefficient for area	-	computed		Eq. 3
δ_{wi}	length-scale associated with conduction of heat at the ice-water interface	m	0.039	Rogers *et al.* (1995)	
δ_{KH}	length-scale associated with formation of Kelvin-Helmholtz billows at the interface of two-layer stratification	m	computed	Imberger and Patterson (1981)	
δ_{outf}	length-scale associated with the vertical thickness of the zone of influence of a withdrawal	m	computed	Imberger and Patterson (1981)	Eq. 66
$\delta_{outf_{top}}$	thickness of withdrawal layer above the withdrawal height	m	computed		
$\delta_{outf_{bot}}$	thickness of withdrawal layer below the withdrawal height	m	computed		
δ_{ss}	particle diameter of bottom sediment	m	80x10^{-6}		
ε_{TKE}	TKE dissipation flux per unit mass	m^2 s^{-3}	-		Eq. 48
$\overline{\varepsilon_{TKE}}$	steady-state/equilibrium TKE dissipation flux per unit mass	m^2 s^{-3}	computed		Eq. 49
ε_{WIND}	TKE dissipation flux created by power introduced by the wind	m^2 s^{-3}	computed		Eq. 49
ε_{INFLOW}	TKE dissipation flux caused by inflow plunging creating seiching	m^2 s^{-3}	computed		Eq. 49
ε_w	emissivity of the water surface	-	0.985		
ε_a	emissivity of the atmosphere under cloud-free conditions	-			
ε_a^*	emissivity of the atmosphere including cloud reflection	-	computed	Henderson-Sellers (1986)	Eq. 19
ϕ_{SW_x}	shortwave radiation flux provided in the input file	W m^{-2}	time-series input	-	user supplied solar radiation data
ϕ_{SW_S}	shortwave radiation flux crossing the water surface	W m^{-2}	computed	-	Eq. 9.
$\hat{\phi}_{SW}$	total incident shortwave radiation flux computed from the BCSM assuming clear-sky conditions	W m^{-2}	computed	Bird (1984)	Eq. 10 and Appendix A

Geoscientific
Model Development
Discussions

Revision 8 Mar 2018

Symbol	Description	Units	Value	Reference	Comments
$\hat{\phi}_{DB}$	direct beam radiation on a horizontal surface at ground level on a clear day	W m^{-2}	computed	Bird (1984)	Eq. A19
$\hat{\phi}_{AS}$	radiation from atmospheric scattering hitting ground level on a clear day	W m^{-2}	computed	Bird (1984)	Eq. A20
ϕ_{PAR}	downwelling PA radiation intensity within the water column	W m^{-2}	computed	Kirk (1994)	Eq. 13
$\phi_{PAR_{BEN}}$	light incident on the bottom of a layer, corresponding to the benthic area	W m^{-2}	variable	-	
ϕ_{LWin}	longwave radiation incident heat flux at the water surface	W m^{-2}	variable		Eq. 18
ϕ_{LWout}	longwave radiation outgoing heat flux from the water surface	W m^{-2}	variable		Eq. 17
$\phi_{LW_{net}}$	net longwave radiation flux across the lake surface	W m^{-2}	computed		Eq. 16
ϕ_H	sensible heat flux across the water surface	W m^{-2}	computed		Eq. 20
ϕ_E	latent heat flux	W m^{-2}	computed		Eq. 21
ϕ_{E_0}	latent heat flux under zero-wind conditions	W m^{-2}	computed		Eq. 26a
ϕ_{H_0}	sensible heat flux under zero-wind conditions	W m^{-2}	computed		Eq. 26b
ϕ_X	generic identifier for either of ϕ_E or ϕ_H	W m^{-2}	computed		
ϕ_{X_0}	generic identifier for either of ϕ_{E_0} or ϕ_{H_0}	W m^{-2}	computed		
ϕ_X^*	maximum value of either ϕ_{X_0} or ϕ_X	W m^{-2}	selected		Eq. 21
ϕ_0	upward conductive heat flux through the ice and snow cover to the atmosphere	W m^{-2}	computed		
ϕ_{net}	net incoming heat flux at the ice-atmosphere interface	W m^{-2}	computed	Rogers et al. (1995)	Eq. 29
ϕ_R	heat flux due to rainfall	W m^{-2}	computed	Rogers et al. (1995)	
ϕ_f	heat flux at the ice-water interface into the blue ice	W m^{-2}	computed		Eq. 31
ϕ_w	heat flux from the water to the blue ice	W m^{-2}	computed		Eq. 33
ϕ_{white}^*	Heat flux per unit volume due to formation of white ice by flooding	W m^{-2}	computed	Rogers et al. (1995)	
Φ_{wind}	wind direction	degrees	time-series input		optionally provided as a boundary condition
Φ_{inf}	slope of inflow coming into the lake	degrees			user provided in &inflow
Φ_{zen}	solar zenith angle	radians	variable		
SZA	solar zenith angle	degrees	variable		SZA = $\Phi_{zen}180/\pi$
ρ_a	air density	kg m^{-3}	computed	TVA (1972)	computed as a function of air temperature, humidity and pressure in atm_density
ρ_o	density of saturated air at the water surface temperature	kg m^{-3}	computed	TVA (1972)	
ρ_i	density of the ith layer	kg m^{-3}	variable	UNESCO (1981)	compute for each layer based on temperature and salinity
ρ_s	density of the surface water layer (i=N$_{LEV}$)	kg m^{-3}	variable		
ρ_{sml}	mean density of the mixed layer	kg m^{-3}	variable		

Geoscientific
Model Development
Discussions

Revision 8 Mar 2018

Symbol	Description	Units	Value	Reference	Comments
ρ_{ref}	average of layer densities over which reduced gravity is being computed	kg m^{-3}	computed		
$\rho_{ice,snow}$	density of the snow or ice	kg m^{-3}	selected		
ρ_{white}	density of snow ice	kg m^{-3}	890		
ρ_{blue}	density of blue ice	kg m^{-3}	917		
ρ_{snow}	density of snow	kg m^{-3}	variable		
$\rho_{s,min}$	assigned minimum snow density	kg m^{-3}	50		
$\rho_{s,max}$	assigned maximum snow density	kg m^{-3}	300		
ρ_{snow*}	intermediate snow density estimate	kg m^{-3}	computed		see Figure 6
ρ_{outf}	density of the lake layer corresponding to the height of withdrawal, i_{outf}	kg m^{-3}	computed		
ρ_{i_j}	density of the lake layer, i, which is at an equivalent depth to inflow parcel j	kg m^{-3}	computed		
ρ_{inf}	density of inflowing water	kg m^{-3}	computed		
ρ_{ins_I}	density of the inflow parcel associated with inflow I when it inserted	kg m^{-3}	computed		
$\rho_{i_{ins_I}}$	density of the lake layer, i, where the inflow I inserted	kg m^{-3}	computed		
κ	von Karman's constant	-	0.41		
ϑ_s	dimensionless moisture content of air at water's surface	-	computed	TVA (1972)	$\vartheta_s = \kappa\, e_s / p$
ϑ_a	dimensionless moisture content of the air above the lake	-	computed	TVA (1972)	$\vartheta_a = \kappa\, e_a / p$
ν_a	kinematic viscosity of air	m^2 s^{-1}	1.52×10^{-5}	TVA (1972)	Reported as 0.0548 m^2 hr^{-1}
ν_w	kinematic viscosity of water	m^2 s^{-1}	1.14×10^{-6}		
τ_i	total shear stress experienced at the lake bed portion of layer i	N m^{-2}	computed		Eq. 76
ψ_M	similarity function for momentum in the air above the lake	-	computed		Eq. A30
ψ_E	similarity function for moisture in the air above the lake	-	computed		Eq. A30
ψ_H	similarity function for heat in the air above the lake	-	computed		Eq. A30
ξ	dimensionless parameter used for wave period calculation	-	computed		Eq. 71
ζ	dimensionless parameter used for wave period calculation	-	computed		Eq. 74
ς	constant related to atmospheric diffuse radiation	-	6	Yajima and Yamamoto (2015)	
Indices					
b	hyposgraphic data point index	-	index		
mi	internal hyposgraphic curve increment	-	index		
i	index of computational layer	-	index		
i_j	index of the lake layer at an equivalent depth to inflow parcel j	-	index		

Revision 8 Mar 2018

Symbol	Description	Units	Value	Reference	Comments
i_{bot}	index of lower most layer impacted by a given withdrawal/outflow	-	index		
i_{top}	index of the upper-most layer impacted by a given withdrawal/outflow	-	index		
i_{outf}	index of the lake layer aligning with a withdrawal/outflow extraction point	-	index		
s	layer index of the layer at the surface of the lake	-	index		
k	layer index of the layer at the bottom of the surface mixed layer (sml; epilimnion)	-	index		
j	index of inflow parcel transport, prior to insertion	-	index		
I	inflow index	-	index		
O	outflow index	-	index		

Geoscientific
Model Development
Discussions

Appendix A: Bird solar radiation model

The Bird Clear Sky Model (BCSM) was developed by (Bird, 1984) to predict clear-sky direct beam, hemispherical diffuse, and total hemispherical broadband solar radiation on a horizontal surface. Average solar radiation is computed at the model time-step (e.g., hourly) based on ten user specified input parameters (Table A1).

5

Table A1: Parameters required for the BCSM model.

Variable	Description	Example values (e.g., Luo et al., 2010)
Lat	Latitude (degrees, + for N)	-31.77
Long	Longitude (degrees + for E)	116.03
TZ	Time Zone indicated by number of hours from GMT	+7.5
AP	Atmospheric Pressure (millibars)	1013
Oz	Ozone Conc. (atm-cm)	0.279 - 0.324
W	Total Precipitable Water Vapour (atm-cm)	1.1 - 2.2
AOD_{500}	Aerosol Optical Depth at 500 nm	$0.033 - 0.1$
AOD_{380}	Aerosol Optical Depth at 380 nm	$0.038 - 0.15$
α_{SW}	Surface albedo	0.2

The solar constant in the model is taken as 1367 W m^{-2}. This is corrected due to the elliptical nature of the earth's orbit and consequent change in distance to the sun. This calculation gives us the Extra-Terrestrial Radiation ($\hat{\phi}_{ETR}$), at the top of the
10   atmosphere:

$$\hat{\phi}_{ETR} = 1367\left(1.00011 + 0.034221\cos(\Phi_{day}) + 0.00128\sin(\Phi_{day}) + 0.000719\cos(\Phi_{day})\right) \qquad \text{A1}$$

where the day angle, Φ_{day}, is computed using, d, the day number:

$$\Phi_{day} = 2\pi\left(\frac{d-1}{365}\right) \qquad \text{A2}$$

The solar declination, Φ_{dec} (radians), is computed from:

$$\Phi_{dec} = \begin{bmatrix} 0.006918 - 0.399912\cos(\Phi_{day}) + 0.070257\sin(\Phi_{day}) - 0.006758\cos\left(2(\Phi_{day})\right) + \\ 0.000907\sin(2\Phi_{day}) - 0.002697\cos\left(3(\Phi_{day})\right) + 0.00148\sin\left(3(\Phi_{day})\right) \end{bmatrix} \qquad \text{A3}$$

15   We then solve the equation of time:

$$EQT = \begin{bmatrix} 0.0000075 + 0.001868\cos(\Phi_{day}) - 0.032077\sin(\Phi_{day}) \\ -0.014615\cos\left(2(\Phi_{day})\right) - 0.040849\sin\left(2(\Phi_{day})\right) \end{bmatrix} \times 229.18 \qquad \text{A4}$$

in order to compute the hour angle, Φ_{hr}, calculated with noon zero and morning positive as:

$$\Phi_{hr} = 15(hr - 12.5) + Long - 15\,TZ + \left(\frac{EQT}{4}\right) \tag{A5}$$

where TZ is the time-zone shift from GMT. The zenith angle, Φ_{zen} (radians), is calculated from:

$$\cos(\Phi_{zen}) = \cos(\Phi_{dec})\cos(\Phi_{hr})\cos(Lat) + \sin(\Phi_{dec})\sin(Lat) \tag{A6}$$

When Φ_{zen} is less than 90°, the air mass factor is calculated as:

$$AM = \left[cos(\Phi_{zen}) + \frac{0.15}{(93.885 - \Phi_{zen})^{1.25}}\right]^{-1} \tag{A7}$$

5   which is corrected for atmospheric pressure, p (hPa),

$$AM_p = \frac{AM\,p}{1013} \tag{A8}$$

AM_P is then used to calculate the Rayleigh Scattering as:

$$T_{rayleigh} = e^{[(-0.0903\,AM_p{}^{0.84})+(1+AM_p-AM_p{}^{1.01})]} \tag{A9}$$

The effect of ozone scattering is calculated by computing ozone mass, which for positive air mass is:

$$T_{ozone} = \left[1 - \left(0.1611\,(Oz\,AM)\left(1 + 139.48\,(Oz\,AM)\right)^{-0.3035}\right)\right.$$
$$\left. - \frac{0.002715\,(Oz\,AM)}{1 + 0.044\,(Oz\,AM) + 0.0003\,(Oz\,AM)^2}\right] \tag{A10}$$

10   The scattering due to mixed gases for positive air mass is calculated as:

$$T_{mix} = e^{[-0.0127\,AMp^{0.26}]} \tag{A11}$$

Then the water scattering is calculated by getting the water mass:

$$Wm = W\,AM_p \tag{A12}$$

where W is the precipitable water vapour. This can be approximated from dew point temperature, eg.:

$$\ln W = a\,T_d + b \tag{A13}$$

where a and b are regression coefficients which have been taken as 0.09, 0.07, 0.07 and 0.08 for values of a, while b is 1.88,

15   2.11, 2.12 and 2.01 in spring, summer, autumn and winter (Luo et al., 2010).

Then the water scattering effect is calculated as:

$$T_{water} = \left[1 - \frac{(2.4959\,Wm)}{1 + (79.034\,Wm)^{0.6828} + 6.385\,Wm}\right] \tag{A14}$$

The scattering due to aerosols requires the Aerosol Optical Depth at 380 nm and 500 nm:

$$TauA = 0.2758\,AOD_{380} + 0.35\,AOD_{500} \tag{A15}$$

20   and the scattering due to aerosols is then calculated as:

$$T_{aerosol} = e^{(-TauA)^{0.873}\,(1+TauA-TauA^{0.7088})\,AM^{0.9108}} \tag{A16}$$

We also define:

Revision 8 Mar 2018

$$T_{aa} = 1 - [0.1 \, (1 - AM + AM^{1.06}) \, (1 - T_{aerosol})] \qquad\text{A17}$$

and:

$$\frac{0.5(1 - T_{rayleigh}) + 0.84(1 - T_{as})}{1 - AM + AM^{1.02}} \qquad\text{A18}$$

where the 0.84 value used is actually the proportion of scattered radiation reflected in the same direction as incoming radiation.

5

The direct beam radiation on a horizontal surface at ground level on a clear day is given by,

$$\hat{\phi}_{DB} = 0.9662 \, \hat{\phi}_{ETR} \, T_{rayleigh} \, T_{ozone} \, T_{mix} \, T_{watvap} \, T_{aerosol} \, cos(\Phi_{zen}) \qquad\text{A19}$$

$$\hat{\phi}_{AS} = 0.79 \, \hat{\phi}_{ETR} \, T_{ozone} \, T_{mix} \, T_{watvap} \, T_{aa} \, cos(\Phi_{zen}) \qquad\text{A20}$$

The total irradiance hitting the surface is therefore (W m^{-2}):

$$\hat{\phi}_{SW} = \frac{\hat{\phi}_{DB} + \hat{\phi}_{AS}}{1 - (\alpha_{SW} \, \alpha_{SKY})} \qquad\text{A21}$$

The albedo is computed for the sky as:

$$\alpha_{SKY} = 0.068 + (1 - 0.84) \left(1 - \frac{T_{aerosol}}{T_{aa}}\right) \qquad\text{A22}$$

10

Revision 8 Mar 2018

Appendix B: Non-neutral bulk transfer coefficients

The iterative procedure used in this analysis to update correct the bulk-transfer coefficients based on atmospheric conditions is conceptually similar to the methodology discussed in detail in Launiainen and Vihma (1990). The first estimate for the neutral drag coefficient, C_{DN}, is specified as a function of wind speed as it is commonly observed to increase with U_{10}. This is

5   modelled by first estimating the value referenced to 10m height above the water from:

$$C_{DN-10} = \begin{cases} 0.001 & U_{10} \leq 5 \\ 0.001 \, (1 + 0.07[U_{10} - 5]) & U_{10} > 5 \end{cases} \qquad \text{Option 1 : Francey and Garratt (1978), Hicks (1972)} \qquad \text{A23}$$

$$C_{DN-10} = 1.92 \times 10^{-7} U_{10}^3 + 0.00096 \qquad \text{Option 2 : Babanin and Makin (2008)}$$

and then computing the Charnock formula with the smooth flow transition (e.g., Vickers et al., 2013):

$$z_o = \frac{a u_*^2}{g} + 0.11 \frac{\nu_a}{u_*} \qquad \text{A24}$$

where a is the Charnock constant (0.012), u_* is the approximated friction velocity ($\sqrt{C_{DN-10} \, U_{10}^2}$) using Eq A23. The drag is re-computed using:

$$C_{DN-10} = \left[\frac{\kappa}{\ln\left(\frac{10}{z_o}\right)} \right]^2 \qquad \text{A25}$$

where κ is the von Karman constant (Figure A1). Note the neutral humidity/temperature coefficient, C_{HWN-10}, is held constant

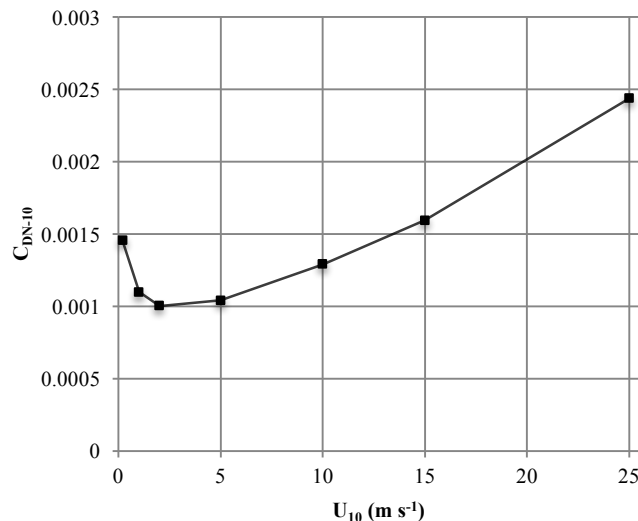10   at the user defined C_H value and is assumed not to vary with wind speed.

Figure A1: Scaling of the 10-m neutral drag coefficient with wind speed, U_{10} (Eqns A23-25)

Under non-neutral conditions in the atmospheric boundary layer, the transfer coefficients vary due to stratification in the air column, as was parameterised by Monin and Obukhov (1954) using the now well-known stability parameter, z/L, where L is the Obukhov length defined as:

$$L = \frac{-\rho_a u_*^3 \theta_V}{\kappa \, g \left(\frac{\phi_H}{c_a} + 0.61 \frac{\theta_a \phi_E}{\lambda_v} \right)} \qquad \text{A26}$$

where $\theta_V = \theta_a (1 + 0.61 e_a)$ is the virtual air temperature and ϕ_H and ϕ_E are the bulk fluxes. Paulson (1970) presented a

5   solution for the vertical profiles of wind speed, temperature and moisture in the developing boundary layer as a function of the Monin-Obukhov stability parameter; the so-called flux-profile relationships:

$$U_z = \frac{u_*}{\kappa} \left[\ln \left(\frac{z}{z_o} \right) - \psi_M \left(\frac{z}{L} \right) \right] \qquad \text{A27a-c}$$

$$\theta_a - \theta_s = \frac{\theta_*}{\kappa} \left[\ln \left(\frac{z}{z_\theta} \right) - \psi_H \left(\frac{z}{L} \right) \right]$$

$$e_a - e_s = \frac{e_*}{\kappa} \left[\ln \left(\frac{z}{z_e} \right) - \psi_E \left(\frac{z}{L} \right) \right]$$

where ψ_M, ψ_H and ψ_E are the similarity functions for momentum, heat and moisture respectively, and z_o, z_θ and z_e are their respective roughness lengths. For unstable conditions ($L<0$), the stability functions are defined as (Paulson 1970; Businger et al., 1971; Dyer, 1974):

$$\psi_M = 2 \ln \left(\frac{1+x}{2} \right) + \ln \left(\frac{1+x^2}{2} \right) - 2 \tan^{-1} x + \frac{\pi}{2} \qquad \text{A28a}$$

$$\psi_E = \psi_H = 2 \ln \left(\frac{1+x^2}{2} \right) \qquad \text{A28b}$$

10   where

$$x = \left[1 - 16 \left(\frac{z}{L} \right)^{1/4} \right] \qquad \text{A29}$$

During stable stratification ($L>0$) they take the form:

$$\psi_M = \psi_E = \psi_H = \begin{cases} -5 \left(\frac{z}{L} \right) & 0 < \frac{z}{L} < 0.5 \\ 0.5 \left(\frac{z}{L} \right)^{-2} - 4.25 \left(\frac{z}{L} \right)^{-1} - 7 \left(\frac{z}{L} \right) \ - 0.852 & 0.5 < \frac{z}{L} < 10 \\ \ln \left(\frac{z}{L} \right) - 0.76 \left(\frac{z}{L} \right) - 12.093 & \frac{z}{L} > 10 \end{cases} \qquad \text{A30}$$

Substituting Eqns. 20-21 into (A27) and ignoring the similarity functions leaves us with neutral transfer coefficients as a

15   function of the roughness lengths:

$$C_{XN} = \kappa^2 \left[\ln \left(\frac{z}{z_o} \right) \right]^{-1} \left[\ln \left(\frac{z}{z_X} \right) \right]^{-1} \qquad \text{A31}$$

Revision 8 Mar 2018

where the N sub-script denotes the neutral value and X signifies either D, H or E for the transfer coefficient and o, θ or e for the roughness length scale. Inclusion of the stability functions into the substitution and some manipulation (Imberger and Patterson, 1990; Launianen and Vihma, 1990) yields the transfer coefficients relative to these neutral values:

$$\frac{C_X}{C_{XN}} = \left[1 + \frac{C_{XN}}{\kappa^2}\left(\psi_M\psi_X - \frac{\kappa\psi_X}{\sqrt{C_{DN}}} - \frac{\kappa\psi_M\sqrt{C_{DN}}}{C_{XN}}\right)\right] \qquad \text{A32}$$

5

Hicks (1975) and Launianen and Vihma (1990) suggested an iterative procedure to solve for the stability corrected transfer coefficient using (A32) based on some initial estimate of the neutral values (as input by the user). The surface flux is subsequently estimated according to Eqns. 20-21 and used to provide an initial estimate for L (Eq. A26). The partially corrected transfer coefficient is then recalculated and so the cycle goes. Strub and Powell (1987) and Launiainen (1995), presented an

10 alternative based on estimation of the bulk Richardson number, Ri_B, defined as:

$$Ri_B = \frac{gz}{\theta_V}\left(\frac{\Delta\theta + 0.61\,\theta_V\Delta e}{U_z^2}\right) \qquad \text{A33}$$

and related as a function of the stability parameter, z/L, according to:

$$Ri_B = \frac{z}{L}\left(\frac{\kappa\sqrt{C_{DN}}/C_{HWN} - \psi_{HW}}{\left[\kappa/\sqrt{C_{DN}} - \psi_M\right]^2}\right) \qquad \text{A34}$$

where it is specified that $C_{HN} = C_{WN} = C_{HWN}$. Figure A2 illustrates the relationship between the degree of atmospheric stratification (as described by both the bulk Richardson number and the Monin-Obukhov stability parameter) and the transfer coefficients scaled by their neutral value.
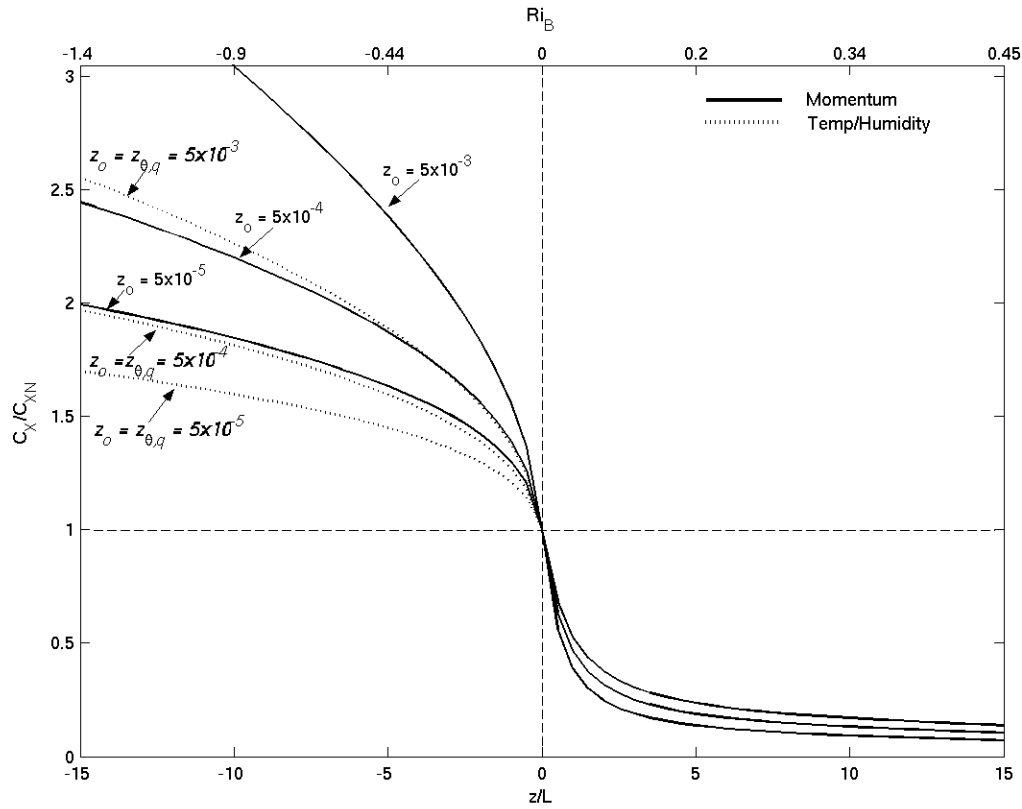
Figure A2: Relationship between atmospheric stability (bottom axis – z/L, top axis – Ri_B) and the bulk-transfer coefficients relative to their neutral value (C_X/C_{XN} where X represents D, H or W) for several roughness values (computed from Eq. A32). The solid line indicates the momentum coefficient variation (C_D/C_{DN}) and the broken line indicates humidity and temperature coefficient (C_{HW}/C_{HWN}) variation.